THESIS

FAULT DAMAGE ZONES AND FRICTION: INSIGHTS FROM SHALLOW JAPAN TRENCH DRILL CORE

Submitted by

Tucker T. Keren

Department of Geosciences

In partial fulfillment of the requirements

For the Degree of Master of Science

Colorado State University

Fort Collins, Colorado

Summer 2015

Master's Committee:

Advisor: James D. Kirkpatrick

Jonathan S. Caine
Christopher A. Bareither

ABSTRACT

FAULT DAMAGE ZONES AND FRICTION: INSIGHTS FROM SHALLOW JAPAN TRENCH DRILL CORE

The integrated deformation in a fault damage zone provides a record of repeated slip on faults and the properties that control slip behavior. Shear displacement on faults is a frictional phenomenon in the sense that slip begins when the ratio of shear to normal stress surpasses the static friction coefficient (μ_s). Thus, earthquakes and the associated patterns of slip are controlled by the frictional properties of faults. The March 11, 2011 Mw 9.0 Tohoku-oki earthquake resulted in an unprecedented coseismic slip of >50 m in the shallow portion of the Japan Trench subduction zone. This thesis presents analysis of drill core recovered during Integrated Ocean Discovery Program (IODP) Expedition 343/343T (JFAST) that characterizes structures surrounding the inferred Japan Trench décollement, and uses the results to constrain the relative magnitude of the long-term, or static friction coefficient (μ_s) on the fault. Datasets include distinction of tectonic and induced structures in drill core, measurements of structure intensity at the core and microscopic scales, and core-scale structure orientations. The results show a sharp decrease in tectonic core-scale structure and microstructure intensity with distance from the décollement, with small spikes corresponding to locations of some known secondary faults. Orientation data reveals a nearly full range of structure dip angles <70° at all depths. The fall-off in structure intensity is fit by power law functions, with decay exponent (n) values consistently >1 in the footwall (underthrust sedimentary units) and <1 in the hanging wall (frontal prism sedimentary units). Estimations of the damage zone thickness from structure intensity data

results in an order of magnitude approximation of a few to several tens of meters. Faults of similar displacement report smaller damage decay exponents and larger damage zone thickness estimations. A quasi-static analytical model of a wavy, frictional fault is used to test the sensitivity of damage zone characteristics to the static friction coefficient (μ_s), and if friction may be responsible for distinct damage zone characteristics in the maximum coseismic slip region of the Japan Trench during the Tohoku-oki earthquake. Modeling suggests the comparatively narrow damage zone, steep damage decay exponents, and spread of structure orientations can all be a consequence of a frictionally weak fault with a low static friction coefficient ($\mu_s \approx 0.1$), consistent with existing constraints for the coseismic frictional strength of the Japan Trench décollement. Results and modeling suggest the shallow Japan Trench décollement is thus too weak to store significant elastic strain energy. Implications include constraints on models for the large shallow coseismic slip during the Tohoku-oki earthquake, and the potential for propagation of future large earthquakes through the shallow décollement without the presence of a shallow strong patch of the fault.

ACKNOWLEDGEMENTS

I would like to sincerely thank my advisor, Jamie Kirkpatrick, for the opportunity to contribute to the JFAST project and his guidance, support, and enthusiasm along the way. I am also thankful for the invaluable assistance of the curatorial staff at the Kochi Core Center and their hospitality. This thesis benefited from discussions with Jonathan Caine, Fred Chester, and the VCD team on board IODP Expedition 343. Thomas Luckie provided assistance in data collection. Cores, images, and data used in this study were provided by the Integrated Ocean Drilling Program (IODP). Funding for this study was provided by the National Science Foundation (award OCE 1260602).

TABLE OF CONTENTS

CHAPTER 1

Introduction

1.1 Overview

This thesis aims to develop an understanding of the role of fault friction on damage zone characteristics such as thickness, rate of damage decay, and structural orientations. A fault damage zone is defined as a zone of brittle deformation surrounding a fault in which the frequency of structures (e.g. fractures, veins, folds, stylolites, deformation bands, secondary faults, etc.) is higher than the background level in the host rock [e.g. *Chester and Logan*, 1986]. Damage zones are a significant architectural component of fault zones, in addition to the fault core and principal slip surface [*Caine et al.*, 1996]. Damage zone structures can form prior to, during, and after formation of the fault core, and therefore are both temporal and local in nature [*Fossen*, 2010]. Structures in damage zones also provide insight into the stresses acting on and around faults through their evolution, forming in predictable orientations with respect to the local stress field.

Frictional strength and stability control the way in which faults grow and evolve, including behavior of slip and earthquake rupture processes. Faulting initiates when the ratio of shear to normal stress surpasses the static friction coefficient (μ_s). Early laboratory studies suggested static friction is independent of lithology, and varies between $0.6 < \mu_s < 0.85$ [*Byerlee*, 1978]. However, clay minerals are an exception, having intrinsically lower friction than most rocks or minerals [*Scholz*, 2002]. After initiation of slip, friction changes as a function of the slip or slip velocity to a dynamic friction coefficient (μ_d). Reduction in frictional resistance during sliding is necessary to cause dynamic instability and sudden slip, generating earthquakes with an

associated stress drop. The process commonly occurs cyclically – stress builds up during a period of no fault motion, followed by another dynamic instability. This frictional behavior of faults is known as "stick slip" [*Brace and Byerlee*, 1966]. Furthermore, the frictional properties of faults control the stability of frictional sliding, depending on whether frictional resistance increases (velocity-strengthening, stable) or decreases (velocity-weakening, unstable) following given change in slip velocity [*Scholz*, 1998]. The "stick slip" model is the most simplified framework for earthquake mechanics, and thus has provided the basis for studies on the relationship between frictional properties of faults and earthquake behavior.

The 2011 Mw 9.0 Tohoku-oki earthquake resulted in coseismic slip of >50 m on the shallow Japan Trench décollement – the largest coseismic displacement ever recorded. Integrated Ocean Discovery Program (IODP) Expedition 343/343T (JFAST) sailed roughly one year after the earthquake (April – May 2012) with the goal of drilling through the plate-boundary décollement a few km landward of the trench within the region of large slip. Even with severe weather and other engineering difficulties [*Chester et al.*, 2013a], a core hole was drilled at site C0019 to 844.5 meters below the seafloor (mbsf) (hole C0019E; total depth = 7734 meters below sea level), achieving core recovery across the décollement. On board Expedition 343, core handling followed standard IODP procedures [*Chester et al.*, 2013a]: whole drill cores were scanned by a X-CT imaging device, whole round samples were collected, then cores were split in half and described by the scientific party geologists. Today, the archive halves of the core are housed at the Kochi Core Center IODP core repository in Kochi, Japan. Original high-resolution photos of core archive halves are available for download from the IODP data repository at: http://sio7.jamstec.go.jp/split-section-image/343/C0019E/. The primary scientific goal of the JFAST expedition was to gain insight on the physical mechanisms and dynamics of large

shallow slip earthquakes, which is inherently related to understanding the huge tsunami that followed [*Chester et al.,* 2013a].

Successful drilling and core recovery at site C0019 provided the chance to constrain the coseismic frictional properties (e.g. μ_d) of the décollement through laboratory experiments on core samples [*Ujiie et al.,* 2013; *Sawai et al.,* 2014; *Ikari et al.,* 2015], from data collected by a temperature observatory [*Fulton et al.,* 2013], and anisotropy of magnetic susceptibility measurements [*Yang et al.,* 2013]. The aforementioned studies all suggest the shallow Japan Trench décollement is frictionally weak, both coseismically and over geologic time. This thesis uses the independent structural observations in the drill cores encompassing the décollement damage zone to test for a signature of a frictionally weak fault. The hypothesis is as follows: the characteristics of the damage zone reflect long-term frictional weakness on the shallow décollement. In order to test this hypothesis, I adopted a three-pronged approach. First, I distinguish between tectonic and induced damage in the JFAST drill cores by defining a unique set of criteria that could be applied to any drill core containing similar rock types. Second, I measure damage zone characteristics such as rate of decay in deformation intensity away from décollement and damage zone thickness at the core and microscopic scales, as well as core-scale structural orientations. Third, I use a quasi-static analytical model of slip on a simplified wavy, frictional fault similar to the décollement to assess the sensitivity of measured damage zone characteristics with changes in static fault friction coefficient (μ_s). Modeling results show that not only can a very low friction coefficient explain the distinct damage zone characteristics at the JFAST site, but also damage zone structures could perhaps be used to independently constrain relative fault friction across faults in similar host lithologies and displacement.

The main contributions of this research are:

- Development of a criteria to distinguish tectonic from induced deformation in drill cores primarily composed of mudstone;
- Comprehensive characterization of damage zone structural properties (thickness, decay, orientations) in the JFAST drill cores;
- Assessment of sensitivity of JFAST damage zone characteristics with changes in static fault friction coefficient on a modeled wavy fault similar to the décollement;
- Independent constraint on relative magnitude of long-term fault friction on the shallow Japan Trench décollement;
- Basis for assessment of relative friction on faults in similar lithologies and of similar age solely from damage zone observations;
- Re-evaluation of the possible causes of extraordinary slip near the trench during the 2011 Tohoku-oki earthquake.

1.2 Motivation

Furthering our understanding of the mechanics of shallow slip in subduction zones and the long-term frictional strength of faults during tsunamigenic earthquakes can mitigate tsunami hazards worldwide, as tsunamis can be directly related to coseismic thrust displacement of the seafloor. Traditionally, shallow (< ~3 km, < ~150°) subduction plate-boundary faults composed of smectite- or illite-rich gouge were thought to be too weak to store much elastic strain energy, and therefore frictionally stable and unlikely to promote large slip [*Saffer and Marone*, 2003]. Clearly, the 2011 Tohoku-oki earthquake and associated shallow rupture has changed the way geologists think about the stability of shallow subduction zones. Large shallow coseismic slip

during the Tohoku-oki earthquake could have resulted from strain accumulation due to subducted seamounts [*Kennett et al.*, 2011; *Matsubara and Obara*, 2011; *Duan*, 2012], large transient stress changes on the fault [*Huang et al.*, 2012; *Kozdon and Dunham*, 2013], dramatic frictional weakening [e.g. *Shibazaki et al.*, 2011; *Noda and Lapusta*, 2013; *Ujiie et al.*, 2013], or dynamic overshoot [*Ide et al.*, 2011]. However, seismological constraints are not adequate for distinguishing between these mechanisms [e.g. *Scholz*, 2014]. Direct observation of tectonic deformation in the rocks is one approach. By observing off-fault deformation that has resulted from total displacement on the décollement, I have interpreted the relative magnitude of static friction on the décollement in the shallow Japan Trench. Using this information, I can better assess the models for the shallow coseismic slip during the Tohoku-oki earthquake, eliminating those that invoke processes inconsistent with inferred frictional strength. More generally, I can use the observed and modeled relationships between damage zone characteristics and fault friction to provide guidance in assessing the relative frictional strength of faults with similar host lithologies and displacements.

1.3 Thesis outline

This thesis addresses two main topics: 1) distinguishing tectonic and induced deformation and 2) evaluating the effect of fault friction on damage zone characteristics, both by way of observations in the JFAST drill core. The final section of this thesis briefly discusses the potential for future work building on the results of this project.

Chapter 2: Tectonic and induced structures in the JFAST core

Chapter 2 develops a set of criteria to distinguish tectonic and induced deformation in the JFAST core. After applying the methodology, the frequency of tectonic and induced structures is

examined with depth. Results show structure intensity has a maximum approximately adjacent to the décollement in the footwall and hanging wall. The pattern in structure intensity is apparent for both exclusively tectonic structures, and also tectonic and induced structures combined. Local increases in induced structure intensity mask trends in tectonic structures, demonstrating that detecting trends in spatial variability of structure intensity in drill core is dependent on the recognition of induced structures. Additionally, the tectonic structure intensity increases where core sections contain faults with significant displacements inferred from stratigraphic information, indicating that structure intensity can be used to identify locations of secondary faults. In order to promote application of similar methods during visual core description (VCD) on future IODP expeditions, Chapter 2 is in review at time of thesis submission to the *Proceedings of the IODP Expedition 343/343T* as a Data Report [*Keren and Kirkpatrick*, in review]. Submissions to the Proceedings volume are required to contain minimal interpretation of the data, so this is a short-format paper.

Chapter 3: The damage is done: low fault friction recorded in the damage zone of the shallow Japan Trench décollement

Chapter 3 investigates in detail the tectonic deformation in the Japan Trench décollement damage zone, and interprets the results in the context of fault friction. The results and interpretations in Chapter 3 are based on observations of tectonic deformation only, the types of which are outlined at the beginning of the results section (3.4.1), following the criteria outlined in Chapter 2. The primary datasets utilized in this chapter are measurements of structure intensity at the core (# of structures/m) and microscopic (# of microstructures/mm) scales, estimates of damage zone thickness based on the spatial decay in structure intensity away from the

décollement, and core-scale structure dip angles. Comparison of damage zone thickness and exponents describing the rate of decay in damage away from the décollement with faults of similar displacement reveals the shallow Japan Trench damage zone is distinct. I test the sensitivity of damage zone characteristics to changes in fault friction in order to evaluate the role of friction on the distinct properties observed in the JFAST core. The quasi-static analytical model of a wavy, frictional fault derived by *Chester and Chester* [2000] is used to test the hypothesis of a frictionally weak fault producing the distinct damage zone characteristics. Modeling suggests the damage zone thickness, structure orientations, and rate of damage decay are partially dependent on fault friction. The distinct damage zone characteristics in the JFAST core may therefore result from low static friction on the décollement over geologic time. A discussion of modeling limitations, and implications for scaling, dynamic rupture modeling, and décollement mechanics follows. Within the discussion, the results and interpretations from the JFAST core are extrapolated to consider the role of fault friction on the nature of structures in damage zones more generally. Finally, constraints on long-term friction are used to re-evaluate models for shallow coseismic slip during the Tohoku-oki earthquake. Chapter 3 was prepared with the intent for it to be submitted for publication in the *Journal of Geophysical Research.*

Chapter 4: Future work and remaining questions

Chapter 4 briefly overviews some of the scientific questions this work has brought forth, but does not answer. Key ideas include the possible extension of damage zone analysis in the shallow Japan Trench after future IODP drilling projects, integration of damage zone characteristics into fluid flow models to assess hydraulic properties, and testing of damage zone characteristics that reflect relative fault friction in similar lithologies.

REFERENCES

Brace, W. F., and J. D. Byerlee (1966), Stick-slip as a mechanism for earthquakes, *Science*, *153*(3739), 990-992.

Byerlee, J. D. (1978), Friction of rocks, *Pure and Applied Geophysics*, *116*, 615–629.

Caine, J. S., J. P. Evans, and C. B. Forster (1996), Fault zone architecture and permeability structure, *Geology*, *24*(11), 1025-1028, doi:10.1130/00917613(1996)024%3C1025:FZAAPS%3E2.3.CO;2.

Chester, F. M., and J. M. Logan (1986), Implications for mechanical properties of brittle faults from observations of the Punchbowl fault zone, California, *Pure and Applied Geophysics*, *124*(1-2), 79-106, doi:10.1007/bf00875720.

Chester, F. M., and J. S. Chester (2000), Stress and deformation along wavy frictional faults, *Journal of Geophysical Research*, *105*(B10), 23421-23430, doi:10.1029/2000jb900241.

Chester, F. M., J. Mori, N. Eguchi, S. Toczko, and the Expedition 343/343T Scientists (2013a), Proceedings of the Integrated Ocean Drilling Program; Japan Trench Fast Drilling Project (JFAST), *IODP Management International*, College Station, TX, doi:10.2204/iodp.proc.343343T.2013.

Duan, B. (2012), Dynamic rupture of the 2011 Mw 9.0 Tohoku-Oki earthquake: Roles of a possible subducting seamount, *Journal of Geophysical Research*, *117*, B05311, doi:10.1029/2011JB009124.

Fossen, H. (2010), *Structural Geology*, Cambridge University Press, Cambridge, UK, 463 pp.

Fulton, P. M., E. E. Brodsky, Y. Kano, J. Mori, F. Chester, T. Ishikawa, R. N. Harris, W. Lin, N. Eguchi, and S. Toczko (2013), Low coseismic friction on the Tohoku-Oki fault determined from temperature measurements, *Science*, *342*(6163), 1214-1217, doi:10.1126/science.1243641.

Huang, Y., L. Meng, and J. P. Ampuero (2012), A dynamic model of the frequency-dependent rupture process of the 2011 Tohoku-Oki earthquake, *Earth Planets Space*, *64*(12), 1061-1066, doi:10.5047/eps.2012.05.011.

Ide, S., A. Baltay, and G. C. Beroza (2011), Shallow dynamic overshoot and energetic deep rupture in the 2011 Mw 9.0 Tohoku-Oki earthquake, *Science*, *332*(6036), 1426-1429, doi:10.1126/science.1207020.

Ikari, M. J., J. Kameda, D. M. Saffer, and A. J. Kopf (2015), Strength characteristics of Japan Trench borehole samples in the high-slip region of the 2011 Tohoku-Oki earthquake, *Earth and Planetary Science Letters*, *412*, 35-41, doi:10.1016/j.epsl.2014.12.014.

Kennett, B. L. N., A. Gorbatov, and E. Kiser (2011), Structural controls on the Mw 9.0 2011 Offshore-Tohoku earthquake, *Earth and Planetary Science Letters, 310*(3), 462-467, doi:10.1016/j.epsl.2011.08.039.

Keren, T. T., and J. D. Kirkpatrick (2015), Tectonic and induced structures in the JFAST core, *Proceedings of the IODP 343/343T*, Integrated Ocean Drilling Program Management International, Inc., College Station, TX, in review.

Kozdon, J. E., and E. M. Dunham (2013), Rupture to the trench: Dynamic rupture simulations of the 11 March 2011 Tohoku earthquake, *Bulletin of the Seismological Society of America, 103*(2B), 1275-1289, doi:10.1785/0120120136.

Matsubara, M., and K. Obara (2011), The 2011 off the Pacific coast of Tohoku Earthquake related to a strong velocity gradient with the Pacific plate, *Earth Planets Space*, *63*(7), 663-667, doi:10.5047/eps.2011.05.018.

Noda, H., and N. Lapusta (2013), Stable creeping fault segments can become destructive as a result of dynamic weakening, *Nature, 493*(7433), 518-521, doi:10.1038/nature11703.

Saffer, D. M., and C. Marone (2003), Comparison of smectite-and illite-rich gouge frictional properties: application to the updip limit of the seismogenic zone along subduction megathrusts, *Earth and Planetary Science Letters, 215*(1-2), 219-235, doi:10.1016/s0012-821x(03)00424-2.

Scholz, C. H. (1998), Earthquakes and friction laws, *Nature, 391*(6662), 37-42.

Scholz, C. H. (2002), *The Mechanics of Earthquakes and Faulting* (2nd ed.), Cambridge University Press, Cambridge, UK, 471 pp.

Scholz, C. H. (2014), The Rupture Mode of the Shallow Large-Slip Surge of the Tohoku-Oki Earthquake, *Bulletin of the Seismological Society of America, 104*(5), 2627-2631.

Shibazaki, B., T. Matsuzawa, A. Tsutsumi, K. Ujiie, A. Hasegawa, and Y. Ito (2011), 3D modeling of the cycle of a great Tohoku-oki earthquake, considering frictional behavior at low to high slip velocities, *Geophysical Research Letters, 38*, L21305, doi:10.1029/2011GL049308.

Ujiie, K., H. Tanaka, T. Saito, A. Tsutsumi, J. J. Mori, J. Kameda, … S. Toczko (2013), Low coseismic shear stress on the Tohoku-Oki megathrust determined from laboratory experiments, *Science, 342*, 1211-1214, doi:10.1126/science.1243485.

Yang, T., T. Mishima, K. Ujiie, F. M. Chester, J. J. Mori, N. Eguchi, S. Toczko, and Exp. 343 Scientists (2013), Strain decoupling across the décollement in the region of large slip during the 2011 Tohoku-Oki earthquake from anisotropy of magnetic susceptibility, *Earth and Planetary Science Letters, 381*, 31-38, doi:10.1016/j.epsl.2013.08.045.

CHAPTER 2

Tectonic and induced structures in the JFAST core

Synopsis

A variety of structures in drill cores surrounding the inferred location of the Japan Trench plate-boundary décollement define a fault damage zone. We quantify the intensity of tectonic and induced structures in the damage zone from drill cores collected at site C0019 during Integrated Ocean Discovery Program (IODP) Expedition 343, the Japan Trench Fast Drilling Project (JFAST) between 770 and 835 meters below sea floor (mbsf). Cores contain structures formed by tectonic deformation and structures resulting from drill core recovery and handling. Differentiating between these two origins is essential for structural analyses and interpretation. We defined ten styles of induced structures that we used to develop a new set of criteria for identifying induced structures in drill cores containing fine-grained sedimentary rocks. These criteria were used to categorize structures according to confidence in a tectonic origin. Our results show structure intensity (including all fractures, faults, breccias, phyllosilicate bands) has a maximum adjacent to the décollement. This pattern in structure intensity is apparent for both exclusively tectonic structures, and also tectonic and induced structures combined. Local increases in induced structure intensity mask trends in tectonic structures, demonstrating that detecting trends in spatial variability in structure intensity is dependent on the recognition of induced structures. Additionally, the tectonic structure intensity increases where cores contain faults with significant displacements inferred from stratigraphic information indicating that tectonic structure intensity can be used to identify secondary faults. We suggest that the criteria for identifying induced structures used in this study could be applied during visual core

description (VCD) in a variety of tectonic settings as a method to collect and assess reliable structural data.

2.1 Introduction

Coseismic thrust displacement during the 2011 Tohoku-Oki M_w 9.0 earthquake reached ~40 – 80 m near the trench, the largest slip ever recorded for an earthquake [*Fujiwara et al.*, 2011; *Fujii et al.,* 2011; *Ide et al.*, 2011; *Lay et al.,* 2011; *Pollitz et al.*, 2011; *Yue and Lay*, 2011]. Integrated Ocean Drilling Program Expedition 343/343T (the 'JFAST' project) sailed one year after the earthquake to investigate the conditions and mechanisms that facilitated large, shallow slip. The primary goals of the JFAST project included identifying and sampling the rocks that were deformed during the earthquake to establish the processes active on the fault during slip, and to establish the stress state on the fault before, during, and after the earthquake [*Mori et al*., 2012]. Structural data is critical for locating the plate boundary décollement, where both the long-term and coseismic displacements are typically localized, and also where the attitude of fractures and faults around the fault provide information about the stress field when they formed [*Chester et al.,* 2013a].

Drilling was undertaken at site C0019, ~7 km landward of the trench in the region of maximum slip during the earthquake (Fig. 1) [*Chester et al.*, 2013a]. Cores were recovered at targeted intervals from hole C0019E, and onboard visual core description (VCD) followed standard IODP procedures [*Chester et al.*, 2013a]. Tectonic structures including mode I fractures, phyllosilicate bands, shear fractures, secondary faults, and breccia zones were logged and care was taken differentiate drilling induced deformation in the core from tectonic features.

Distinguishing tectonic structures from those induced by drilling and recovery processes is a key goal of VCD, but is difficult because tectonic and induced deformation may appear

alike, and drilling mud may also resemble natural features and sediments. Moreover, structures in weak sedimentary rock, like those recovered during the JFAST expedition, are not clearly mineralized, therefore increasing the difficulty of telling apart natural from induced damage. Of the published guidelines for identifying induced damage in core [e.g. *Pendexter and Rohn*, 1954; *Kidd*, 1978; *Kulander et al.*, 1979; *Dengo*, 1982; *Leggett*, 1982; *Kulander et al.*, 1990] few address induced damage in mudstone.

Results from Exp. 343/343T on-board VCD provided insufficient data for robust estimates of the spatial distribution or orientation of structures throughout the frontal prism and in particular surrounding the plate boundary fault [*Chester et al.*, 2013a; *Kirkpatrick et al.*, 2015]. Here, we re-examine the cores from hole C0019E with the aims of a) expanding on previous criteria for distinguishing induced and tectonic deformation, in order to b) evaluate the spatial variability of tectonic structure intensity, and c) establish whether structure intensity can be used to locate fault horizons as observed in IODP cores elsewhere [e.g. *Maltman et al.*, 1993; *Ujiie and Kimura*, 2014].

2.2 Cores from C0019E used in analysis

Twenty-one cores were recovered from coring hole C0019E from 176.5 to 185.2 meters below seafloor (mbsf), 648 – 660 mbsf, ~690 – 725 mbsf, and ~770 – 835 mbsf, with an overall recovery rate of 43%. The first 16 coring runs recovered rocks composed of Pliocene and Pleistocene siliceous mudstones of the hanging wall frontal prism [*Chester et al.*, 2013a; *Rabinowitz et al.*, 2015]. Core 17R-1 was composed of highly sheared scaly clay interpreted to be the plate-boundary décollement (821.5 to 822.5 mbsf) [*Chester et al.*, 2013a; *Rabinowitz et al.*, 2015]. Below the décollement, the rocks included Middle to Late Miocene brown siliceous

mudstone, Late Miocene stratified pelagic clay and Late Cretaceous laminar chert at the total drilling depth [*Chester et al.*, 2013a; *Rabinowitz et al.*, 2015]. Degree of lithification increases moderately with depth, indicated by increasing *P*-wave velocity (m/s) and electrical resistivity (Ωm) [*Chester et al.*, 2013a; *Nakamura et al.*, 2014]. Unconfined compressive strength of recovered rocks also increases with depth, ranging from 1 to 10 MPa [*Chester et al.*, 2013a]. All examined cores contain intact rock; the most poorly lithified units are pelagic clay, whereas the most well lithified units are chert.

The data reported here focuses on deformation that is hypothesized to define the damage zone surrounding the plate-boundary décollement, rather than all 21 cores collected at C0019E. A damage zone is generally defined as the network of subsidiary structures – faults, fractures, veins that bound a fault core and are related to its growth [e.g. *Chester and Logan*, 1986; *Caine et al.*, 1996]. This study focused on subsidiary structures in cores 10R to 20R, which surround the décollement and were recovered from 770 – 833.5 mbsf. We examined a total of 6.73 m of intact core below the décollement and a total of 9.38 m of intact core above the décollement. The total depth interval examined in this study is 63.5 m.

2.3 Methods

2.3.1 Distinguishing tectonic and induced deformation

Tectonic deformation in drill core includes the structures present in the volume of rock prior to drilling. Here, we use a set of criteria to identify tectonic deformation based on kinematic and geometric evidence following methods practiced onboard Expedition 343. Characteristics of tectonic structures in the split core face include:

- shear displacement evident by measurable offset of piercing points such as marker beds or other tectonic structures, truncation of marker beds or other tectonic structures

(displacement may exceed core width), development of slickenlines on fracture surface planes, significant changes in bedding orientation across a structure, or juxtaposition of different rock types/chemistries/fossil assemblages;

- development of fault rock formed by deformation within a brittle shear zone (e.g. scaly fabric defined by the surfaces of phacoid lenses that create an anastomosing network of curviplanar, striated shear surfaces), or as an alternative to scaly fabric, a non-foliated fault gouge;
- presence of tectonic breccia (which may occur without independent evidence for shear displacement), indicated by striated and/or polished surfaces on sub-angular to angular fragments, and gradational boundaries defined by less fractured rock;
- formation of anastomosing or braided networks of structures dark gray to black in color, often with higher X-ray computed tomography (X-CT) numbers (indicating increase in density) than the surrounding rock, and typically oblique to bedding (i.e. phyllosilicate bands [*Fossen et al.*, 2007]);
- fracture fill or mineralization, evident by change in color or mineralogy within structure compared to surrounding rock;
- consistent orientation(s) of adjacent structures that define structure sets likely forming under the same stress field.

Induced deformation in core includes the structures that form as a result of drilling, coring, or handling operations. *Kulander et al.* [1990] provide a detailed description of common induced structures observed in drill core, which fall into in three categories: drilling-induced structures that propagate in the rock ahead of the drill bit, coring-induced structures that develop anywhere within the core barrel, and handling-induced structures that form during or after

removal of the core from the core barrel. Drilling- and coring-induced structures are initiated by stresses related to drilling operations and/or removal of overburden pressure. Handling-induced structures are initiated by stresses related to splitting, bending, and impact after cores are brought onboard [*Kulander et al.*, 1990].

While the groupings defined by *Kulander et al.* [1990] provide a simple overview of induced structure types, complexity arises when core recovery results in open fractures forming along pre-existing *in situ* tectonic structures or sedimentary layering. Therefore, an open fracture in recovered core may be a primary tectonic structure, an induced feature, or an induced fracture superimposed on a primary structure and/or preexisting mechanical anisotropy. Examples of preexisting mechanical anisotropies can include natural fractures, faults, microfractures, bedding planes, residual stresses, and solution cleavage [*Kulander et al.*, 1990].

We defined ten styles of induced deformation from a combination of our observations of the split face of core C0019E and previously published descriptions of induced deformation. The definitions of each, and the criteria employed to identify them are described below.

Drilling Biscuits/Discs

Drilling biscuits or discs (termed ‘biscuits’ here) are one of the most commonly recognized examples of induced damage in core. Following observations made by *Pendexter and Rohn* [1954], *Kidd* [1978] first cataloged induced damage observations, with a focus on “core-discing” in the context of deep sea drilling after encountering examples in DSDP Leg 42A Mediterranean sediment cores. Biscuits appear as separated blocks with convex tops and/or concave bottoms (Fig. 2A), typically separated by drilling mud or a collection of rock fragments in a matrix of drilling mud. Drilling mud can also smear along the side of the core and out from

between biscuits, resulting in discrete, isolated biscuits of lithified material [*Leggett*, 1982]. Inclinations of biscuit edges are typically horizontal to sub-horizontal in vertical or sub-vertical cores; however, inclined bedding can influence the orientation [*Kulander et al.*, 1990]. Completely developed horizontal coring-induced biscuits cut entirely across the core or abut against earlier-formed natural or coring-induced structures [*Kulander et al.*, 1979]. Additionally, circular striations can sometimes be observed on tops and/or bottoms of biscuits.

Biscuiting is the result of vertical tensile stress acting on the rock during progress of the drill bit, followed by blocks spinning with respect to each other in the core barrel [*Kidd*, 1978; *Kulander et al.*, 1979]. The rapid removal of overlying strata permits underlying rocks to expand, contributing to vertical tension and the formation of sub-horizontal fractures due to unloading. It is then common for some biscuits to be held steady in the core barrel while other adjacent biscuits rotate with the drill. Curved edges form as the biscuits spin while staying in contact with each other [e.g. *Kidd*, 1978]. The wear and abrasion results in ‘erosion’ of biscuit edges and local formation of wear products that may resemble fault gouge or drilling mud.

Induced Brecciation

The term “induced breccia” is commonly used in VCD due to the tendency for drilling operations to recover cores that contain only fragmented angular clasts. See for example, cores 2R and 3R in core C0019E. However, throughout the majority of core C0019E, induced breccia clasts can appear within a single biscuit, as if each fragment is a uniquely fitting piece of a ‘puzzle’, or in between biscuits in random orientations. More simply, others have described drilling breccias as angular chips of indurated mudstone in drilling mud [*Leggett*, 1982]. One reliable way to differentiate between natural tectonic brecciation and drilling-induced brecciation

is the characteristics of striations on individual clasts. Induced breccias will sometimes lack slickenlines or polished surfaces due to limited relative motion between clasts. An exception is spiral or helicoidal slickenlines resulting from the biscuiting process [*Chester et al.,* 2013a; Methods chapter]. Most induced brecciation observed in core C0019E is not in a matrix of drilling mud, such as the induced breccia zone in Figure 2B, where none of the angular clasts exhibit slickenlines or polished surfaces between pieces.

Triangular Fracture Sets

Triangular fracture sets are common at the edge of the core barrel in the split face of the core. Triangular fracture sets are typically defined by sub-horizontal fractures dipping in opposite directions that intersect at the apex of a triangle, which points towards the center of the core. These structures are interpreted to be induced because their orientations locally parallel biscuit edges and/or other induced structure orientations, and the triangular geometry is consistent with localized failure during vertical flexing of the core [e.g. *Hiraishi*, 1984]. The triangles can occur at nearly all scales visible within the core. The angle at the apex between the two fractures in a triangular geometry ranges from ~30° (Fig. 2C) to over 100° (Fig. 2D). A complicating factor with determining the origin of fractures that make triangles at the edge of the drill core is the case of reactivation of tectonic fractures. In some cases, fractures with triangular geometries trend directly into tectonic structures, most commonly phyllosilicate bands (Fig. 2E). Triangular fracture sets can sometimes form in between two biscuits, and due to flexure of the core in the vertical direction, ultimately ‘erode’ away (Fig. 2C).

(Near) Right Angle Fractures

Continuous, open fractures exhibiting nearly 90° bends are prevalent near the outer edge of drill core C0019E. The most common occurrence of such fractures is along biscuit corners. Right angle fractures are observed both with no adjacent or parallel tectonic structures, and opening along pre-existing tectonic structures (Fig. 2F). In the absence of any evidence of shear or abutting relationships between the differently oriented segments of a right angle fracture, we infer that they are the result of continued rotation and flexure of the core, resulting in removal of corners from biscuits. As described in *Kulander et al.* [1990], induced fractures can form when pieces of intact core are chipped off along the edges due to the plucking action of the clockwise-rotating drill bit.

Radiating Fractures

Open fractures displaying a variety of orientations that radiate from, or seem to originate at, common points are observed in core C0019E and are inferred to be induced. This geometry is apparent in the split face and is consistent with formation in response to a load applied at an arbitrary angle and position where mismatched pieces of rock are in contact with intact core. Oftentimes the “impacting” fragment of rock is preserved, displaying a set of fractures that all radiate from the point of a triangular-shaped fragment (e.g. Fig. 2G). Similar radial arrays of fractures have been noted on previous IODP expeditions as being drilling-induced. *Arthur et al.* [1980] and *Dengo* [1982] describe the fractures as originating near the core center, with a radial symmetry in the down-core direction. *Kulander et al.* [1990] describe similar curviplanar fractures that originate outside of the core and diverge down-core. The point of origin for some radial fractures can therefore also be absent within the recovered core. However, an observation

of the preserved impacting fragment is also evidence of mobile piece(s) of rock during the coring process. Radial fractures that originate off-core are an indication of inception off-core and growth ahead of the advancing bit in rock that is subsequently drilled.

Core Axis Parallel Fractures

Several forms of induced deformation occur symmetrically about the long axis of the core. The most obvious of these is the presence of a zone of flowage [*Dengo*, 1982], or rock fragments in a matrix of dominantly drilling mud between the core and the core liner. Additionally, two types of vertical induced fractures are recognized that vary in scale and orientation. The first are petal-centerline fractures, described in detail by *Kulander et al*. [1979], *Kulander et al.* [1990], and *Li and Schmitt* [1998]. Characteristic petal-centerline fractures dip between 30 and 75 degrees in a down-core direction near the core edge and curve to dip vertically near the center of the core [*Kulander et al.*, 1990]. Petal-centerline fractures form in response to an induced principal tension that rotates downward in a vertical plane from an inclined orientation to horizontal [*Kulander et al.,* 1979], and the strike of the fracture surface is aligned with the direction of the greatest horizontal stress [*Li and Schmitt,* 1998]. We observe no clear petal-centerline fractures in the JFAST core, similar to other studies in thrust faulting regimes [*Li and Schmitt,* 1998]. However, in drill core of well-indurated rock, petal-centerline fractures are commonly used to estimate *in situ* principal stress orientations [e.g. *Li and Schmitt,* 1998; *Davatzes and Hickman*, 2010].

The second type of core axis-parallel induced fractures is typically smaller in scale, and interpreted to be related to both the coring and handling processes. Induced core axis-parallel fractures, sometimes several centimeters in length and open several millimeters, are best

observed in section 20R-2 of core C0019E (Fig. 2H). This section, composed of dominantly stratified pelagic clay with sub-horizontal bedding, displays sub-vertical fractures that appear to have originated near the center of the core and never reached the edge of the core. We interpret these induced fractures to form under non-uniform deformation of layers under triaxial or uniaxial stress conditions, similar to "axial cracking" described in *Dusseault and Van Domselaar* [1984] and *Kulander et al.* [1990], where compression of the core vertically results in the formation of vertical to sub-vertical mode I fractures that abut either a sub-horizontal biscuit boundary or detachment surface within the core.

Small Saw-Mark-Parallel Fractures

Open fractures that are roughly 1 cm or less in length on the core face and aligned parallel to the ridges and grooves produced by the core-splitting saw are common. The fractures have nearly perfectly horizontal rakes along the cut face (Fig. 2I) and do not extend to the edge of the core. Most importantly, small saw-mark-parallel fractures cannot be observed in X-CT imagery collected before core splitting. Small horizontal fractures commonly terminate against other open fractures. Especially where they terminate against reactivated induced structures, the terminating fractures are likely younger in age and not related to tectonic deformation. The orientation of the fractures parallel to the saw blade and relative timing of formation of the fractures shows that they are handling-induced.

Drilling Mud Injection

Drilling mud may be difficult to distinguish from lithified (or partially lithified) clay and mudstone in core. Drilling mud is typically lighter in color than the mudstones in core C0019E

and much softer. However, drilling mud can appear to be very similar to rocks lighter in color. In X-CT imagery, drilling mud is notably lighter colored than surrounding rocks due to the low density of the mud. Drilling mud correlates with induced deformation in a number of contexts. It can appear to have been injected through paths between drilling biscuits and is observed to penetrate along open fractures into the interior of the core. Small fragments of rock from core can be entrained within the drilling mud matrix giving the material the appearance of a breccia (Fig. 2J), however such fragments cannot be considered tectonic in origin with any confidence without the presence of slickenlines. In these occurrences, a combination of biscuiting and drilling mud injection results in a drilling breccia.

Fractures Crosscutting Drilling Mud

In rare instances, open fractures can be observed crosscutting drilling mud (Fig. 2K). The crosscutting and relative timing relationship is a clear indication that the fracture post-dates the injection of drilling mud, and therefore is induced by the drilling or coring processes.

Rubble

Commonly at the tops and bottoms of core sections, there is a total loss of coherence in the recovered rocks. The common location in the sections is not a coincidence, since cores are often sectioned in places where this style of induced deformation occurs. Resultantly, it is common for induced damage to be concentrated at the tops and bottoms of core sections, while remaining fairly evenly distributed throughout the rest of the core. Sub-rounded fragments with a variety of lithologies and randomly oriented bedding appear as “rubble” – or a zone of fragments that are not *in situ* and likely each have entirely different origins (Fig. 2L). Rubble zones display

no associated drilling mud when at the top of core sections. Fragments in rubble zones rarely retain a cut face parallel to the orientation of core splitting.

2.3.2 Measurement of structure intensity

For the purposes of quantifying the intensity of all structures in the examined cores, we categorized each structure based on a confidence index developed as part of this work. The first structural style (termed "Category 1") is deformation that is unequivocally tectonic and *in situ* – a 100% confidence level regarding tectonic origin (see criteria outlined in previous section). The second structural style (Category 2) is deformation that may be tectonic or induced in origin, but lacks definitive evidence for either source. The third structural style (Category 3) is deformation that can clearly be demonstrated to have been induced by drilling, coring, and/or handling operations.

The intensity of core-scale structures was quantified using a linear scanline sampling method performed on core imagery and verified through direct observation of the archive halves. Structure intensity is defined here as a linear measurement of number of structures per unit length (m^{-1}) [*Zeeb et al.*, 2013]. High-resolution imagery of all core sections was collected on board Expedition 343 using a MSCL-I digital imaging system with GEOSCAN IV: GEOTEK. The instrument uses a line-scan system for split-core imaging, reducing the optical distortion from the lens or variations of lighting, and provides 16bit RGB color tiff-formatted images with a resolution of 100 pixels/cm. The linear scanline method allows for quick measurement of structure characteristics and is the main method used in borehole image logs and cores [*Zeeb et al.,* 2013]. The linear scanline method has been used in many previous studies of damage zone structures at the outcrop scale and has clearly documented elevated damage in the vicinity of many major faults [e.g. *Caine and Forster*, 1999; Wilson *et al.*, 2003; *Mitchell and Faulkner*,

2009; *Savage and Brodsky*, 2011]. In order to best avoid induced damage near the edge of the core, the linear scanline was drawn down the center of each core section. The depth of every structure intersecting the scanline was recorded and each structure was assigned a category according to the classification scheme described above.

In intensively deformed intervals of cores (i.e. breccia zones), where the spacing between structures was ~1 cm or less, depths of structures within the zone were approximated by estimating the average size of clasts within the zone. As clasts within breccias are fragmented rock, the boundaries of clasts are fracture surfaces so the size of the clast is a measure of the fracture spacing. We used an image analysis method implemented in Matlab©, following the methods of *Bjørk et al.* [2009] to measure clast properties. Due to the irregular sizes and shapes of clasts in breccia zones, the simple linear scanline sampling method could not accurately represent the spacing of structures. We therefore calculated the average clast size in the breccia zone and set the structure intensity to the breccia interval thickness divided by the average clast diameter.

2.4 Results and Discussion

The linear scanline intersected 2,692 structures of all types over the total length of core examined (16.11 m). Of these, 1,085 were categorized as tectonic (Category 1), 1,225 were clearly induced (Category 3) and 382 could not be shown to be either tectonic or induced (Category 2). The complete data-table of structure depths for all categories is included in the supplementary material. Each core contained structures that fell into all three categories (for example, see Figure 3, which shows the categorization method applied to structures in section 14R-1 of core C0019E).

Combining all three categories of structures in core C0019E, the results show the greatest structure intensity (measured as the number of structures per 20 cm depth interval) occurs adjacent to the Japan Trench plate-boundary décollement (Fig. 4a). The largest structure intensity occurs near the décollement for all three of the structural categorizations (i.e. the same pattern is observed in calculations from exclusively Category 1 structures, summed Category 1 and 2, and summed Category 1, 2, and 3). In the hanging wall, local maxima for all three category combinations exceed 60 structures/m at ~819 mbsf. In the footwall, local maxima for all three category combinations surpass 80 structures/m at ~824 mbsf. These results show that high structure intensity correlates with the presence of the shallow Japan Trench décollement and an associated fault damage zone.

Throughout the interval of core spanned by our analysis, distinguishing trends in the spatial variability of structure intensity is dependent on the identification of induced structures. This is particularly the case in the hanging wall, where the structure intensity decreases with distance from the décollement for Category 1 structures, but not for the cumulative structure intensity of all three categories. For example, when induced deformation structures are included in the transect results above 790 mbsf, the combined total of Categories 1, 2 and 3 shows a slight increase in structure intensity. In contrast, the results for Category 1 structures without induced structures shows a significant decrease over the same interval. Including induced deformation structures therefore conceals the continued decay in tectonic structure intensity, and could result in misinterpretation if high structure densities are used to define tectonic faults. In the footwall, inclusion of induced deformation makes the decay in structure intensity with distance from the décollement appear less steep than the decay in Category 1 structure intensity.

Secondary faults have associated minor damage zones that can result in locally high structure intensity around a major structure [*Savage and Brodsky*, 2011]. Several major secondary faults defined by core observations [*Chester et al.*, 2013a; *Kirkpatrick et al*., 2015], radiolarian biostratigraphic age ranges [*Chester et al.*, 2013a], and/or chemostratigraphic constraints [*Rabinowitz et al.*, 2015] are located in the transect interval (Fig. 4a). Of the major secondary faults, there are two types: (1) those identified within sections of recovered core and (2) those inferred between core sections in intervals that were not recovered. We observe slightly elevated tectonic structure intensity at ~817 and ~832 mbsf, corresponding to the locations of a secondary fault defined from core observations and chemostratigraphic constraints [*Rabinowitz et al.*, 2015], respectively. At both depths, structure intensity decays both above and below the fault depth (see example from ~832 mbsf in Fig. 4b). Other secondary faults identified in recovered core sections (~824.5, ~825.2 mbsf) do not correlate with locally high tectonic structure intensity in our data. This is likely because the faults around 825 mbsf have small offsets, indicated by the lack of stratigraphic reversals or gaps associated with them [*Rabinowitz et al.*, 2015]. Secondary faults inferred between core sections are not resolvable from our structure intensity data due to large gaps in core recovery and incomplete recovery within coring intervals.

Similar structure intensity datasets from previous ocean drilling expeditions have been used to investigate deformation in core [e.g. *Maltman*, 1993; *Saito et al.*, 2001]. Our results show that the identification of induced structures and the confidence categorization method utilized in this study highlighted trends in tectonic deformation that would have been masked if induced deformation had been included. The induced structures described here are generic to drill core in sedimentary rocks, and the method we used could be applied in many tectonic settings,

potentially enhancing the application of structure intensity characterization for detailed structural analysis.

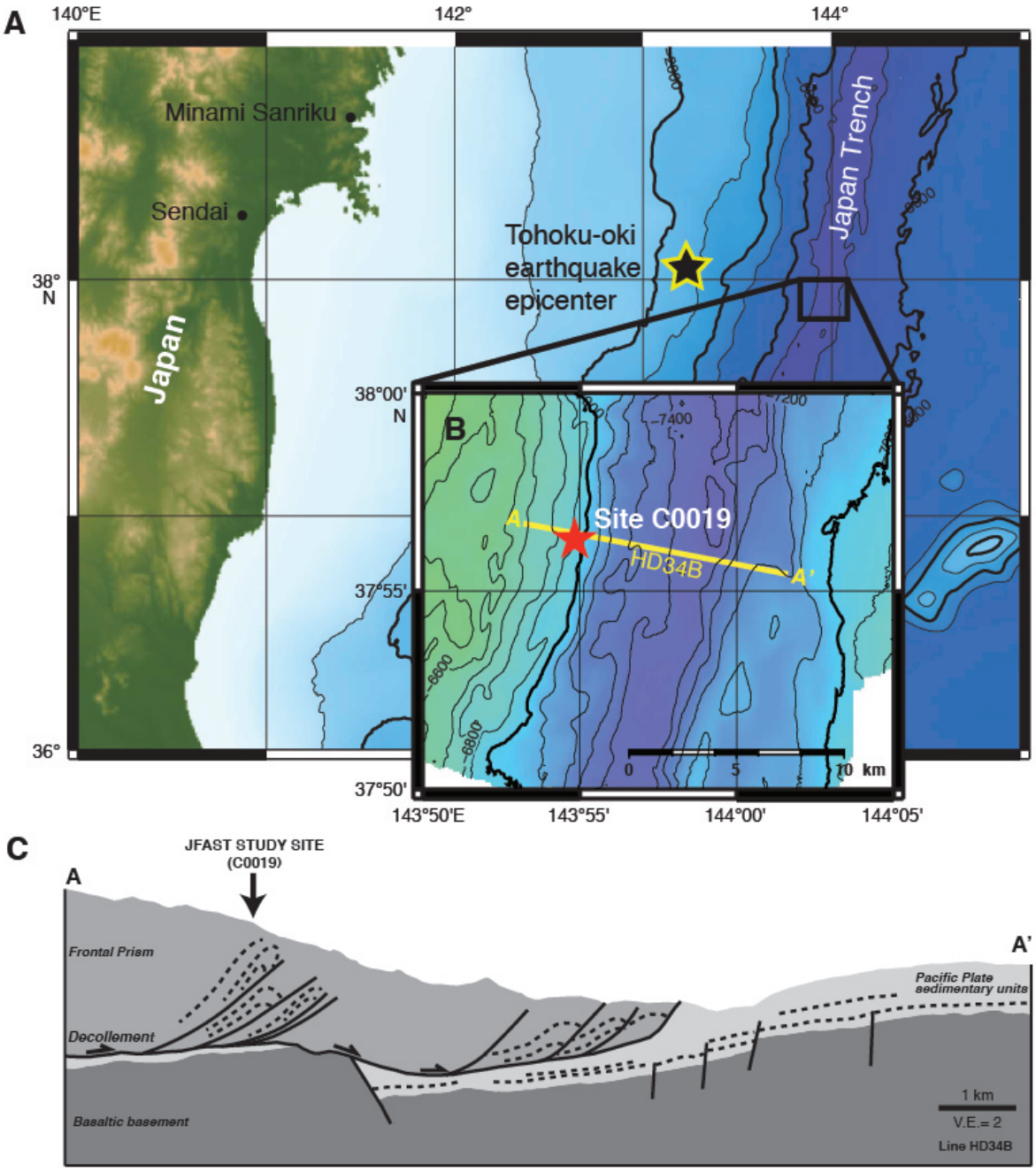

Figure 1. A) Location map, showing Tohoku area of the Japan Trench and Tohoku-oki earthquake epicenter (black star). B) Location of Expedition 343/343T Site C0019 (red star) and orientation of in-line seismic section Line HD34B [*Nakamura et al.*, 2013] (500 m N of C0019) [modified after *Chester et al.*, 2013a]. C) Cross-section (A to A') through the toe of the Japan Trench prism with location of Site C0019 and plate-boundary décollement showing overall margin architecture (vertical exaggeration = 2) [modified after *Kirkpatrick et al.*, 2015].

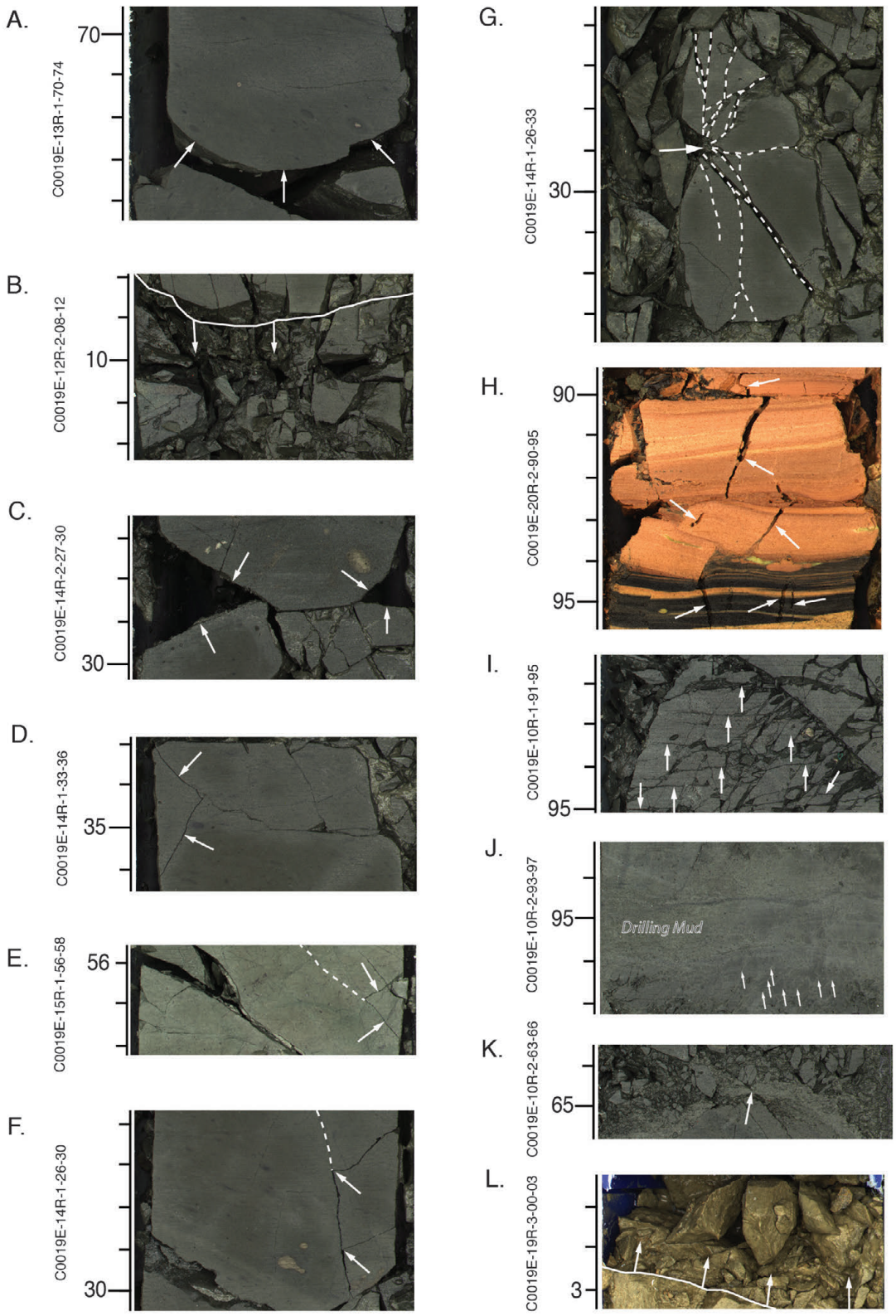

Figure 2. Examples of induced structure types observed in core C0019E, white arrows show feature exemplified in each image. A) Induced biscuit/disc fracture with characteristic arched

bottom. B) Induced brecciation below white line, with characteristic angular, randomly oriented clasts exhibiting no slickenlines. C) Two low-angle triangular fracture sets in which the internal piece of rock bound by the fractures no longer remains. D) High-angle triangular fracture set in which internal piece of rock remains. E) Triangular fracture set in which the fracture with an apparent dip to the right of the photo has opened along a pre-existing tectonic structure (denoted with dashed white line). F) Two approximately right angle fracture sets near bottom edge of an induced biscuit/disc. The fracture with an apparent steep dip to the right of the photo has opened along a pre-existing tectonic structure (denoted with dashed white line). G) Radial fracture set (white dashed lines) propagating from an impact point likely at the location of the white arrow. H) Sub-vertical fractures in the pelagic clay at the base of core section 20R-2. I) Small saw-mark-parallel fractures that open in the same orientation as the horizontal saw-mark striations in the upper right portion of the photo. J) Induced fractures resulting from drilling mud injection. Drilling mud has a characteristic bright color, which matches the color of the fill in the fractures identified with white arrows. K) Open fracture crosscutting a zone of drilling mud injection. L) Zone of rubble, characteristically at the top of a core section with randomly oriented, mismatched fragments with no slickenlines. All scales are in cm.

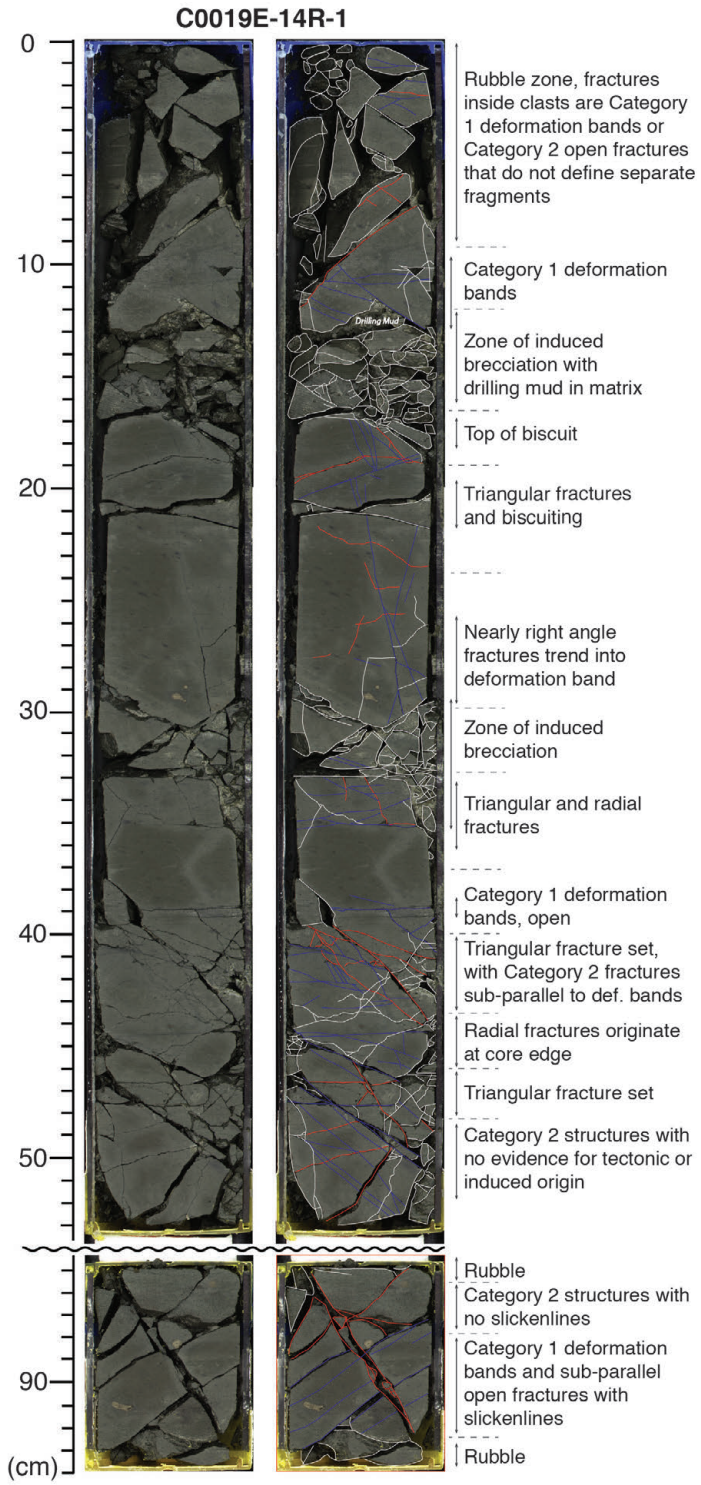

Figure 3. A) High-resolution MCSL-I photograph of core section 14R-1 archive half, cropped at wavy black line to exclude sampled portion of core between 53 and 85 cm (where imagery is unavailable). B) Same core section digitized with structure traces and types based on confidence categorization method (blue lines are Category 1 structures, red lines Category 2, and white lines Category 3).

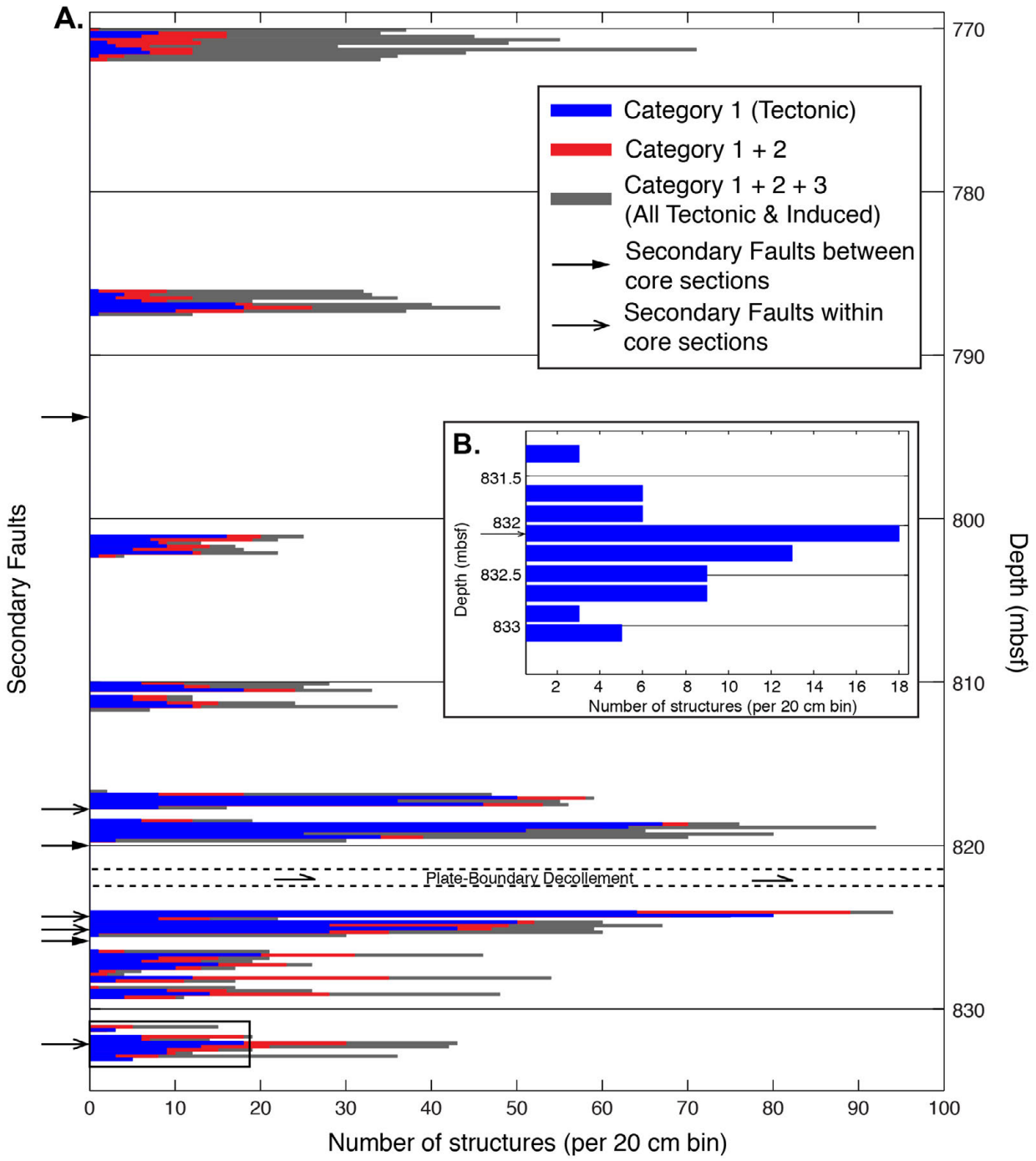

Figure 4. A) Number of structures (per 20 cm bin) vs. depth below sea floor. Depths of known secondary faults noted, most of which are not resolvable from tectonic structure intensity data. B) Zoom-in of the location of the secondary fault identified from chemostratigraphy showing the corresponding structure intensity data. A small increase in tectonic structure intensity is centered on the secondary fault.

REFERENCES

Arthur, M. A., B. Carson, and R. von Huene (1980), Initial tectonic deformation of hemipelagic sediment at the leading edge of the Japan convergent margin, in: Langseth, M., H. Okada, *et al.* (eds.), *Initial Reports of the Deep Sea Drilling Project 56-57 Part 1*, College Station, TX, 569-614, doi:10.2973/dsdp.proc.5657.115.1980.

Bjørk, T. E., K. K. Mair, and H. H. Austrheim (2009), Quantifying granular material and deformation: advantages of combining grain size, shape, and mineral phase recognition analysis, *Journal of Structural Geology*, *31*(7), 637-653, doi:10.1016/j.jsg.2009.03.020.

Caine, J. S., and C. B. Forster (1999), Fault zone architecture and fluid flow: Insights from field data and numerical modeling, in: Haneberg, W. C., P. S. Mozley, J. C. Moore and L. B. Goodwin (eds.), *Faults and Subsurface Fluid Flow in the Shallow Crust*, American Geophysical Union, Washington, D. C.

Caine, J. S., J. P. Evans, and C. B. Forster (1996), Fault zone architecture and permeability structure, *Geology*, *24*(11), 1025-1028, doi:10.1130/00917613(1996)024%3C1025:FZAAPS%3E2.3.CO;2.

Chester, F. M., and J. M. Logan (1986), Implications for mechanical properties of brittle faults from observations of the Punchbowl fault zone, California, *Pure and Applied Geophysics*, *124*(1-2), 79-106, doi:10.1007/bf00875720.

Chester, F. M., J. Mori, N. Eguchi, S. Toczko, and the Expedition 343/343T Scientists (2013a), Proceedings of the Integrated Ocean Drilling Program; Japan Trench Fast Drilling Project (JFAST), *IODP Management International*, College Station, TX, doi:10.2204/iodp.proc.343343T.2013.

Davatzes, N. C., and S. H. Hickman (2010), Stress, Fracture, and Fluid-flow Analysis Using Acoustic and Electrical Image Logs in Hot Fractured Granites of the Coso Geothermal Field, California, U.S.A., in: Pöppelreiter, M., C. Garcia-Carballido, and M. Kraaijveld (eds.), *Dipmeter and Borehole Image Log Technology*, American Association of Petroleum Geologists Special Volumes, Tulsa, OK, 259–293.

Dengo, C. (1982), A structural analysis of cores from the Leg 67 transect across the Middle America Trench offshore Guatemala, in: Aubuoin, J., R. von Huene, *et al.*, (eds.), *Initial Reports of the Deep Sea Drilling Project 67*, College Station, TX, 651-666, doi:10.2973/dsdp.proc.67.133.1982.

Dusseault, M. B., and H. R. Van Domselaar (1984), Unconsolidated sand sampling in Canadian and Venezuelan oil sands: Proceedings of UNITRAR Second International Oil Conference on the Future of Heavy Crudes and Tar Sands, Caracas, Venezuela, 336-348.

Fossen, H., R. A. Schultz, Z. K. Shipton, and K. Mair (2007), Deformation bands in sandstone: a review, *Journal of the Geological Society, London*, *164*(4), 755-769, doi:10.1144/0016-76492006-036.

Fujii, Y., K. Satake, S. I. Sakai, M. Shinohara, and T. Kanazawa (2011), Tsunami source of the 2011 off the Pacific coast of Tohoku Earthquake, *Earth Planets Space*, *63*(7), 815-820, doi:10.5047/eps.2011.06.010.

Fujiwara, T., S. Kodaira, T. No, Y. Kaiho, N. Takahashi, and Y. Kaneda (2011), The 2011 Tohoku-Oki earthquake: Displacement reaching the trench axis, *Science*, *334*(6060), 1240-1240, doi:10.1126/science.1211554.

Fulton, P. M., E. E. Brodsky, Y. Kano, J. Mori, F. Chester, T. Ishikawa, ... and S. Toczko (2013), Low coseismic friction on the Tohoku-Oki fault determined from temperature measurements, *Science*, *342*(6163), 1214-1217, doi:10.1126/science.1243641.

Hiraishi, H. 1984, Evaluation of shear and flexural deformations of flexural type shear walls, *Bulletin of the New Zealand Society for Earthquake Engineering*, *17* (2), 135–144.

Ide, S., A. Baltay, and G. C. Beroza (2011), Shallow dynamic overshoot and energetic deep rupture in the 2011 Mw 9.0 Tohoku-Oki earthquake, *Science*, *332*(6036), 1426-1429, doi:10.1126/science.1207020.

Kidd, R. B. (1978), Core discing and other drilling effects in DSDP Leg 42A Mediterranean sediment cores, in: Hsü, K., L. Montadert, *et al.* (eds.), *Initial Reports of the Deep Sea Drilling Project 42 Part 1*, College Station, TX, 1143-1149, doi:10.2973/dsdp.proc.42-1.app1.1978.

Kirkpatrick, J. D., C. D. Rowe, K. Ujiie, J. C. Moore, C. A. Regalla, F. Remitti, V. Toy, M. Wolfson-Schwehr, J. Kameda, S. Bose, and F. M. Chester (2015), Structure and lithology of the Japan Trench subduction plate boundary fault, *Tectonics*, *34*, 53–69, doi:10.1002/2014TC003695.

Kulander, B. R., C. C. Barton, and S. L. Dean (1979), *Application of fractography to core and outcrop fracture investigations* (No. METC/SP-79/3), Department of Energy, Morgantown, WV (USA), Morgantown Energy Research Center.

Kulander, B. R., S. L. Dean, and B. J. Ward (1990), Fractured core analysis: Interpretation, logging, and use of natural and induced fractures in core, *AAPG Methods in Exploration Series*, *8*, American Association of Petroleum Geologists, Tulsa, OK.

Lay, T., C. J. Ammon, H. Kanamori, L. Xue, and M. J. Kim (2011), Possible large near-trench slip during the 2011 M_w 9.0 off the Pacific coast of Tohoku Earthquake, *Earth Planets Space*, *63*(7), 687-692, doi:10.5047/eps.2011.05.033.

Leggett, J. K. (1982), Drilling-induced structures in Leg 66 cores, in*:* Mariana, L., *et al.* (eds.) *Initial Reports of the Deep Sea Drilling Project 66*, College Station, TX, 531-538, doi:10.2973/dsdp.proc.66.118.1982.

Li, Y., and D. R. Schmitt (1998), Drilling-induced core fractures and in situ stress, *Journal of Geophysical Research, 103*(B3), 5225–5239, doi:10.1029/97JB02333.

Lundberg, N. C. and J. C. Moore (1986), Macroscopic structural features in Deep Sea Drilling Project cores from forearc regions, in: Moore, J.C. (ed.) *Structural Fabrics in Deep Sea Drilling Project Cores from Forearcs*, Memoirs of the Geological Society of America, *166*, 13–44, doi:10.1130/mem166-p13.

Maltman, A. J., T. Byrne, D. E. Karig, and S. Lallemant (1993), Deformation at the toe of an active accretionary prism: synopsis of results from ODP Leg 131, Nankai, SW Japan, *Journal of Structural Geology*, *15*(8), 949-964, doi:10.1016/0191-8141(93)90169-b.

Mitchell, T. M., and D. R. Faulkner (2009), The nature and origin of off-fault damage surrounding strike-slip fault zones with a wide range of displacements: a field study from the Atacama fault system, northern Chile, *Journal of Structural Geology*, *31*(8), 802-816, doi:10.1016/j.jsg.2009.05.002.

Mori, J., F. M. Chester, N. Eguchi, and S. Toczko (2012), Japan Trench Fast Earthquake Drilling Project (JFAST), *IODP Scientific Prospectus*, *343*(10.2204), doi:10.2204/iodp.sp.343.2012.

Nakamura, Y., S. Kodaira, B. J. Cook, T. Jeppson, T. Kasaya, Y. Yamamoto, Y. Hashimoto, M. Yamaguchi, K. Obana, and G. Fujie (2014), Seismic imaging and velocity structure around the JFAST drill site in the Japan Trench: low *V*p, high *V*p/*V*s in the transparent frontal prism, *Earth, Planets and Space*, *66*(1), 121, doi:10.1186/1880-5981-66-121.

Nakamura, Y., S. Kodaira, S. Miura, C. Regalla, and N. Takahashi (2013), High-resolution seismic imaging in the Japan Trench axis area off Miyagi, northeastern Japan, *Geophysical Research Letters*, *40*(9), 1713-1718, doi:10.1002/grl.50364.

Pendexter, C., and R. E. Rohn (1954), Fractures induced during drilling, *Journal of Petroleum Technology*, *6*(3), 15.

Pollitz, F. F., R. Bürgmann, and P. Banerjee (2011), Geodetic slip model of the 2011 M9.0 Tohoku earthquake, *Geophysical Research Letters*, *38*, L00G08, doi:10.1029/2011gl048632.

Rabinowitz, H. S., H. M. Savage, T. Plank, P. J. Polissar, J. D. Kirkpatrick, C. D. Rowe (2015), Multiple major faults at the Japan Trench: Chemostratigraphy of the plate boundary at IODP Exp. 343: JFAST, *Earth and Planetary Science Letters,* in review.

Saito, S., D. Goldberg, and Leg 196 Shipboard Scientific Party (2001), ODP Leg 196: Deformation and Fluid Flow Processes in the Nankai Trough Accretionary Prism, Downhole Logging Summary, retrieved December 9, 2014, from http://brg.ldeo.columbia.edu/data/odp/odp-log_sum/leg196/196.index.html

Savage, H. M. and E. E. Brodsky (2011), Collateral damage: Evolution with displacement of fracture distribution and secondary fault strands in fault damage zones, *Journal of Geophysical Research, 116*, B03405, doi:10.1029/2010jb007665.

Ujiie, K., and G. Kimura (2014), Earthquake faulting in subduction zones: insights from fault rocks in accretionary prisms, *Progress in Earth and Planetary Science, 1*(7), doi:10.1186/2197-4284-1-7.

Yue, H., and T. Lay (2011), Inversion of high-rate (1 sps) GPS data for rupture process of the 11 March 2011 Tohoku earthquake (Mw 9.1), *Geophysical Research Letters, 38*, L00G09, doi:10.1029/2011gl048700.

Wilson, J. E., J. S. Chester, and F. M. Chester (2003), Microfracture analysis of fault growth and wear processes, Punchbowl Fault, San Andreas system, California, *Journal of Structural Geology, 25*(11), 1855-1873, doi:10.1016/s0191-8141(03)00036-1.

Zeeb, C., E. Gomez-Rivas, P. D. Bons, and P. Blum (2013), Evaluation of sampling methods for fracture network characterization using outcrops, *AAPG Bulletin, 97*(9), 1545-1566, doi:10.1306/02131312042.

CHAPTER 3

The damage is done: low fault friction recorded in the damage zone of the shallow Japan Trench décollement

Synopsis

The integrated deformation in a fault damage zone provides a record of repeated slip on faults and the conditions that control slip behavior, including friction. To assess the role of fault friction on damage zone structural patterns, we utilized Integrated Ocean Drilling Program (IODP) Expedition 343 (JFAST) drill core recovered from the shallow Japan Trench. Core- and micro-scale structure densities decrease sharply above and below the décollement in a manner fit by power law functions. Core-scale structure decay exponents (n) are 1.45 in the footwall and 0.70 in the hanging wall. Microstructure decay exponents (n) are 1.09 in the footwall and 0.50 in the hanging wall. Damage zone thickness is on the order of a few tens of meters. At all depths, core-scale structures dip between ~10° and ~70° and are mutually crosscutting. Compared to similar offset faults, the décollement has steep decay exponents and a comparatively narrow damage zone. Motivated by previous constraints that demonstrate the plate boundary is weak, we tested if the damage zone characteristics are consistent with low fault friction. Quasi-static modeling of off-fault stresses and deformation due to slip on a wavy, frictional fault similar to the décollement predicts frictionally weak faults exhibit narrow damage zones, steep damage decay exponents, and no preferred orientations of damage zone structures. We interpret the integrated damage zone properties in the shallow Japan Trench to reflect long-term frictional weakness of the décollement, suggesting great earthquake propagation to the trench does not require a shallow strong patch of the fault.

3.1 Introduction

Damage zones record the mechanical conditions causing slip along faults. While principal slip zones and the fault core accommodate displacement, the broader volume surrounding a fault accumulates strain through time in the form of structures of various kinds. A sharp decay in intensity of damage zone structures away from faults has been recognized in outcrop [e.g. *Brock and Engelder*, 1977; *Chester and Logan*, 1986; *Anders and Wiltschko*, 1994; *Vermilye and Scholz*, 1998; *Shipton et al.*, 2005; *Mitchell and Faulkner*, 2009], drill core [e.g. *Maltman et al.*, 1993; *Fossen and Hesthammer*, 2000; *Heermance et al.*, 2003], and geophysical logs [e.g. *Johri et al.*, 2014b]. The functional form of damage decay is similar to models for decaying stresses with distance from a fault [*Cowie and Scholz*, 1992; *Scholz et al.*, 1993; *Savage and Brodsky*, 2011]. The rate of damage decay and damage zone thickness vary significantly for different faults, as demonstrated by scaling relations that relate damage zone characteristics to displacement, length, or thickness [e.g. *Hull*, 1988; *Evans*, 1990; *Knott et al.*, 1996; *Lyakhovsky*, 2001; *Shipton et al.*, 2006; *Childs et al.*, 2009; *Faulkner et al.*, 2011a; *Savage and Brodsky*, 2011].

Processes that cause structures to form within damage zones include fault propagation and growth [e.g. *Cowie and Scholz*, 1992; *McGrath and Davison*, 1995; *Vermilye and Scholz*, 1998], wear related to fault geometry [e.g. *Scholz*, 1987; *Wilson et al.*, 2003], and off-fault plasticity accompanying earthquake rupture [e.g. *Rice et al.*, 2005]. Fractures in the damage zone are a function of the stress field at formation suggesting fracture orientations should be useful for constraining off-fault stresses [e.g. *Kilsdonk and Fletcher*, 1989; *Saucier et al.*, 1992; *Chester and Fletcher*, 1997; *Chester and Chester*, 2000; *Griffith et al.*, 2010]. While the types, distributions, and orientations of damage zone structures corresponding to each fault evolution

process may be predictable for some faults [e.g. *Wilson et al.*, 2003; *Mitchell and Faulkner*, 2009], similar recognition of structures can be very complicated for mature faults that have experienced multiple slip events. Nevertheless, the integrated damage zone deformation can elucidate properties of faults over geologic time, such as the long-term fault friction.

Fault friction is a primary control on the stress field around a fault, so damage zones should also be dependent on friction. However, few studies have approached the effects of friction on damage zone characteristics, specifically the rate of damage decay from a fault, perhaps because fault friction is not readily measured in the field. The role of fault friction has primarily been addressed in quasi-static and dynamic modeling of off-fault stress and deformation [e.g. *Johnson and Fletcher*, 1994; *Cooke*, 1997; *Cooke and Pollard*, 1997; *Lyakhovsky et al.*, 1997; *Chester and Chester*, 2000; *Faulkner et al.*, 2006; *Griffith et al.*, 2010; *Savage and Cooke*, 2010]. These results suggest an increase in static fault friction increases the size of a brittle failure region, a proxy for damage zone thickness [*Chester and Chester*, 2000]. Additionally, an increase in static friction is predicted to decrease the variations in principal stress orientations near a fault [*Chester and Chester*, 2000; *Griffith et al.*, 2010].

Drill core recovered from Integrated Ocean Drilling Program (IODP) Expedition 343/343T, or the Japan Trench Fast Drilling Project (JFAST; *Chester et al.*, 2013a), provided the opportunity to examine the damage zone of a plate-boundary décollement where the fault is already demonstrated to be frictionally weak [*Fulton et al.*, 2013; *Ujiie et al.*, 2013]. The March 11, 2011 Tohoku-oki M_w9.0 earthquake ruptured through the shallow portion of the subduction fault, with coseismic thrust displacement exceeding ~50 m near the trench (Fig. 5a) [e.g. *Fujii et al.*, 2011; *Ide et al.*, 2011; *Ito et al.*, 2011; *Pollitz et al.*, 2011; *Yue and Lay*, 2011; *Kodaira et al.*, 2012], directly contributing to the devastating tsunami that followed. Large magnitudes of slip

updip of the seismogenic zone were conventionally considered unfavorable in subduction settings, due to the tendency of shallow fault zone material to strengthen with increasing slip rate [*Saffer and Marone*, 2003]. Following the earthquake, the JFAST expedition recovered drill core samples transecting the shallow plate-boundary décollement. As frictional strength and stability are crucial factors in determining seismic and tsunami hazards, many studies have aimed to determine the coseismic frictional properties of the shallow décollement [e.g. *Fulton et al.*, 2013; *Ujiie et al.*, 2013; *Sawai et al.*, 2014]. Here, we take an alternative approach and use the integrated damage zone characteristics in the JFAST core to assess the role of long-term (static) friction on the décollement.

3.2 Tectonic setting

The Japan Trench is a convergent margin where the Pacific Plate subducts beneath the North American Plate in the direction N62°W at a rate of ~85 mm/y [*Apel et al.*, 2006; *DeMets et al.*, 2010; *Argus et al.*, 2011]. The margin has historically hosted high rates of seismic activity, notably eighteen M_w7 or larger earthquakes in the past 400 years [e.g. *Kanamori et al.*, 2006; *Hashimoto et al.*, 2009], not including the 2011 M_w 9.0 Tohoku-oki event and its aftershocks. Records of tsunamis suggest great earthquakes, and perhaps shallow coseismic slip, recurred in the Japan Trench between ~500 [*Sawai et al.*, 2012] and ~1100 [*Minoura et al.*, 2001] years.

Drilling expeditions [*Scientific Party*, 1980; *Chester et al.*, 2013a] and seismic reflection surveys [*von Huene et al.*, 1982, 1994; *Suyehiro and Nishizawa*, 1994; *Tsuru et al.*, 2000, 2002; *Kodaira et al.*, 2012; *Nakamura et al.*, 2013] show that the Japan Trench consists of a deep-sea terrace, middle prism, frontal prism, trench, outer trench slope, and plate-boundary décollement. Beneath the deep-sea terrace, 15-30 km landward of the trench, upwards of ~5 km of Neogene

sedimentary units overly a regional Cretaceous unconformity [e.g. *Scientific Party*, 1980; *von Huene et al.,* 1982; *von Huene and Culotta*, 1989; *von Huene and Lallemand*, 1990]. The missing Paleogene and early Neogene sediments reflect sub-aerial erosion in response to upper plate thinning and deep-sea terrace subsidence that are thought to be the consequence of hydrofracturing above the décollement [*von Huene et al.,* 2004]. The middle prism contains seismically resolved ~N-S striking normal faults with displacements as large as ~800 m [*Tsuji et al.*, 2011]. The frontal prism displays disrupted and chaotic reflectors [e.g. *Tsuru et al.*, 2000; *Chester et al.*, 2013a] in the form of poorly resolved landward- and shallowly-dipping thrust faults that branch off the décollement and displace uniform hemi-pelagic sediments [*Scientific Party*, 1980; *Tsuji et al.*, 2011; *Nakamura et al.*, 2013]. The Pacific Plate outer trench slope is composed of normal faults that cut a sequence of hemi-pelagic mudstone, pelagic clay, chert, and basement basaltic rocks with increasing depth. A horst-and-graben topography is initiated ~100 km seaward of the trench axis [e.g. *Tsuru et al.,* 2002; *Miura et al.,* 2005]. The plate-boundary décollement is resolved between the frontal prism and down-going Pacific Plate at shallow depths.

The JFAST study site (IODP site C0019) is ~7 km landward of the Japan Trench and ~100 km ESE of the 2011 Tohoku-oki earthquake epicenter (Fig. 5a,b). Seismic surveys have interpreted a shallowly dipping (~8°) reflector as the décollement, around 821.5 meters below sea floor (mbsf) at the site [*Nakamura et al.,* 2013]. An area-balanced reconstruction of a plate-convergence-parallel seismic section through the site estimates the total west-directed subduction of the Pacific Plate (footwall) relative to the hanging wall is at least ~3.2 km [*Chester et al.*, 2013b]. IODP Expedition 343/343T recovered 21 cores from targeted intervals at 176.5 to 185.2, 648 to 660, ~690 to 725, and ~770 to 835 mbsf hole C0019E at site C0019, with an overall

recovery rate of 43% (Fig. 5c) [*Chester et al.*, 2013a]. The upper 16 cores from the frontal prism are composed of Pliocene and Pleistocene siliceous mudstones with varying amounts of siliciclastic, volcanic, and biogenic material [*Rabinowitz et al.*, 2015]. Core 17R-1 was recovered from the depth of the décollement seismic reflector and is composed of strongly deformed scaly clay interpreted to be the plate-boundary fault (821.5 to 822.5 mbsf) [*Chester et al.*, 2013a, 2013b]. The maximum thickness of the décollement is 4.87 m, accounting for unrecovered intervals above and below core 17R-1 [*Chester et al.*, 2013b]. Below the décollement, the recovered cores are composed of Middle to Late Miocene siliceous mudstone, Late Miocene stratified pelagic clay, and Late Cretaceous laminar chert at the total drilling depth [*Chester et al.*, 2013a; *Rabinowitz et al.*, 2015]. Degree of lithification increases moderately with depth, indicated by increasing *P*-wave velocity (m/s) and electrical resistivity (Ωm) [*Chester et al.*, 2013a; *Nakamura et al*., 2014]. Unconfined compressive strength of recovered rocks also increases with depth, ranging from 1 to 10 MPa [*Chester et al.*, 2013a]. All examined cores contain intact rock; the most poorly lithified units are pelagic clay, whereas the most well lithified units are chert.

Various lines of evidence suggest the décollement is frictionally weak. Fault zone textures within the ~1 m of recovered core from the décollement suggest shear slip on the fault occurred within a thin layer of smectite-rich (60-80 wt%) scaly clay [*Chester et al.*, 2013b; *Kameda et al.*, 2015; *Kirkpatrick et al.*, 2015]. Friction experiments performed on samples of the fault reveal the material is weak and changes between velocity-strengthening behavior at sub-seismic slip rates to velocity-weakening at coseismic rates [*Ujiie et al.*, 2013; *Ikari et al.*, 2015]. In agreement with friction experiments, *in situ* temperature measurements following the Tohoku event indicate a very low coseismic shear resistance [*Fulton et al.*, 2013]. Orientations of

anisotropy of magnetic susceptibility in core samples are different above and below the décollement suggesting the décollement is decoupled over geologic time [*Yang et al.*, 2013]. Samples of the frontal prism are also relatively weak, but still much stronger than the décollement due to lower clay content and diagenetic silica cementation [*Ikari et al.*, 2015]. Prior to the Tohoku-oki earthquake, *Wang and Suyehiro* [1999] reported a low coefficient of friction on the décollement to explain upper crust compressional stress in NE Japan.

Significant secondary faults have been identified or inferred at the JFAST site from drill core observations, radiolarian biostratigraphic ages, and/or chemostratigraphic constraints (Fig. 5c), in addition to the seismic observations. In recovered core, secondary faults were identified at ~700, 720, 817.5, and two around 825 mbsf [*Chester et al.*, 2013a; *Kirkpatrick et al.*, 2015]. Using constraints on age reversals and gaps, secondary faults have also been inferred at ~790, 820, 824, 826, 832, and 833 mbsf [*Chester et al.*, 2013a; *Rabinowitz et al.*, 2015].

The 2011 Tohoku-oki earthquake significantly affected the stress field in the frontal prism. Prior to the Tohoku event borehole breakouts measured at site 1151 of Ocean Drilling Program (Leg 186), located 83 km NNE of the Tohoku-oki earthquake epicenter, indicated the maximum horizontal stress orientation was roughly parallel to the plate convergence direction and the site was in a reverse faulting stress regime [*Lin et al.*, 2011]. However, following the earthquake, *Lin et al.* [2013] inferred a rotation in the stress field at the JFAST site to a normal faulting stress regime. Using focal mechanisms, *Hasegawa et al.* [2012] inferred a similar stress field rotation with the change from reverse faulting foreshocks and mainshock to normal faulting aftershocks. Collectively, the stress field changes indicate a nearly complete stress drop during the 2011 earthquake on the shallow portion of the décollement [*Lin et al.*, 2013].

3.3 Methodology

We targeted intervals of the JFAST drill core (C0019E) above and below the proposed location of the décollement to focus on structures that define and characterize the plate-boundary fault damage zone. To ensure that we examined enough core sections to characterize the damage zone, our study encompasses several tens of meters above and below the décollement, consistent damage zone width predictions for a fault with ~3.2 km of displacement [*Savage and Brodsky*, 2011]. We investigated cores 10R through 16R in the hanging wall (~770 – 820 mbsf) and cores 18R through 20R in the footwall (~824 – 833.5 mbsf) (Fig. 5c). Cores above 770 mbsf were not included in this analysis due to a ~45 m gap in recovery between cores 10R and 9R. All available cores in the footwall were analyzed. The total depth interval encompassed by these cores is 63.5 m with a total of 9.38 m of intact core in the hanging wall and 6.73 m of intact core in the footwall.

Structural analysis was performed on high-resolution images of core sections and verified with direct observation of archive core halves and X-ray computed tomography (X-CT) scans of core sections, available for download from the IODP data repository. A multi-scanner core logger (MSCL-I Digital Imaging System with GEOSCAN IV: GEOTEK) instrument collected high-resolution (100 pixels/cm) scans of all core archive halves during the JFAST expedition. Prior to core splitting, each section was also scanned by a X-CT imaging device (GE Yokogawa Medical Systems LightSpeed Ultra 16) that generated core-axis-normal planes of X-ray attenuation values with dimensions 512 x 512 pixels (0.188 mm x 0.188 mm) [*Chester et al.*, 2013a].

To distinguish natural tectonic deformation from induced damage we classified all core-scale structures based on our confidence in tectonic or induced origin. The classification scheme

includes three categories of structures: 1) unequivocally tectonic and *in situ*, 2) ambiguous or no evidence for either a tectonic or induced origin, and 3) induced by drilling, coring, and/or handling operations. The results presented here are limited to category 1 tectonic structures. For a complete review of the attributes used to distinguish tectonic and induced deformation in the JFAST core, see *Keren and Kirkpatrick* [in review].

The intensity of core-scale tectonic structures was quantified with a linear scanline sampling method on core photos with verification from direct observations of archive core halves. Structure intensity is defined here as a linear measurement of number of structures per unit length [*Zeeb et al.*, 2013]. A linear transect was drawn down the center of each examined core section, and the depths (in mbsf) of all tectonic structures intersecting the line were recorded. This sampling method is the recommended practice in borehole image logs and cores [*Zeeb et al.*, 2013], and has also been shown to document elevated damage in the vicinity of major faults at the outcrop scale [e.g. *Schulz and Evans*, 1998; *Vermilye and Scholz*, 1998; *Wilson et al.*, 2003; *Mitchell and Faulkner*, 2009; *Faulkner et al.*, 2011a; *Savage and Brodsky*, 2011]. Where the spacing between structures was ~0.5 cm or less (i.e. breccia zones), we approximated the intensity of structures within the zone by determining the average clast size. Assuming the boundaries of clasts within a breccia zone are fracture surfaces, the size of a clast is also a measure of fracture spacing. We implemented an image analysis technique in Matlab© following the methods of *Bjørk et al.* [2009] to separate individual grains and report average grain diameter (Appendix A1). Structure intensity was measured from the data by calculating the number of structures per meter of examined core (st/m), ensuring that the length of examined core was accurate by removing gaps >4 cm (typically locations of whole-round samples).

True dips of structures in the core reference frame were calculated from two apparent dips measured in different sections through the archive halves or X-CT imagery (Appendix A2). Rakes of slickenlines were measured in the core reference frame for structures that exhibited kinematic criteria. Where possible, we used orientation data that has been corrected using paleomagnetic constraints from coherent intervals of core [*Mishima et al.*, 2012; *Chester et al.*, 2013a]. Two apparent dip angles, and therefore true orientation data, could not be collected for the majority tectonic structures in the damage zone; however, the apparent dip of each structure transected by the linear scanline was measured as the rake of the structure in the split face of the archived core half. Kinematic indicators such as shear displacement of piercing points (i.e. marker beds) and crosscutting relationships were also recorded.

Microscopic deformation was characterized with petrographic microscope and scanning electron microscope (SEM) observations from 28 samples collected from coherent intervals of core sections 14R through 16R in the hanging wall, and sections 18R through 20R in the footwall. Three orthogonal thin sections were prepared from each sample, following the methodology of *Friedman* [1969] and *Anders and Wiltschko* [1994], among others. We quantified the intensity of microstructures in each thin section using a modified linear scanline sampling method. Since the JFAST samples are dominantly a mixture of micrometer sized clay, volcanic debris, and microfossils, we could not follow the procedures of *Anders and Wiltschko* [1994] or *Wilson et al.* [2003] that focus on counting intragranular fractures in 50+ quartz grains per thin section. Instead, we drew 10 randomly oriented linear scanlines across each thin section and counted the number of tectonic microstructures that intersected each line of known length (Appendix A3), similar to *Anders et al.* [2013]. Each scanline resulted in an intensity calculation in the form: number of microstructures per millimeter (ms/mm). The median microstructure

intensity (in order to avoid the assumption of a normal distribution) from each of the three orthogonal sections was averaged to obtain a representative value of microstructure intensity for each sample. Box and whisker plots of microstructure intensity calculations for each scanline were created to evaluate the distribution of the data between the three thin sections (Appendix A3).

3.4 Results

3.4.1 Deformation Structures

We identified six types of macroscopic tectonic structures in the JFAST core and four types of microstructures. Here, we briefly summarize the characteristics (morphology, textures, composition, etc.) of the five distinctive core-scale structures and three distinctive microstructures; the remaining tectonic structures were deemed mode I fractures. Mode I fractures are similar in core and thin section – straight to curvi-planar, open (no mineralization) fractures that commonly exhibit preferred orientations, but no indication of shear. Mode I microfractures were differentiated from cracks in the rock resulting from sample preparation by the presence of mineralized zones running parallel to a crack in the adjacent wall rock.

3.4.1.1 Core-scale structures

A small number of *secondary fault zones* with displacements greater than the diameter of the core (~7 cm) were observed in cores within ~5 m of the décollement. Secondary faults are several cm thick and contain fault rock interpreted to be gouge. We also identified secondary faults above the décollement by disrupted zones of densely arranged, mm-thick, dark grey to black seams (Fig. 6a), sometimes with evidence of shear being a lack of continuity of

stratigraphy across the seams [*Kirkpatrick et al.*, 2015]. Below the décollement, secondary faults zones were observed to contain phacoid-shaped lenses, the surfaces of which define a scaly fabric texture [e.g. *Cowan,* 1974; *Lundberg and Moore,* 1986; *Maltman,* 1998; *Kirkpatrick et al.*, 2015] and cut bedding.

Phyllosilicate bands, a subset of deformation bands with >10-15% platy minerals [*Fossen et al.*, 2007], are dark grey to black, mm-thick structures that typically form braided networks oblique to bedding with observed dips of ~20-80° (Fig. 6b). They have higher X-CT numbers (a normalized value of the calculated x-ray absorption coefficient of a pixel) than the surrounding rock, indicating relatively higher compaction (similar to "kink-like bands" observed by *Byrne et al.* [1993]). Grain-scale realignment is evident from crystallographic preferred orientations (CPO) within individual bands. Networks of closely spaced phyllosilicate bands also form few mm thick, dark zones with displacement typically less than the width of the drill core (Fig. 6c). Within the bands, there is minimal reduction in grain size and brighter color in backscattered scanning electron (BSE) images. Margins of bands vary from sharp outlines of opaque mineralization to gradational boundaries. Similar structures have been observed at the Japan Trench as "dark seams" [*Chester et al.*, 2013a], Nankai margin [e.g. *Lundberg and Karig*, 1986; *Maltman et al.*, 1993; *Maltman*, 1998; *Ujiie et al.*, 2004] and Chile margin [e.g. *Rochford et al.*, 1995].

Shear fractures commonly exhibit clear kinematic indicators such as displaced piercing points (e.g. marker beds or other tectonic structures) along single fracture surfaces and/or slickenlines or grooves on fracture surface planes. Displacement can range from a few mm (Fig. 6e) to several cm and possibly greater than the width of the drill core where only truncation is

noted. Significant changes in bedding orientation across an open fracture are also inferred to result from shear displacement.

Breccia zones are extensively fractured and contain clasts of sub-angular to angular sedimentary rock typically <1-2 cm long. In coherent sections of core they often grade to relatively undeformed rock (Fig. 6f). Breccia clasts are frequently striated and/or polished. Under optical microscope, thin zones of sub-angular clasts in a fine-grained cataclastic matrix separate larger clasts in breccia zones, providing further evidence for tectonic origin. *Arthur et al.* [1980], *Carson et al.* [1982], *Lundberg and Moore* [1986], *Maltman et al.* [1993], and *Maltman* [1998] recognize breccia zones in comparable settings.

3.4.1.2 Microstructures

Crystallographic preferred orientation (CPO) bands make up a large proportion of tectonic microstructures observed in JFAST core samples and these structures are the microscopic equivalent of core-scale phyllosilicate bands. They are defined by linear bands several tens of microns thick that contain phyllosilicate grains with a common extinction angle only visible under cross-polarized light (Fig. 7a). BSE images reveal CPO bands containing poorly expressed phyllosilicate fabric (Fig. 7b) compared to observations under an optical microscope, with the exception of deflection of phyllosilicate fabric around larger grains, similar to observations of *Lewis et al.* [1997] on “kink-like bands.” Here, we group the microstructures displaying any form of crystallographic preferred orientation, whether kink-like [e.g. *Lundberg and Moore*, 1986; *Maltman et al.*, 1993; *Lewis et al.*, 1997; *Vannucchi and Tobin*, 2000] or deformation bands [e.g. *Karig and Lundberg*, 1990; *Rochford et al.*, 1995; *Vannucchi and Tobin*, 2000; *Ujiie et al.*, 2004].

Displacement or truncation of piercing points, most commonly microfossils, is observed for a small number of microfractures or broader zones of microstructures that are classified as *shear microfractures* (Fig. 7c). Where measurable, offset is typically on the order of a few 100 μm. However, the majority of shear fractures are identified from truncation and offset is not quantifiable. Shear fractures, as with most open microfractures, are commonly bound by a halo of opaque-rich sediment in the wall rock. Similar structures have been described as "microfaults" [e.g. *Lindsley-Griffin et al.*, 1990; *Vannucchi and Tobin*, 2000] or "healed fractures" [*Carson et al.*, 1982]. Shear fractures, CPO bands, and/or mode I fractures collectively can make up broader zones of damage defined as *shear zones* (Fig. 7d).

Mineralized veins contain opaque iron oxide crystals in bands <100 μm wide. Veins vary from linear to wavy geometries, and can also be discontinuous or bend around large grains or microfossils. The majority of veins show no evidence for shear, however we observed select cases of shear displacement across veins and displacement of veins across other microstructures (Fig. 7e). Similar vein structures have observed in other forearc settings with different compositions [e.g. *Lundberg and Karig*, 1986; *Lindsley-Griffin et al.*, 1990]

3.4.2 Core-scale structure intensity

The linear scanline sampled 1,102 tectonic (category 1) structures and 3 secondary faults in the 16.11 m of examined JFAST core. Of the sampled structures, 30% are phyllosilicate bands, 24% are shear fractures, 40% are fractures in breccia zones, and 6% are mode I fractures. Structure intensity decreases with distance from the décollement (Fig 8a). In the hanging wall, structure intensity decreases from a maximum of 247 st/m at 2.4 m from the fault to a minimum of 21 st/m at 51 m from the fault. In the footwall, structure intensity decreases from a maximum

of 254 st/m at 3.2 m from the fault to 28 st/m at 11.4 m from the fault. The sharp decrease in structure intensity primarily occurs within 10 m of the décollement, and decreases more gradually with greater distance from the fault. Small variations in structure intensity occur at the locations of secondary faults with stratigraphic reversals or gaps (~817 and ~832 mbsf) [*Keren and Kirkpatrick*, in review].

Structure intensity in the hanging wall and footwall are both consistent with power law decay with distance from the fault using the equation:

$$d = cr^{-n} \quad (1)$$

where d is structure intensity (st/m), r is distance from the fault (m), n is the damage decay exponent, and c is an empirically estimated fault-specific constant. Our results show a steeper decay exponent n in the footwall ($n = 1.45 \pm 0.45$) relative to the hanging wall ($n = 0.70 \pm 0.11$; Fig. 8b). Large potential error in footwall n value is likely only due to small sample size (n = 6), but we also performed statistical tests of goodness of fit. Previous studies have shown that the decay in damage from faults can be fit by logarithmic or exponential functions [*Vermilye and Scholz*, 1998; *Mitchell and Faulkner*, 2009; *Savage and Brodsky*, 2011]. In order to evaluate the proper function to fit our data, we calculated Pearson linear correlation coefficients and associated *p*-values (a measure of the probability that the data would have arisen if the null hypothesis were true) for all three functions (Table 1). Largest correlation coefficients (r) and smallest *p*-values favor the power law function, consistent with models for stresses produced from a line or point source [*Love*, 1927], which is suggested to be a sensible model of damaging fault slip [*Savage and Brodsky*, 2011].

Table 1: Statistical tests for quality of fit[a]

[a]Correlation coefficient calculates the Pearson linear correlation coefficient (*r*), resulting in a value ranging from -1 to 1. An *r* of -1 indicates a perfect negative linear relationship, an *r* of 0 indicates no linear relationship, and an *r* of 1 indicates a perfect positive linear relationship.

Scale of Observation	Fault Block	Function	Correlation Coefficient (*r*)	*p*-value	Sample size
Core-scale structures	Hanging Wall	Power Law	0.971	3.2E-6	10
		Exponential	0.802	5.2E-3	
		Logarithmic	0.893	5.0E-4	
	Footwall	Power Law	0.945	4.4E-3	6
		Exponential	0.863	2.6E-2	
		Logarithmic	0.843	3.5E-2	
Microstructures	Hanging Wall	Power Law	0.677	7.8E-3	14
		Exponential	0.726	3.3E-3	
		Logarithmic	0.710	4.5E-3	
	Footwall	Power Law	0.889	2.2E-5	14
		Exponential	0.869	5.4E-5	
		Logarithmic	0.869	5.4E-5	

3.4.3 Microstructure intensity

Microstructure intensity also decreases with distance from the fault (Fig. 8c). In the hanging wall, microstructure intensity decreases from a maximum of 1.1 ms/mm at ~2 m above the fault to a minimum of 0.34 ms/mm at ~11 m from the fault. The sample closest to the fault (1.8 m) has a microstructure intensity of 0.94 ms/mm, slightly lower than the peak value. In the footwall, microstructure intensity decreases from a maximum of 2.1 ms/mm at ~2 m from the fault to a minimum of 0.31 ms/mm at ~10 m below the fault. Six samples with microstructure intensity between ~0.7 and ~1 ms/mm cluster around a secondary fault at 817.5 mbsf. Other depths of samples with abnormally large microstructure intensity, perhaps due to proximity with a secondary fault or microscopic shear zone (e.g. Fig. 7d) include 826.9 and 832.4 mbsf.

Power law functions fit to the microstructure intensity data show a steeper damage decay exponent *n* in the footwall ($n = 1.09 \pm 0.16$) relative to the hanging wall ($n = 0.50 \pm 0.14$; Fig. 8d). Including all microstructures in the hanging wall, correlation coefficients slightly favor an exponential fit, but all *p*-values are of an equal order of magnitude. In the footwall, correlation coefficients slightly favor a power law fit, but all *p*-values are of an equal order of magnitude.

Equal magnitude, very small *p*-values suggest all functions are statistically significant fits to the data, thus we fit all microstructural data with a power law function for consistency with core-scale data, recognizing an exponential fit may be slightly more appropriate in the hanging wall.

3.4.4 Core-scale structure orientations

True dip angles of 152 of 1,085 tectonic structures in the examined core sections show no apparent trends with depth (Fig. 9a). Measured dip angles in nearly every core section range from ~10° to ~70°. The exceptions to this observation are core sections 10R-1 and 10R-2 (~770 mbsf) where the majority of measured dip angles are greater than 50°. Overall, the dip data show roughly constant frequency of structures dipping ~10° to ~70°, with the highest frequency at ~40° (Fig. 9b). Rakes measured in the split core face also show no preferred orientation (Appendix A4).

Kinematic criteria were used to distinguish shear structures and, where possible, normal and reverse sense of shear. Dip angles of shear structures in the hanging wall are consistently between ~10° and ~80°, with the exception of measurements at ~770 mbsf, where dips are >50°. In the footwall, dip angles of all shear structures remain scattered, but range from ~30° to nearly 90°. Normal and reverse structures display no consistent change in shear sense with depth. Additionally, we observed anomalously high dips for reverse shear structures and low dips for normal shear structures. Crosscutting relationships at 25 locations show mutually crosscutting reverse and normal structures at all depths.

True strike was found using available paleomagnetic data from coherent intervals of core for 64 of the 152 structures with measured true dip angles. The data shows no clustering of structures in distinct orientation sets for either the hanging wall or footwall (Fig. 9c). The best-fit great circle to corrected orientations strikes 288°, nearly parallel to the convergence direction of

the Pacific Plate at the Japan Trench (298°), but the scatter around this great circle is considerable.

3.5 Interpretation

3.5.1 Damage zone characteristics

We estimated the total fault zone thickness at the JFAST site from the changes in structure intensity with distance from the décollement. Core-scale and microstructure intensity data in the hanging wall and footwall do not decay to constant values within our dataset, so the background level of deformation is unknown. *Savage and Brodsky* [2011] examined structures in mudstone and determined a background intensity of ~9-15 st/m, slightly smaller than the minimum reached in our examined cores, however the faults are isolated continental normal faults and are likely not comparable. Core-scale structure intensity decreases sharply to a level of ~75 st/m within ~10 m above the décollement and ~5 m below, and decreases less steeply further than the fault. We use this background value as an approximation for the minimum fault zone thickness (fault core + damage zone [e.g. *Caine et al.*, 1996]) of ~18 m. If the background level is reached at the outer limits of the studied interval (~25 st/m), we estimate the maximum fault zone thickness is at least the width of examined core-scale structures (~65 m). The maximum fault zone thickness could be even greater if the background level was not reached in the cores furthest from the décollement. Similar considerations for the microstructure intensity yield slightly different estimates of fault zone thickness. If the background level is ~0.5 ms/mm, the minimum fault zone thickness is ~10 m, but a background value of ~0.3 ms/mm suggests the thickness is ~23 m. The background level may not be captured in our microstructure dataset, in which case the fault zone thickness is greater than ~23 m. The combined scales of observation

suggest an approximation for total fault zones thickness on the order of a few to several tens of meters with an absolute minimum thickness of ~10 m.

The structural orientation data indicate structures dipping >70° are underrepresented (Fig. 9a,b), a sampling bias predicted for sub-vertical cores [e.g. *Terzaghi*, 1965]. Correction factors have been designed to eliminate this bias from measurements of the frequency of structures in cores or outcrops [e.g. *Terzaghi*, 1965; *Mauldon and Mauldon*, 1997; *Peacock et al.*, 2003; *Davy et al.*, 2006; *Peacock*, 2006]. However, correction factors require the acute angle between the line normal to each structure and the scanline, and therefore the true dip angle of each structure, which is not available for the majority of our data. Correction factors can also be applied to sets of structures with common orientations [e.g. *Peacock et al.*, 2003], but we observed no clusters in any of the structural orientation data (Fig. 9c), eliminating the possibility of defining representative orientations and applying correction factors to each set. Any correction factor would result in a significant increase in steeply dipping structures, consequently increasing the intensity of structures in each core section [e.g. *Johri et al.*, 2014b]. Since each core section has approximately the same distribution of dips and rakes (Appendix A4), any correction factor would uniformly increase structure intensity in each core [*Peacock et al.*, 2003]. Thus, the application of a correction factor to our data likely would only change the peak structure intensity, but not the damage decay exponents or damage zone thickness.

Our data indicates that some of the damage zone characteristics at the JFAST site are distinct compared to observations of faults with similar displacement. *Savage and Brodsky* [2011] compiled damage zone decay exponent and thickness data from faults of all rock types to investigate the scaling of fault damage with displacement. Our evaluation of a total fault zone thickness on the order of several tens of meters, with a minimum of ~10 m, is comparatively

narrow, but within the range of values observed for similar displacement faults (Fig. 10a). Significantly, both core- (Fig. 10b) and micro-scale (Fig. 10c) measurements of the damage decay exponent (*n*) in the footwall are substantially greater than previously observed values from similar displacement faults. Hanging wall damage decay exponents are less than the footwall, perhaps because the frontal prism has undergone more displacement (though this is unconstrained). If so, the hanging wall damage decay exponents for core-scale (Fig. 10b) and microstructure (Fig. 10c) observations are roughly within the expected range of values for a displacement slightly >3.2 km.

3.5.2 Role of friction

Our observations of large damage decay exponents and a comparatively narrow damage zone thickness are distinct for faults with ~3.2 km of displacement. Previous studies have demonstrated the coseismic friction coefficient (μ_d) on the décollement is low ($\mu_d < 0.1$) [*Fulton et al.*, 2013; *Ujiie et al.*, 2013; *Sawai et al.*, 2014], raising the possibility that the static fault friction coefficient is a primary control on the damage zone characteristics.

We investigated if the damage zone characteristics at the JFAST site are sensitive to low static fault friction using a 2-D elastic perturbation model [*Saucier et al.*, 1992; *Johnson and Fletcher*, 1994; *Chester and Fletcher*, 1997; *Chester and Chester*, 2000]. The décollement was modeled as a wavy, frictional interface in an isotropic linear elastic medium. In this model, deformation results from stress perturbations due to a uniform far-field shear displacement applied to the sinusoidal fault surface of amplitude *A* and wavelength *L*. The total stress field is calculated by summing the stress required to initiate slip on a frictional planar fault surface, and stresses produced by perturbations from the rough fault surface. The solutions for the total stress

field about a fault aligned with the *x* axis and perturbed around the *z* = 0 plane are given in terms of the Cartesian components of the stress tensor in equations (7a)-(7c) of *Chester and Chester* [2000]:

$$\sigma_{xx} = \bar{\sigma}_{xx} + Ale^{-lz}\left\{\left[\frac{UEl}{4(1-v^2)}\right](-1+lz)\cos(lx) + \left[\bar{\sigma}_{zz}(1-k+2\mu^2) - \frac{\mu UEl}{4(1-v^2)}\right](-2+lz)\sin(lx)\right\} \quad (2a)$$

$$\sigma_{zz} = \bar{\sigma}_{zz} + Ale^{-lz}\left\{\left[\frac{UEl}{4(1-v^2)}\right](-1-lz)\cos(lx) + \left[\bar{\sigma}_{zz}(1-k+2\mu^2) - \frac{\mu UEl}{4(1-v^2)}\right](-lz)\sin(lx)\right\} \quad (2b)$$

$$\sigma_{xz} = \bar{\sigma}_{xz} + Ale^{-lz}\left\{\left[\frac{UEl}{4(1-v^2)}\right](-lz)\sin(lx) + \left[\bar{\sigma}_{zz}(1-k+2\mu^2) - \frac{\mu UEl}{4(1-v^2)}\right](-1+lz)\cos(lx)\right\} \quad (2c)$$

where $\bar{\sigma}_{ij}$ are the far-field background stresses (Pa), *l* is the wave number, *U* is shear displacement (m), *E* is Young's modulus (Pa), *v* is Poisson's ratio, *k* is the ratio $\bar{\sigma}_{xx}/\bar{\sigma}_{zz}$, and μ is the static fault friction coefficient. The model is simple in the sense that faults are considered to be infinite length, no separation of fault walls is prescribed, and the host rock is a homogenous, isotropic media.

We tailored the model parameters to approximate the conditions of faulting in the shallow portion of the Japan Trench décollement. To represent low effective stress at the JFAST site, maximum principal compressive stress σ_{max} was set to 4 MPa, in the range of estimates of the effective normal stress (~2-7 MPa) calculated from the lithostatic stress acting on the fault and hydrostatic pore pressure [*Chester et al.*, 2013a; *Fulton et al.*, 2013], as well as effective

normal stresses applied in friction experiments on the fault rock [*Ujiie et al.*, 2013; *Ikari et al.*, 2015]. The angle α between σ_{max} and the fault surface was 10°, parallel to the maximum principal compressive stress direction in an Andersonian stress field along a low angle reverse fault. Using appropriate values for ~1 km depth of faulting, we assigned Young's modulus E = 3 GPa, Poisson's ratio ν = 0.25, and roughness ratio $A/L = 10^{-3}$ [*Power et al.*, 1987; *Power and Tullis*, 1991]. Static fault friction was initially set to μ = 0.1 to model a frictionally weak fault [*Ujiie et al.*, 2013; *Ikari et al.*, 2015], and later adjusted to examine the effects of friction.

We first explored the stress distribution along a 100 m wavelength (L) of the modeled décollement with a total displacement (U) of 50 m to explore the effects of a slip increment similar to the 2011 Tohoku-oki earthquake. The greatest mismatch of the two displaced surfaces and maximum associated perturbed stresses occur at $U = L/2$. In the case of a frictionally weak fault (μ = 0.1), large variations in the magnitudes and orientations of local principal stresses occur within ~50 m of the fault surface (Fig. 11a). The degree of variation in stress magnitudes and orientations decreases with greater fault friction [*Chester and Chester*, 2000]. The largest compressive stresses occur towards the edges of the model near restraining bends, whereas the largest tensile stresses occur towards the center of the model near the releasing bend. The observation of no preferred structure orientation throughout the examined JFAST cores may be explained by the large variation in local stress orientations due to the geometry of the fault.

To assess the sensitivity of friction on fault damage zone thickness, we assume the stress distributions from the elastic model approximate stresses just before brittle failure [e.g. *Hafner*, 1951; *Sanford*, 1959; *Chester and Fletcher*, 1997; *Chester and Chester*, 2000]. We combined the modeled stress field with a Coulomb failure criterion (Appendix A5) [*Jaeger et al.*, 2007] for the clay-rich sediments surrounding the décollement expressed in terms of the principal stresses:

$\sigma_2 = -T_o$, if $\sigma_1 + 3\sigma_2 < 0$ (3a)

$(\sigma_1 - \sigma_2)^2 = 8T_o(\sigma_1 + \sigma_2)$, if $\sigma_1 + 3\sigma_2 > 0$ and $\sigma_1 < 2T_o[\tan^{-1}(\beta)]$ (3b)

$\sigma_1 = 2\tau_o[(1 + \mu_i^2)^{1/2} + \mu_i] + [(1 + \mu_i^2)^{1/2} + \mu_i]^2 \sigma_2$, if $\sigma_1 > 2T_o[\tan^{-1}(\beta)]$ (3c)

where cohesion τ_o is 1 MPa (derived from unconfined compressive strength in *Chester et al.* [2013a]), tensile strength T_o is ½(τ_o), coefficient of internal friction μ_i is 0.8, σ_1 and σ_2 are the two in-plane principal stresses, and β = 45° + ½(ϕ), where ϕ is the angle of internal friction (see Table 2 for a complete list of model parameters). The predicted region of failure is a proxy for damage zone thickness on one side of the fault and increases in size and distance from fault with an increase in fault friction (Fig. 11b), consistent with *Chester and Chester* [2000]. At μ = 0.1, the thickness of the modeled damage zone is predicted to be ~50 m on either side of the fault, whereas at μ = 0.6 the modeled damage zone thickness is nearly 100 m. The shape of the failure region increases in width (distance along fault) for a weak fault, due to a small increase in compressive failure towards the fault restraining bends. We increased the angle α to 20° [*Mitsui et al.*, 2012] and observed the same relationship between failure region thickness and fault friction (Fig. 11c). With an increase in α, the extent of deformation decreases and the width of failure regions increase.

Table 2: Analytical model parameters

Model Parameter	**Assigned Value**
Maximum principal compressive stress (σ_{max})	4 MPa
Angle between σ_{max} and fault (α)	10°
Young's modulus (E)	3 GPa
Poisson's ratio (v)	0.25
Wavelength (L)	100 m
Roughness ratio (A/L)	3E-3
Shear displacement (U)	50 m
Static fault friction coefficient (μ)	Variable
Cohesion (τ_o)	1 MPa
Tensile strength (T_o)	0.5 MPa
Coefficient of internal friction (μ_i)	0.8

To test the effect of friction on the structure intensity decay, we summed the regions of brittle failure resulting from one increment of slip on an ensemble of self-similar wavelengths. In this approach, the model length was fixed at 100 m, but the wavelengths within the model ranged from 100 to 10 m. The distance of perturbed stresses generated off fault scales with wavelength [e.g. *Chester and Fletcher*, 1997]. We fixed displacement on all wavelengths at 5 m, representing the maximum mismatch slip for the smallest wavelength in the model (10 m), and summed the regions of failure from each model realization. Previous studies using a similar analytical model have shown that small increments of slip generate off fault failure, suggesting the use of a small slip increment is reasonable [*Sagy and Brodsky*, 2009].

A fault with a low static friction coefficient (μ = 0.1) results in a steeper decay in the frequency of deformation with distance off fault compared to a high static friction (μ = 0.6) fault (Fig. 12). The results show heavily tailed distributions. Close to the fault this is due to the finite resolution of the model. Far from the fault, the small slip increment means limited failure. We suggest the steeper decay in deformation on a low friction fault is the result of regions of failure on progressively smaller wavelengths increasing in width (distance along fault or x-axis), but only slightly decreasing in thickness. In contrast, the modeled high friction fault failure regions decrease in width and thickness more uniformly with decreasing wavelength (i.e. the shape does not change). This difference arises because of very high differential stresses near restraining bends on the low friction fault, and therefore more failure in compression and extension of the failure region width. Others have also noted slip on "lubricated" (μ = 0) wavy faults produces very high differential stresses at contractional bends [*Griffith et al.*, 2010]. The modeled slopes are much greater than the values measured in the JFAST core due to the small increment of slip, preventing deformation from reaching the full extent off fault. The results are consistent with

static fault friction controlling the shapes of failure regions that change with variations in wavelength, and as a result, the rate of decay of failure frequency with distance from the fault is also sensitive to fault friction.

3.6 Discussion

We suggest that our measurements of the damage zone surrounding the shallow Japan Trench décollement indicate low fault friction over geologic time, consistent with *Yang et al.* [2013]. Previous models of damage zone stresses related friction to damage zone thickness, decay exponents, and structure orientations [*Lyakhovsky et al.*, 1997; *Chester and Chester*, 2000; *Faulkner et al.*, 2006; *Griffith et al.*, 2010; *Savage and Cooke*, 2010; *Johri et al.*, 2014a]. However, no single study accounts for the effect of long-term friction on all three damage zone characteristics measured in this study. Although our modeling approach was extremely simplified, the results provide insights into damage localization around weak faults with implications for damage zone scaling and subduction zone mechanics.

3.6.1 Model limitations

The analytical model we used in this study contains several important assumptions that could affect the results [*Chester and Chester*, 2000]. The model does not account for opening normal to the fault, non-uniform friction, displacement gradients, influence of fault tips, fractal fault geometries, pore fluid pressure variability, or syn-kinematic mineral precipitation [e.g. *Dieterich and Smith*, 2009; *Griffith et al.*, 2010; *Ritz and Pollard*, 2012]. However, it does provide a framework with which to investigate the role of friction on off-fault stresses and damage patterns in an elastic medium. This simplification does account for changes in elastic moduli in the damage zone resulting from inelastic deformation [e.g. *Xu et al.*, 2014]. We lack

information describing the 3-D roughness of the Japan Trench décollement, so the 2-D fault geometry used instead is a simplification. Irregularities on natural faults may lead to opening, but the no-separation boundary condition of the *Chester and Chester* [2000] model promotes off-fault tension rather than opening. As a consequence, low friction faults will perturb stress more than high friction faults in order to maintain the no-separation boundary condition. The degree of opening has been shown to increase with a decrease in fault friction coefficient [*Ritz et al.*, 2015], yet models allowing opening normal to the fault still observe the largest changes in off-fault stress magnitudes and orientations on faults with a low static friction coefficient [*Griffith et al.*, 2010]. The analytical model does not specifically address self-similar fault surfaces. By integrating predicted failure regions for an ensemble of self-similar wavelengths with a small fixed displacement, we have evaluated the effects of fault roughness in a more simplified way. *Ritz and Pollard* [2012] showed that a local perturbation in shear stress occurs at fault tips, but as the fault-adjacent stress perturbation increases and ultimately dominates, the effect of fault tips becomes relatively less significant. Here, we only address the fault-adjacent stress perturbations as they have the largest effect on damage zone thickness. Syn-kinematic mineral precipitation [e.g. *Kennedy and White*, 2001] could also affect frictional properties faults, however this phenomenon is not well documented in the shallow crust and is not incorporated into the analytical model.

Several of the model parameters we used were not derived from measured quantities (roughness) or were set within a range of measured values (σ_{max}, U, α, failure criteria). Varying each of these parameters has a smaller effect than changing the fault friction, except for the background stress. An increase in background stress results in a larger brittle failure region around high friction faults ($\mu = 0.6$), but a smaller brittle failure region around low friction faults

(μ = 0.1). This is because the background stress term ($\overline{\sigma_{zz}}$) in equations 2a – 2c is scaled by (1 – k + 2μ^2). By squaring μ, low and high friction faults will result in an order of magnitude difference in (1 – k + 2μ^2). Therefore when μ is low, the perturbed stress will not increase at a rate greater than the background stress, resulting is less failure. However, we kept the background stress constant in all analyses, and therefore any interpretations are not biased by this effect.

We aimed to optimize the input parameters to best match the conditions of faulting at the JFAST site and isolate the role of friction on off-fault stress and deformation. The modeling results do not replicate the measured damage zone thickness, decay exponents, or structure orientations, but we suggest the sensitivity of those characteristics to static fault friction is robust.

3.6.2 Damage localization and scaling

Structures in the JFAST core suggest the processes controlling damage zone growth are highly localized around the décollement. Clay-rich faults, including the shallow Japan Trench décollement, change from velocity-strengthening to velocity-weakening behavior at coseismic slip rates [*Faulkner et al.*, 2011b; *Ferri et al.*, 201l; *Tsutsumi et al.*, 2011; *Ujiie et al.*, 2013; *French et al.*, 2014; *Sawai et al.*, 2014; *Oohashi et al.*, 2015]. Significantly, the Japan Trench fault rocks are also statically weak [*Ikari et al.*, 2015]. *Beeler et al.* [1996] suggested fault strength controls the degree of slip localization in a PSZ, rather than the velocity dependence of friction. We propose fault strength (friction coefficient) also controls the degree of damage localization.

Figure 13 is a schematic representation of core-scale damage zone characteristics, demonstrating the mutual dependency of thickness, critical (maximum) structure intensity, and damage decay exponent. The effect of friction on damage zone thickness was established by *Chester and Chester* [2000], and our results suggest the damage decay exponent may also be

related to friction where critical structure intensity is reached near fault. Considering the rocks adjacent to the décollement are intensely, but locally brecciated, the critical core-scale structure intensity may be approximated by the measured values in core sections 16R and 18R (~250 st/m). If critical structure intensity has been reached, then the comparatively narrow estimated damage zone thickness (a result of low fault friction) necessitates the damage decay exponent (*n*) will be greater than the predicted value (Fig. 13). In this sense, another fault with a similar critical structure intensity and greater damage zone thickness (a result of greater fault friction) will inevitably have a smaller damage decay exponent. Critical intensity of structures is independent of fault length [*Vermilye and Scholz*, 1998] and displacement [*Mitchell and Faulkner*, 2009], but dependent on lithology and modal mineralogy. Thus, frictionally weak faults will exhibit more localized damage zone deformation and larger damage decay exponents in comparison with frictionally strong faults of the similar host lithology and displacement.

Assuming long-term fault friction does influence damage zone characteristics, we can begin to evaluate possible related patterns in damage zone scaling. Damage zone thickness has been shown to positively correlate with fault displacement [e.g. *Faulkner et al.*, 2011a; *Savage and Brodsky*, 2011], with a decrease in the rate of increase in damage zone thickness above ~2400 m offset. The data from *Savage and Brodsky* [2011] is scattered due to comparisons of faults in different host lithologies and faulting regimes and/or variations in measurement methods, but our data fits the low-end of damage zone thickness predictions for ~3.2 km displacement (Fig. 10a). Our results suggest variable friction may cause deviations from the typical scaling patterns. Faults on the low-end of damage zone thickness predictions may be frictionally weak, whereas faults on the high-end of thickness predictions may be frictionally strong. In addition to friction, host lithology and its state of lithification could also explain scatter

in thickness-displacement scaling. *Heynekamp et al.* [1999] reported damage zone thickness increases with average grain size, implying the clay-rich composition of shallow Japan Trench host rock likely also contributed to a comparatively narrow damage zone thickness compared to scaling predictions. Finally, changes in strain distributions on transects across faults due to macroscopic fault zone complexity could influence damage zone thickness [*Childs et al.* 2009]. The 1-D scanline sampling method employed in this study does not capture that variability.

The scaling of damage decay exponents with displacement may also be sensitive to fault friction and host lithology. *Savage and Brodsky* [2011] suggested damage decay exponents in all settings are relatively constant ($n \approx 0.8$) for smaller faults (displacement < ~150 m), and then gradually decrease with increasing displacement as deformation delocalizes (Fig. 10b,c). Our observation of smaller damage decay exponents in the hanging wall compared to the footwall agrees with the interpretation that n decreases with increasing displacement. However, the steep damage decay exponents ($n > 1$) in the footwall suggest the initial n at low displacements (~0.8) and point where n begins to decrease with increasing displacement (~150 m) may vary for faults in different settings. Frictionally weak faults could generate larger damage decay exponents than scaling predictions, whereas frictionally strong faults may generate smaller damage decay exponents. Other anomalously high damage decay exponents have been observed in joint-dominated fault systems, where complex linking patterns in splay joints, sheared joints, and breccia blocks near fault control the steep fall-off [*Davatzes et al.*, 2003]. The displacement required to form such a pattern may still partially depend on fault friction [*Davatzes et al.*, 2003]. Host lithology could also contribute to scatter in decay exponent-displacement scaling by governing the critical structure intensity (Fig. 13).

Our observation of no preferred structure orientations in the damage zone implies large rotations in the stress field occurred around the Japan Trench décollement. This could be explained by regional stress field rotations, predictions of local stress perturbations around a non-planar fault, and/or stress rotations predicted for critically tapered wedges. Focal mechanisms indicate regional stress field rotations between reverse and normal faulting regimes are caused by large seismic slip [e.g. *Hasegawa et al.*, 2012]. *Chester and Chester* [2000] and *Griffith et al.* [2010] noted a decrease in static fault friction resulted in an increase in angular variation of maximum compressive stress in the damage zone. Since we observed a wide range of structure dip angles and mutually crosscutting low and high dip structures within 10s of meters of the décollement, and within the region of stress perturbation predicted by the model, we suggest the fault geometry may be a key cause of the variation in orientations near the décollement, but regional stress field rotations from seismic slip could also contribute.

Asymmetric distribution of structure intensity and damage zone thickness has been observed in faults of all types [e.g. *Heermance et al.*, 2003; *Berg et al.*, 2005; *Dor et al.*, 2006; *Caine and Minor*, 2009]. In the JFAST core, elevated smectite is observed in the footwall units, which decays below the décollement in a similar fashion to our structure intensity data [*Kameda et al.*, 2015, their Fig. 2]. Smectite retains water and is highly porous, resulting in structurally weaker strata with increasing smectite content [e.g. *Vrolijk*, 1990]. Sliding friction measured in the laboratory also reveals the underthrust sedimentary units are mechanically weaker than the hanging wall [*Ikari et al.*, 2015]. Elevated smectite content may therefore contribute to a narrower footwall damage zone [*Heynekamp et al.*, 1999]. Our results also demonstrate a potential positive correlation between smectite content and structure intensity in the footwall.

Elevated smectite content below the décollement could be a primary cause of the asymmetric damage zone characteristics.

Dynamic rupture models predict off-fault deformation suggesting coseismic structures may also contribute to the damage zone characteristics we observed. Dynamic rupture models predict logarithmic or power law decay in coseismic damage away from faults [*Ampuero et al*., 2008; *Johri et al.*, 2014a], but typically fix the properties describing frictional strength and stability in order to avoid a stress singularity and infinite strains at the propagating rupture tip. If a portion of the damage zone deformation observed in the JFAST core is coseismic, our results demonstrate that dynamic processes governing off-fault damage are also localized within several meters of the fault. The results may also indicate the thickness of coseismic damage is less than that formed during fault growth [*Faulkner et al.*, 2011a]. *Johri et al.* [2014a] modeled damage decay exponents around buried thrust faults experiencing a Gutenberg-Richter distribution of earthquake magnitudes. The results showed n = ~0.85 within ~10 m of the fault and $n > 1$ a few tens of meters from the fault, with the change in slope perhaps due to the small number of large magnitude events and related damage. As the fault rock at the JFAST study site is velocity-strengthening at low slip rates, few small, local earthquakes would be expected to have occurred. The steep damage decay exponents in the footwall of the décollement may indicate the plate-boundary fault only hosted large magnitude earthquakes in the past.

3.6.3 Implications for décollement mechanics

Several mechanisms have been proposed for the extraordinary shallow coseismic slip during the 2011 Tohoku-oki earthquake. Rupture propagation to the trench may have been facilitated by strain accumulation due to subducted seamounts [*Kennett et al.*, 2011; *Matsubara*

and Obara, 2011; *Duan*, 2012]. Alternatively, the reflection of seismic waves in the subduction wedge may have caused large transient stress changes on the fault [*Huang et al*., 2012], and possibly driven rupture regardless of the frictional stability of the shallow fault zone [*Kozdon and Dunham*, 2013]. Dramatic frictional weakening and low shear resistance at coseismic slip rates are observed in rock friction experiments [*Ujiie et al.*, 2013; *Sawai et al*., 2014] and may explain the anomalous slip [*Shibazaki et al*., 2011; *Mitsui et al.*, 2012; *Noda and Lapusta*, 2013; *Cubas et al*., 2015]. Others propose large stress changes on the shallow décollement resulted in dynamic overshoot caused by conditions within the seismogenic zone [*Ide et al*., 2011].

Our measurements of the décollement damage zone do not provide any indication that the décollement was frictionally strong at any stage over the seismic cycle. A frictionally strong fault would have damage zone thickness more than a few tens of meters, small damage decay exponents as damage is more delocalized, and preferred structure orientations. As the damage zone integrates deformation throughout the displacement history of the décollement, all the damage zone properties are consistent with long-term frictional weakness at the JFAST site. Lack of resolution makes interseismic strain accumulation models on the shallow fault zone challenging [*Hashimoto et al.*, 2009; *Loveless and Meade*, 2011], however recent onshore and offshore geodetic measurements suggest an increase in seismic coupling several hundred kms NNE and SSW of the JFAST site along strike [*Sato et al*., 2013; *Perfettini and Avouac*, 2014]. Therefore, the signature of long-term frictional weakness recorded in the damage zone in the JFAST core may best represent the maximum Tohoku-oki earthquake slip region of the shallow Japan Trench (Fig. 5). Nevertheless, mechanisms for shallow coseismic slip in which the shallow fault zone accumulates significant elastic strain energy [*Kato and Yoshida*, 2011; *Kennett et al*., 2011; *Matsubara and Obara*, 2011; *Koge et al.*, 2014] are inconsistent with the observed damage

zone properties. If our interpretations are correct, great earthquakes like the 2011 M_w 9.0 Tohoku-oki event could rupture to the trench without a shallow strong patch.

3.7 Conclusion

Damage zone structures observed in core from around the shallow Japan Trench décollement provided a unique opportunity to assess long-term frictional strength at an active subduction margin. We show that the coefficient of friction on the décollement is a primary control on the damage zone thickness, exponents describing the decay in intensity of structures from the fault, and rotations in the local principal stresses around a rough fault. The Japan Trench damage zone is comparatively narrow to similar displacement faults, and is characterized by steep decay exponents and a wide range of structure orientations. These properties develop over the history of faulting and record the long-term frictional strength of the fault. Tests of damage zone property's sensitivity to changes in static fault friction coefficient indicate the distinct JFAST damage zone characteristics are consistent with long-term frictional weakness. This interpretation suggests scatter in damage zone thickness and decay exponent scaling with displacement may be a in part result of variability in long-term friction on different faults. Where displacement and host lithology are approximately equivalent, changes in damage zone characteristics may indicate predictable variance in static coefficient of friction. If the shallow décollement is frictionally weak over geologic time, earthquake propagation to the trench similar to the 2011 Tohoku-oki earthquake does not require a shallow strong patch of the fault.

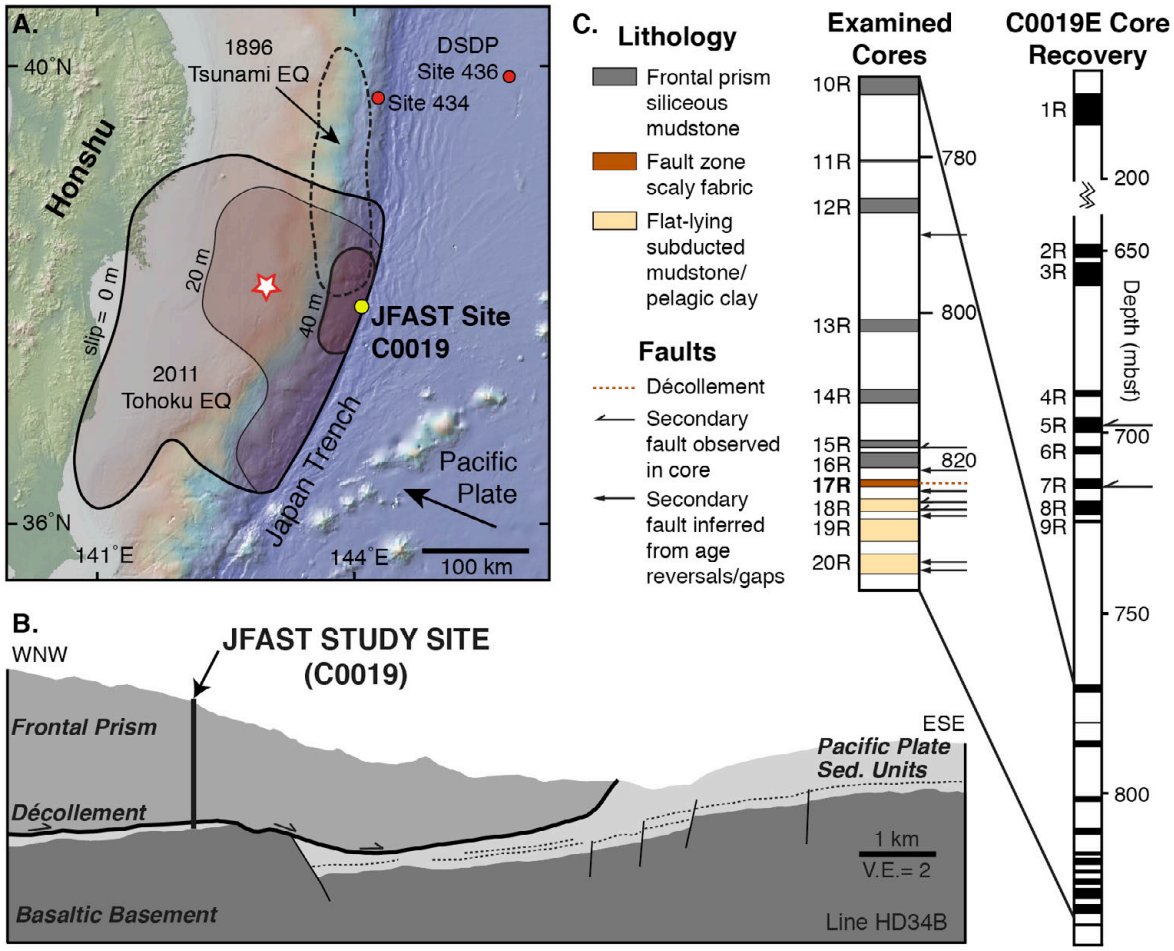

Figure 5: A) Location map of JFAST Site C0019 at the Japan Trench. Bathymetry and 2011 Tohoku-oki earthquake slip contours shown [modified after *Chester et al.*, 2013b]. Earthquake epicenter denoted by red and white star. Pacific Plate arrow represents plate convergence direction. B) Cross-section through seismic survey line HD34B (500 m N of site C0019) [*Nakamura et al.*, 2013], roughly parallel to plate convergence direction [modified after *Kirkpatrick et al.*, 2015]. C) Hole C0019E core recovery summary [modified after *Chester et al.*, 2013a], with zoomed in view of the cores studied here, locations of décollement, secondary faults, and lithology [after *Chester et al.*, 2013a; *Kirkpatrick et al.*, 2015; *Rabinowitz et al.*, 2015].

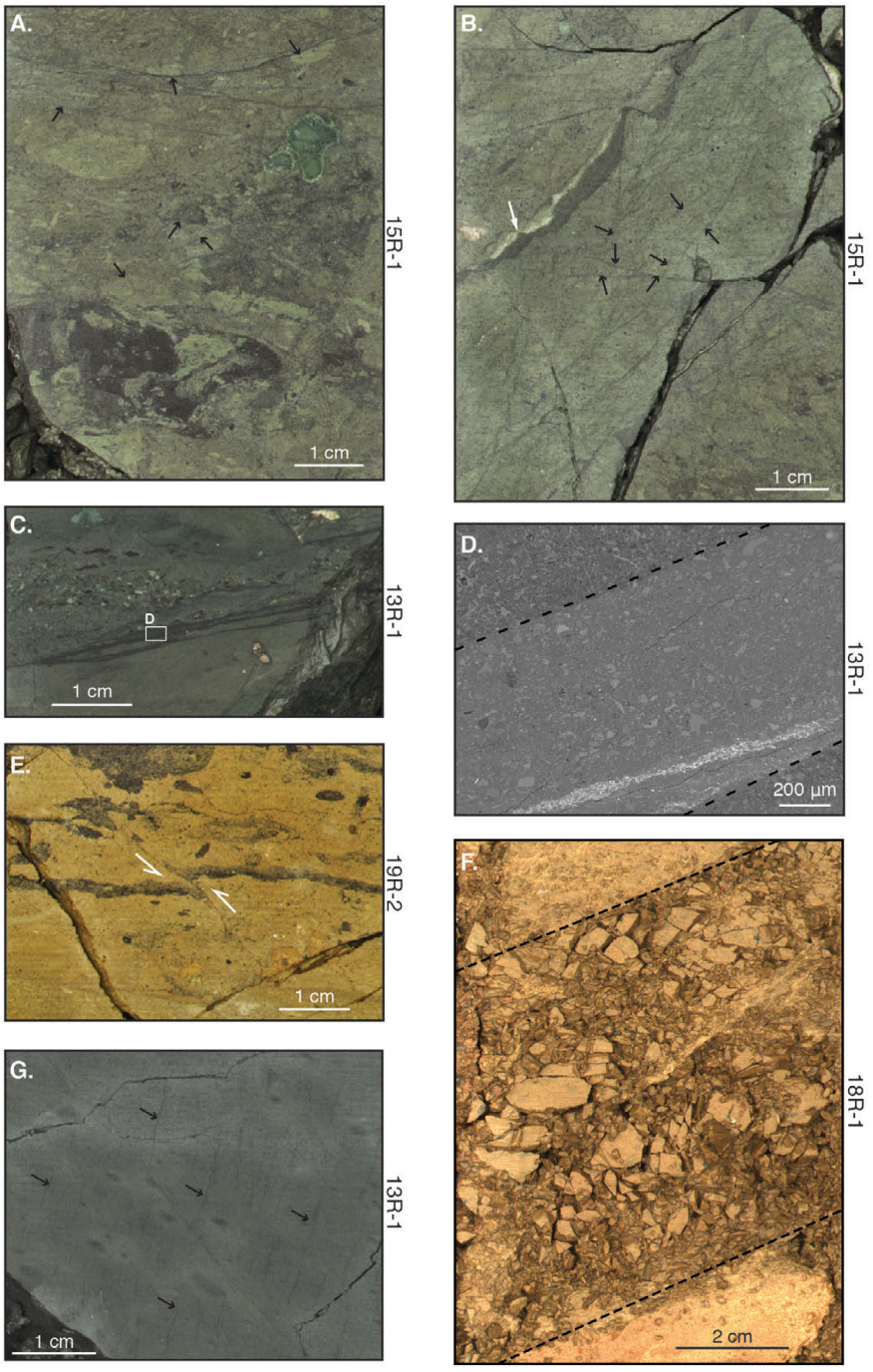

Figure 6: Types of core-scale structures included in linear scanline sampling. A) Secondary fault zone, with characteristic disrupted mudstone appearance. Black arrows denote locations of lack of mudstone continuity across dark bands; B) Phyllosilicate bands, examples denoted by black arrows, commonly displaying shear offset of bedding markers (white arrow); C) Network of phyllosilicate bands forming shear band (white box indicates location of D); D) Back-scattered electron (BSE) image of phyllosilicate band with slightly brighter appearance and sharp boundary (black dashed lines); E) shear fracture; F) breccia zone, bound by soft clay; and G) sediment-filled veins (examples denoted with black arrows).

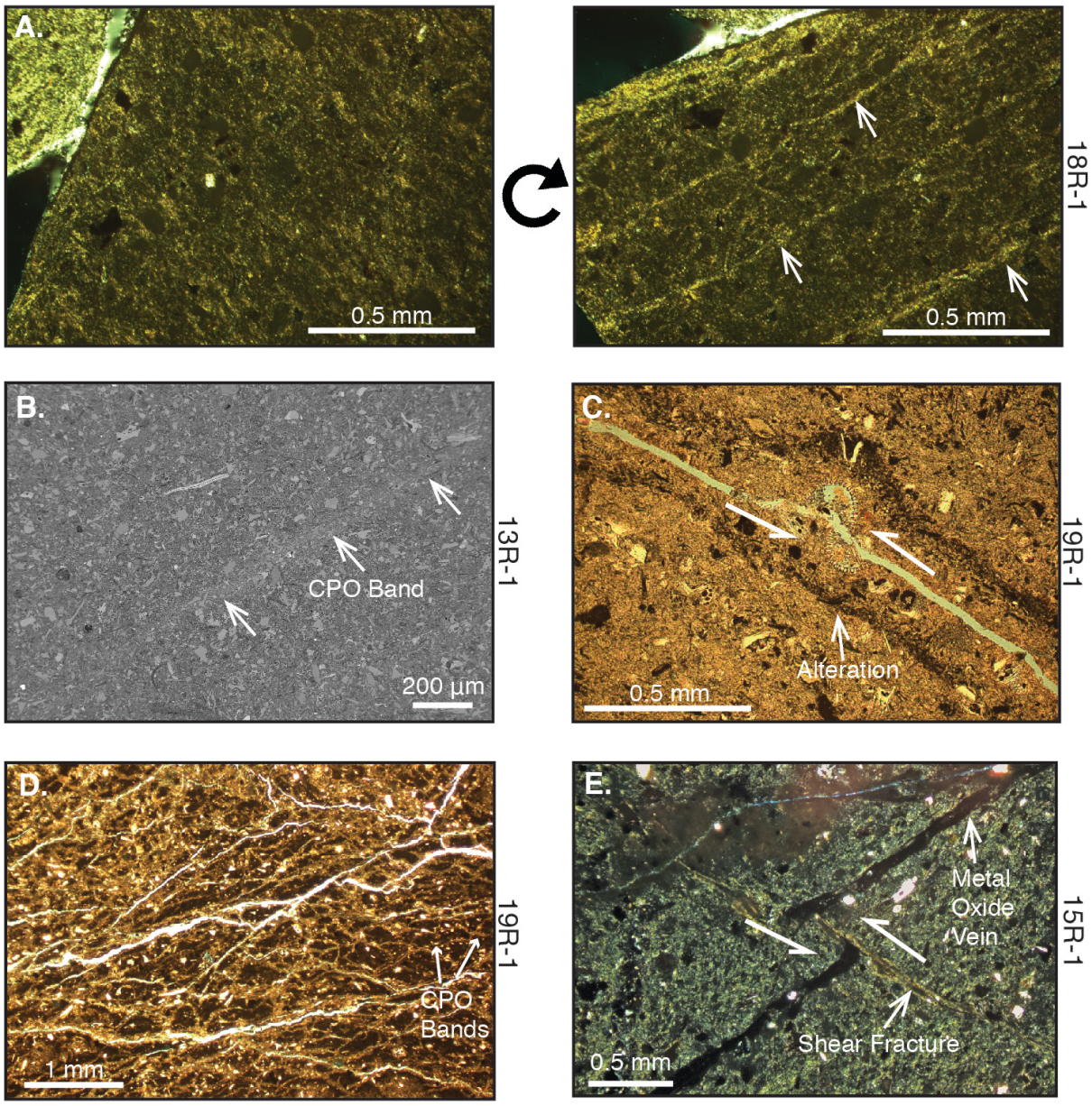

Figure 7: Types of microstructures included in scanline sampling. A) Crystallographic preferred orientation (CPO) bands, denoted by arrows, and only visible by rotating stage; B) BSE photo of CPO band with slightly brighter color compared to host; C) Shear fracture with associated alteration, offsetting microfossil; D) Shear zone of densely-arranged fractures and CPO bands; and E) Mineralized iron oxide vein, offset by shear fracture.

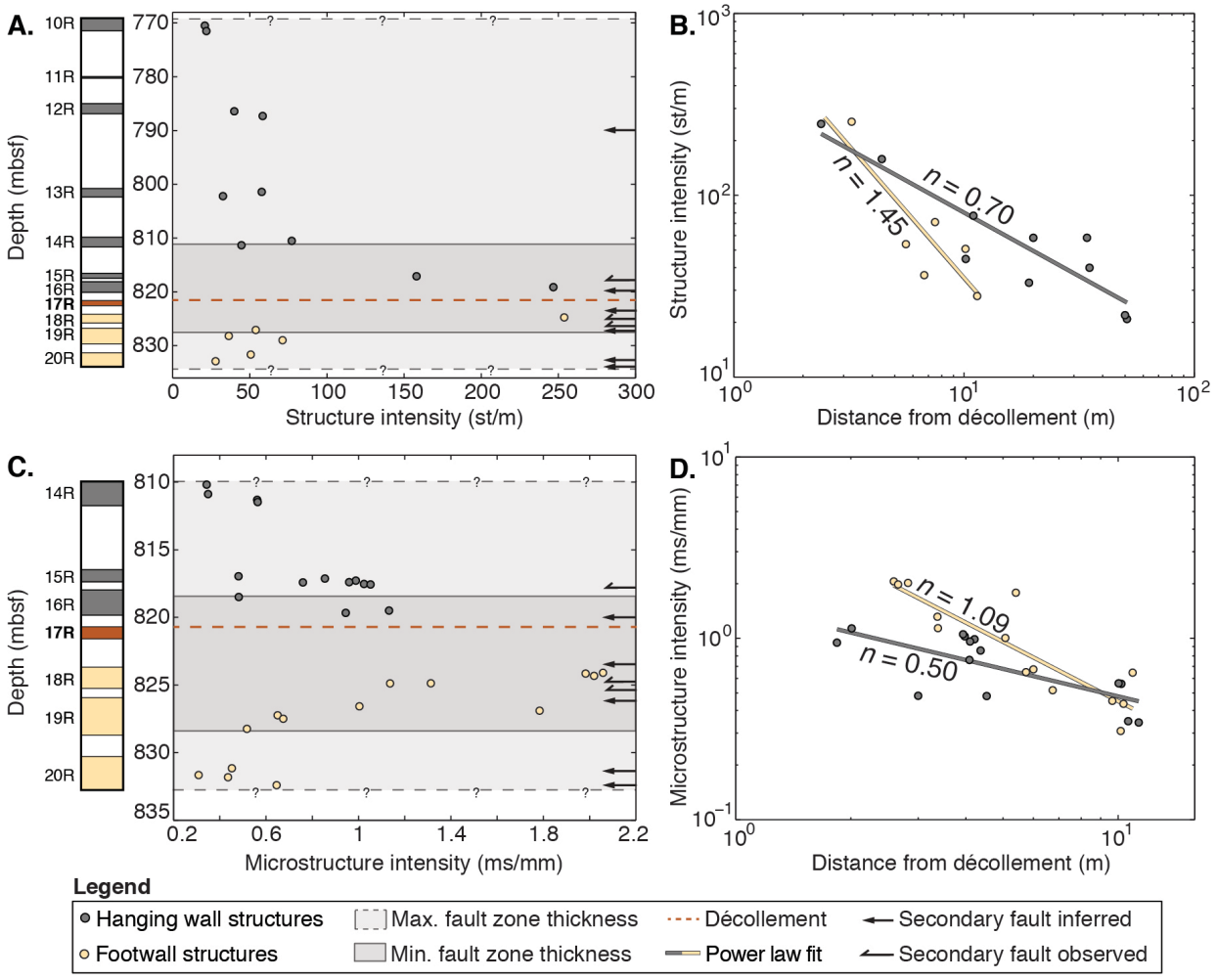

Figure 8: A) Spatial variability of core-scale structure intensity in all examined cores. Each point represents one core section. Arrows denote locations of secondary faults. Estimates of minimum and maximum damage zone thickness in gray scale shading. B) Change in core-scale structure intensity with distance from décollement on a logarithmic scale. Hanging wall and footwall data separately fit by power law functions, of which the value *n* describes the rate of damage decay. C) Spatial variability of microstructure intensity in only cores 14R-20R. Each point represents the average median microstructure intensity observed in three orthogonal thin sections. Estimates of minimum and maximum damage zone thickness in gray scale shading. D) Change in microstructure intensity with distance from décollement on a logarithmic scale with power law function fits to hanging wall and footwall data.

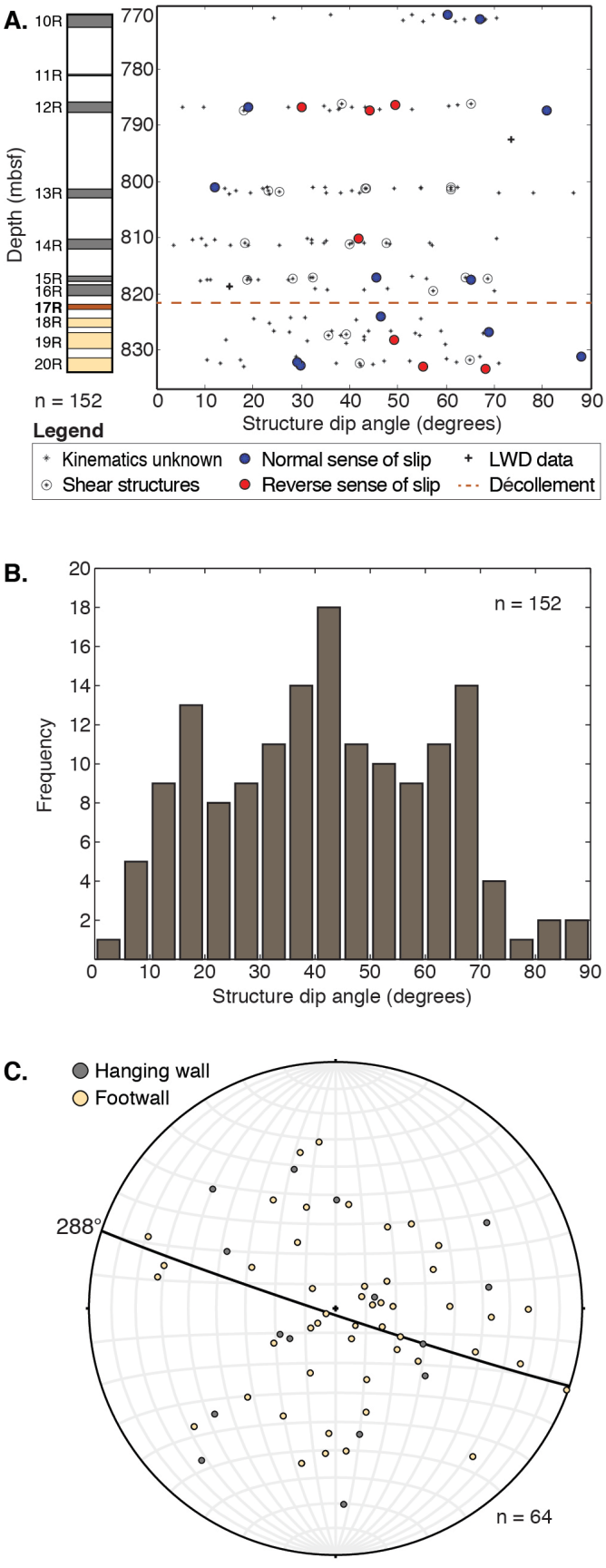

Figure 9: Core-scale orientation data. A) Variability in true dip angle with depth in all examined cores, displaying full range of structure orientations. Logging while drilling fracture/fault dip data included (n = 2) [*Chester et al.*, 2013a]. Structures for which kinematic criteria are available show no preferred shear structure orientations, low angle normal shear structures, and high angle reverse shear structures. B) Histogram of all core-scale structure dip angles. C) Lower hemisphere, equal-area projection of poles to planes of paleomagnetic corrected [*Mishima et al.*, 2012; *Chester et al.*, 2013a] orientations from coherent intervals of core, with best-fit great circle.

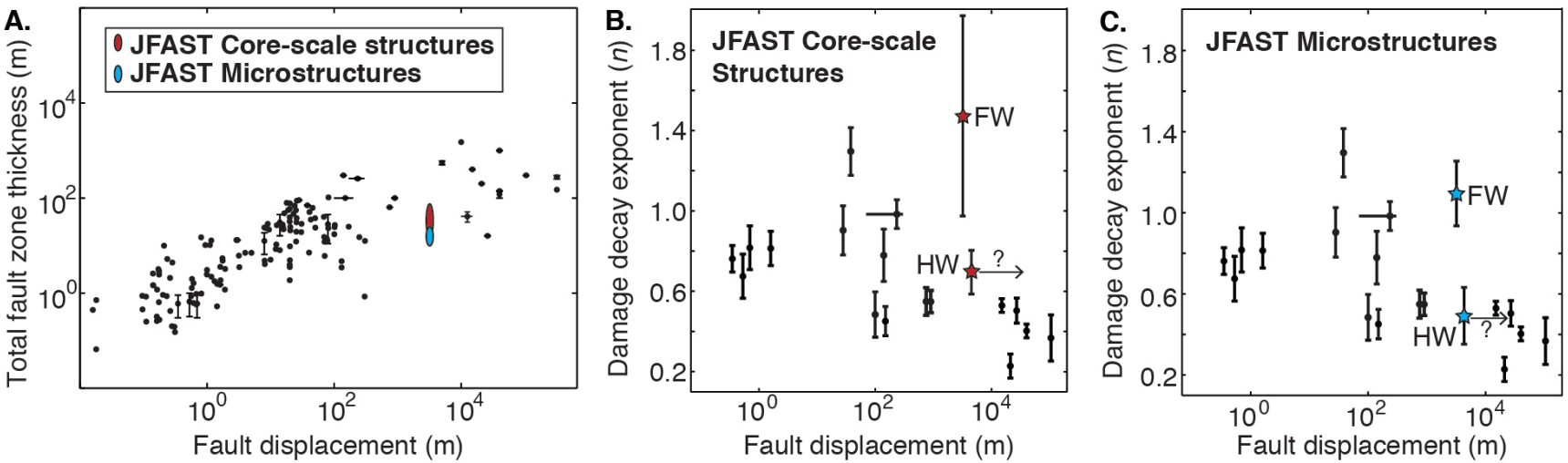

Figure 10: Comparison of JFAST damage zone characteristics with similar displacement faults of all lithologies and tectonic settings [modified from *Savage and Brodsky*, 2011]. A) Core- (red) and micro-scale (blue) estimations of damage zone thickness, comparatively narrow for similar offset faults. B) Damage decay exponents (*n*) and error bars for core-scale observations in hanging wall (HW) and footwall (FW). Footwall displacement is constrained at ~3.2 km [*Chester et al.*, 2013b]. C) Damage decay exponents and error bars for micro-scale observations. Hanging wall displacement is unknown, but likely slightly greater than 3.2 km.

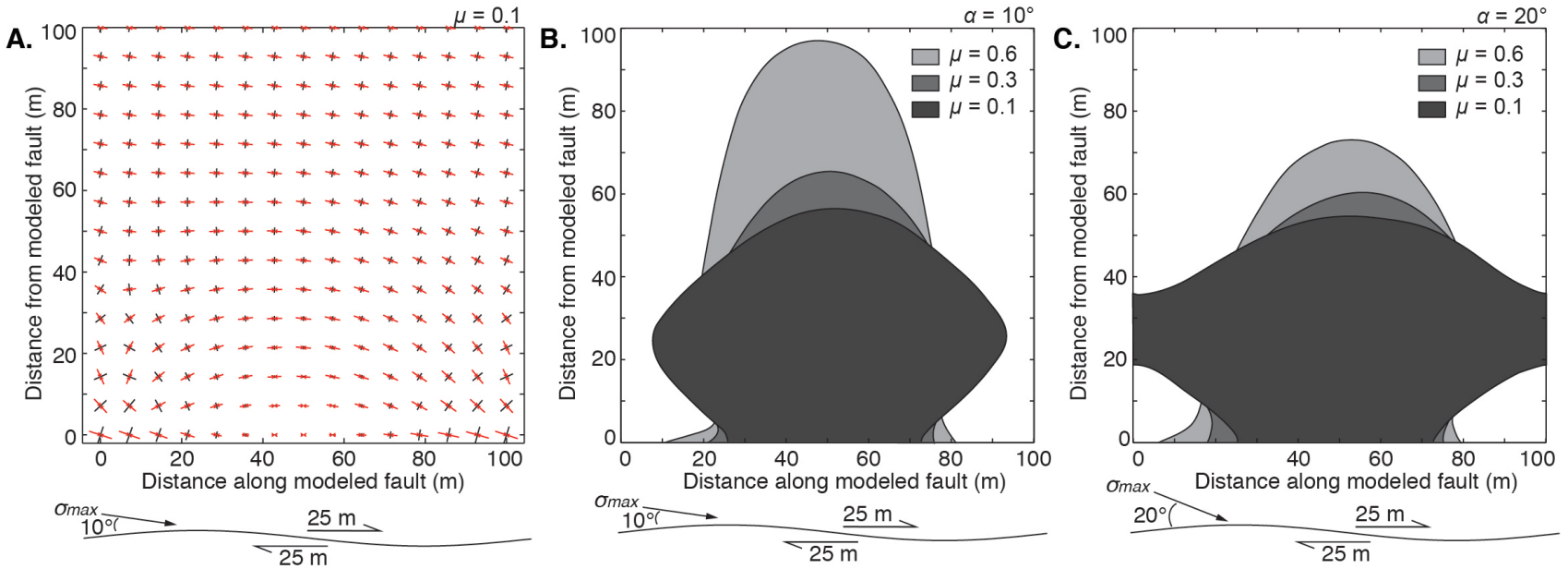

Figure 11: Quasi-static analytical modeling of wavy, frictional fault similar to the shallow Japan Trench décollement following *Chester and Chester* [2000]. A) Model stress field within 100 m of fault with coefficient of friction (μ) = 0.1. Red and black arrows represent orientation and relative magnitude of maximum (σ_1) and minimum (σ_3) principal compressive stresses, respectively. Far-field maximum principal compressive stress (σ_{max}) is at 10° to fault. Total relative displacement is 50 m in all three figures. B) Regions where failure criterion is satisfied for model stress distribution with varying μ. σ_{max} is at 10° to fault (see text for details of failure criterion). C) Regions where failure criterion is satisfied, with σ_{max} increased to 20° to fault.

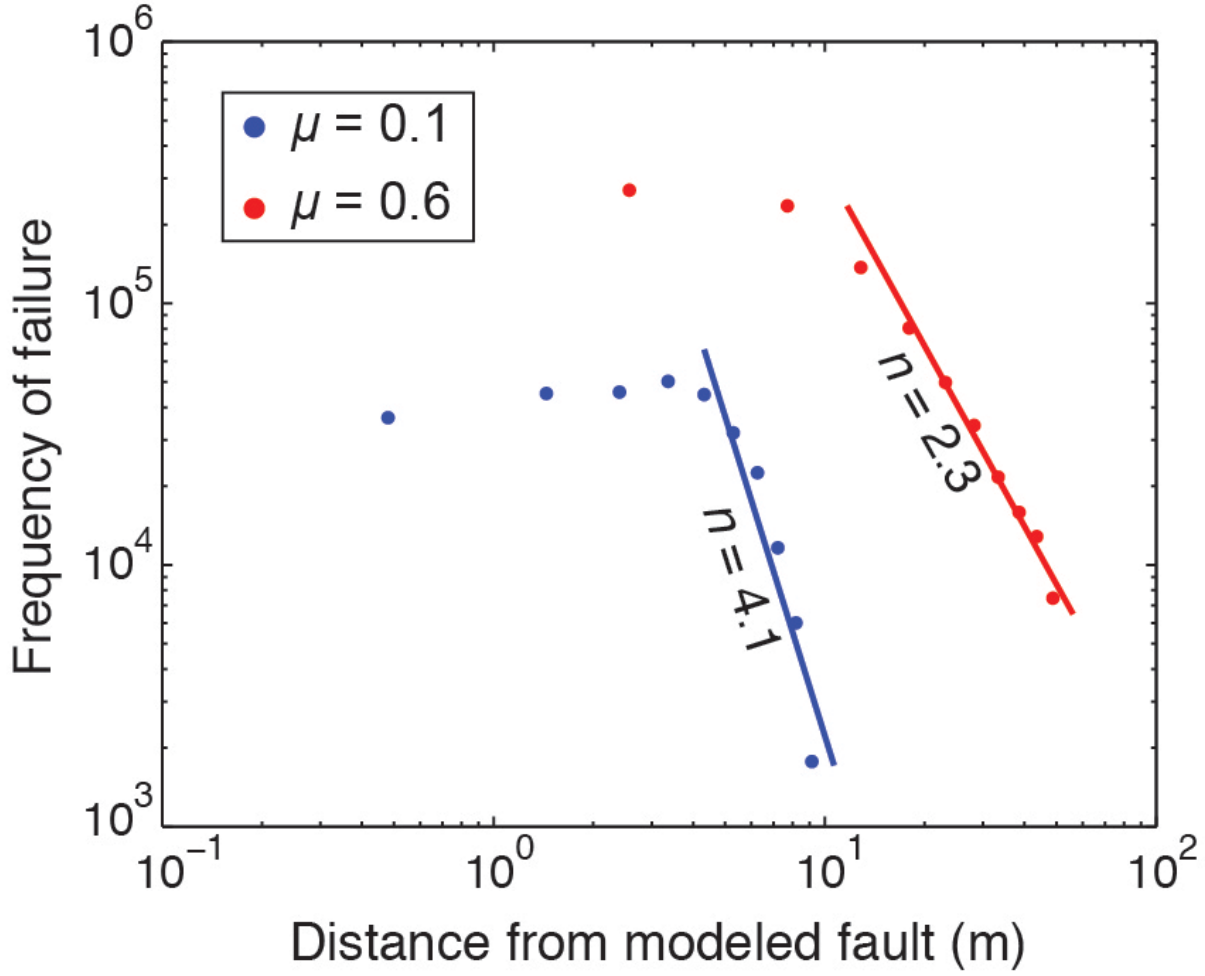

Figure 12: Change in frequency of failure with distance from modeled fault on logarithmic scale when summing the contributions of multiple wavelengths. Power law functions fit to straight portions of data indicate the decay in damage on low friction faults (blue) is steeper than high friction faults (red). Model parameters (with the exception of wavelength *L*) are the same as Fig. 11b.

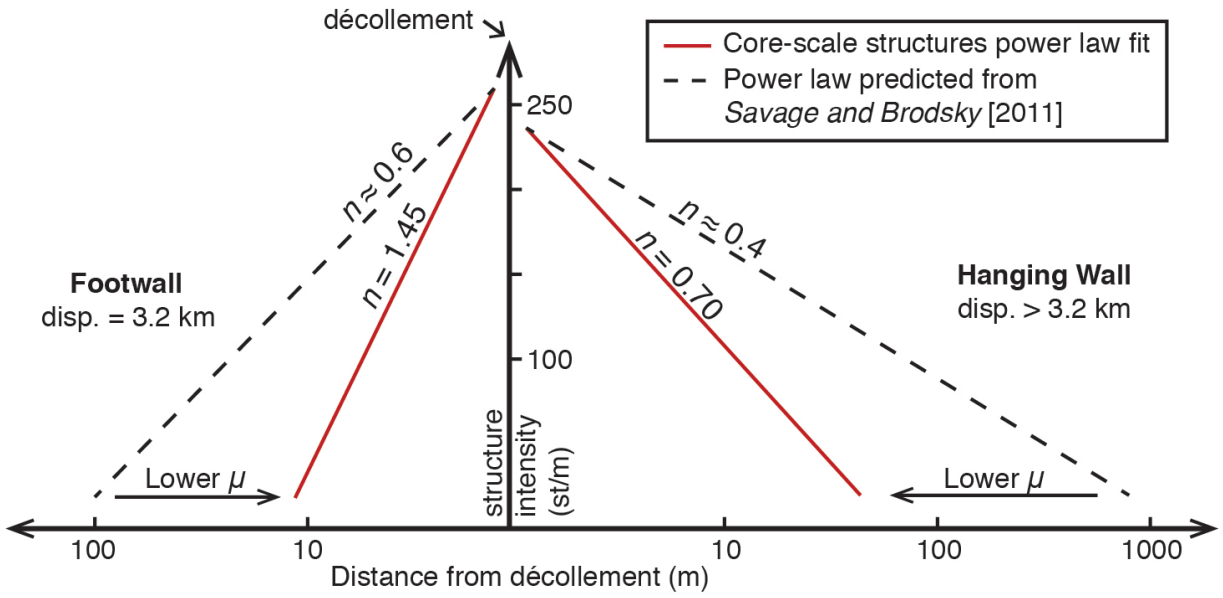

Figure 13: Schematic representation of change in damage zone thickness and decay exponents with decreasing fault friction (visualized with core-scale data as an example). If damage zone thickness (intercepts with x-axis) is sensitive to fault friction, then damage decay exponents will be inherently steeper when peak structure intensity near fault is reached (peak structure intensity at JFAST is unknown). If peak structure intensity is dependent on lithology and reached as faults mature, relative fault friction can be assessed across faults of similar lithology and age solely from damage zone characteristics.

REFERENCES

Ampuero, J. P., Y. Ben-Zion, and V. Lyakhovsky (2008), Interaction Between Dynamic Rupture and Off-Fault Damage, *Seismological Research Letters, 79*(2), 295-296.

Anders, M. H., and D. V. Wiltschko (1994), Microfracturing, paleostress and the growth of faults, *Journal of Structural Geology, 16* (6), 795-815, doi:10.1016/0191-8141(94)90146-5.

Anders, M. H., J. R. Schneider, C. H. Scholz, and S. Losh (2013), Mode I microfracturing and fluid flow in damage zones: The key to distinguishing faults from slides, *Journal of Structural Geology, 48*, 113-125, doi:10.1016/j.jsg.2012.11.010.

Apel, E. V., R. Bürgmann, G. Steblov, N. Vasilenko, R. King, and A. Prytkov (2006), Independent active microplate tectonics of northeast Asia from GPS velocities and block modeling, *Geophysical Research Letters, 33*, L11303, doi:10.1029/2006GL026077.

Argus, D. F., R. G. Gordon, and C. DeMets (2011), Geologically current motion of 56 plates relative to the no-net-rotation reference frame, *Geochemistry Geophysics Geosystems, 12*, Q11001, doi:10.1029/2011GC003751.

Arthur, M. A., B. Carson, and R. von Huene (1980), Initial tectonic deformation of hemipelagic sediment at the leading edge of the Japan convergent margin, in: Lee, M, and L. N. Stout (eds.), *Initial Reports of the Deep Sea Drilling Project 56-57 Part 1*, College Station, TX, 569-613.

Beeler, N. M., T. E. Tullis, M. L. Blanpied, and J. D. Weeks (1996), Frictional behavior of large displacement experimental faults, *Journal of Geophysical Research, 101*(B4), 8697–8715, doi:10.1029/96JB00411.

Berg, S. S., and T. Skar (2005), Controls on damage zone asymmetry of a normal fault zone: outcrop analyses of a segment of the Moab fault, SE Utah, *Journal of Structural Geology, 27*(10), 1803-1822, doi:10.1016/j.jsg.2005.04.012.

Bjørk, T. E., K. Mair, and H. Austrheim (2009), Quantifying granular material and deformation: Advantages of combining grain size, shape, and mineral phase recognition analysis, *Journal of Structural Geology, 31*(7), 637-653, doi:10.1016/j.jsg.2009.03.020.

Brock, W. G., and T. Engelder (1977), Deformation associated with the movement of the Muddy Mountain overthrust in the Buffington window, southeastern Nevada, *Geological Society of America Bulletin, 88*(11), 1667-1677.

Byerlee, J. D. (1978), Friction of rocks, *Pure and Applied Geophysics, 116*, 615–629.

Byrne, T., A. Maltman, E. Stephenson, W. Soh, and R. Knipe (1993), Deformation structures and fluid flow in the toe region of the Nankai accretionary prism, in: Hill, I. A., A. Taira, J. V. Firth, and P. J. Vrolijk (eds.), *Proceedings of the Ocean Drilling Program, Scientific Results 131*, College Station, TX, 83-101.

Caine, J. S., and S. A. Minor (2009), Structural and geochemical characteristics of faulted sediments and inferences on the role of water in deformation, Rio Grande Rift, New Mexico, *Geological Society of America Bulletin, 121*(9-10), 1325-1340.

Caine, J. S., J. P. Evans, and C. B. Forster (1996), Fault zone architecture and permeability structure, *Geology, 24*(11), 1025-1028.

Carson, B., R. von Huene, and M. Arthur (1982), Small-scale deformation structures and physical properties related to convergence in Japan Trench slope sediments, *Tectonics, 1*(3), 277–302, doi:10.1029/tc001i003p00277.

Chester, F. M., and J. S. Chester (2000), Stress and deformation along wavy frictional faults, *Journal of Geophysical Research, 105*(B10), 23421-23430, doi:10.1029/2000jb900241.

Chester, J. S., and R. C. Fletcher (1997), Stress distribution and failure in anisotropic rock near a bend on a weak fault, *Journal of Geophysical Research, 102*(B1), 693-708, doi:10.1029/96jb02791.

Chester, F. M., J. Mori, N. Eguchi, S. Toczko, and the Expedition 343/343T Scientists (2013a), Proceedings of the Integrated Ocean Drilling Program; Japan Trench Fast Drilling Project (JFAST), *IODP Management International*, College Station, TX, doi:10.2204/iodp.proc.343343T.2013.

Chester, F. M., C. Rowe, K. Ujiie, J. Kirkpatrick, C. Regalla, F. Remitti, … S. Toczko, (2013b), Structure and composition of the plate-boundary slip-zone for the 2011 Tohoku-oki earthquake, *Science, 342*, 1208-1211, doi:10.1126/science.1243719.

Childs, C., T. Manzocchi, J. J. Walsh, C. G. Bonson, A. N. Nicol, and M. P. J. Schopfer (2009), A geometric model of fault zone and fault rock thickness variations, *Journal of Structural Geology, 31*, 117–127, doi:10.1016/j.jsg.2008.08.009.

Cooke, M. L. (1997), Fracture localization along faults with spatially varying friction, *Journal of Geophysical Research, 102*(B10), 22425–22434, doi:10.1029/97JB01829.

Cooke, M. L., and D. D. Pollard (1997), Bedding-plane slip in initial stages of fault-related folding, *Journal of Structural Geology, 19*(3), 567-581, doi:10.1016/s0191-8141(96)00097-1.

Cowan, D. S. (1974), Deformation and metamorphism of the Franciscan subduction zone complex northwest of Pacheco Pass, California, *Geological Society of America Bulletin, 85*, 1623-1634.

Cowie, P. A., and C. H. Scholz (1992), Physical explanation for the displacement-length relationship of faults using a post-yield fracture mechanics model, *Journal of Structural Geology, 14*(10), 1133-1148, doi:10.1016/0191-8141(92)90065-5.

Cubas, N., N. Lapusta, J. P. Avouac, and H. Perfettini (2015), Numerical modeling of long-term earthquake sequences on the NE Japan megathrust: comparison with observations and implications for fault friction, *Earth and Planetary Science Letters, 419*, 187-198.

Davatzes, N. C., A. Aydin, and P. Eichhubl (2003), Overprinting faulting mechanisms during the development of multiple fault sets in sandstone, Chimney Rock fault array, Utah, USA, *Tectonophysics, 363*(1), 1-18, doi:10.1016/s0040-1951(02)00647-9.

Davy, P., C. Darcel, O. Bour, R. Munier, J. R. De Dreuzy (2006), A note on the angular correction applied to fracture intensity profiles along drill core, *Journal of Geophysical Research, 111*, B11408, doi:10.1029/2005JB004121.

DeMets, C., R. G. Gordon, and D. F. Argus (2010), Geologically current plate motions, *Geophysical Journal International, 181*, 1-80, doi:10.1111/j.1365-246x.2009.04491.x.

Dieterich, J. H., and D. E. Smith (2009), Nonplanar faults: Mechanics of slip and off-fault damage, *Pure and Applied Geophysics, 166*(10–11), 1799–1815, doi:10.1007/s00024-009-0517y.

Dor, O., T. K. Rockwell, and Y. Ben-Zion (2006), Geological observations of damage asymmetry in the structure of the San Jacinto, San Andreas and Punchbowl faults in Southern California: a possible indicator for preferred rupture propagation direction, *Pure and Applied Geophysics, 163*(2-3), 301-349, doi:10.1007/s00024-005-0023-9.

Duan, B. (2012), Dynamic rupture of the 2011 Mw 9.0 Tohoku-Oki earthquake: Roles of a possible subducting seamount, *Journal of Geophysical Research, 117*, B05311, doi:10.1029/2011JB009124.

Evans, J. P. (1990), Thickness-displacement relationships for fault zones, *Journal of Structural Geology, 12*(8), 1061-1065.

Faulkner, D. R., T. M. Mitchell, D. Healy, and M. J. Heap (2006), Slip on 'weak' faults by the rotation of regional stress in the fracture damage zone, *Nature, 444*(7121), 922-925, doi:10.1038/nature05353.

Faulkner, D. R., T. M. Mitchell, E. Jensen, and J. Cembrano (2011a), Scaling of fault damage zones with displacement and the implications for fault growth processes, *Journal of Geophysical Research, 116*, B05403, doi:10.1029/2010JB007788.

Faulkner, D. R., T. M. Mitchell, J. Behnsen, T. Hirose, and T. Shimamoto (2011b), Stuck in the mud? Earthquake nucleation and propagation through accretionary forearcs, *Geophysical Research Letters, 38*, L18303, doi:10.1029/2011GL048552.

Ferri, F., G. Di Toro, T. Hirose, R. Han, H. Noda, T. Shimamoto, M. Quaresimin, and N. de Rossi (2011), Low- to high-velocity frictional properties of the clay-rich gouges from the slipping zone of the 1963 Vaiont slide, northern Italy, *Journal of Geophysical Research, 116*, B09208, doi:10.1029/2011JB008338.

Fossen, H., and J. Hesthammer (2000), Possible absence of small faults in the Gullfaks Field, northern North Sea: Implications for downscaling of faults in some porous sandstones, *Journal of Structural Geology*, *22*(7), 851–863, doi:10.1016/S0191-8141(00)00013-4.

Fossen, H., R. A. Schultz, Z. K. Shipton, and K. Mair (2007), Deformation bands in sandstone: a review, *Journal of the Geological Society, London, 164*(4), 755-769, doi:10.1144/0016-76492006-036.

Friedman, M. (1969), Structural analysis of fractures in cores from the Saticoy Field, Ventura Co., California, *AAPG Bulletin, 53*, 367–389.

French, M. E., H. Kitajima, J. S. Chester, F. M. Chester, and T. Hirose (2014), Displacement and dynamic weakening processes in smectite-rich gouge from the Central Deforming Zone of the San Andreas Fault, *Journal of Geophysical Research, 119*, 1777–1802, doi:10.1002/2013JB010757.

Fulton, P. M., E. E. Brodsky, Y. Kano, J. Mori, F. Chester, T. Ishikawa, R. N. Harris, W. Lin, N. Eguchi, and S. Toczko (2013), Low coseismic friction on the Tohoku-Oki fault determined from temperature measurements, *Science, 342*(6163), 1214-1217, doi:10.1126/science.1243641.

Fujii, Y., K. Satake, S. Sakai, M. Shinohara, and T. Kanazawa (2011), Tsunami source of the 2011 off the Pacific coast of Tohoku earthquake, *Earth Planets Space*, 63, 815–820, doi:10.5047/eps.2011.06.010.

Griffith, W. A., S. Nielsen, G. Di Toro, and S. A. Smith (2010), Rough faults, distributed weakening, and off-fault deformation, *Journal of Geophysical Research, 115*, B08409, doi:10.1029/2009JB006925.

Hafner, W. (1951), Stress distributions and faulting, *Geological Society of America Bulletin*, *62*(4), 373-398.

Hasegawa, A., K. Yoshida, Y. Asano, T. Okada, T. Iinuma, and Y. Ito (2012), Change in stress field after the 2011 great Tohoku-Oki earthquake, *Earth and Planetary Science Letters*, *355-356*, 231–243, doi:10.1016/j.epsl.2012.08.042.

Hashimoto, C., A. Noda, T. Sagiya, and M. Matsu'ura (2009), Interplate seismogenic zones along the Kuril-Japan trench inferred from GPS data inversion, *Nature Geoscience, 2*, 141-144, doi:10.1038/ngeo421.

Heermance, R., Z. K. Shipton, and J. P. Evans (2003), Fault structure control on fault slip and ground motion during the 1999 rupture of the Chelungpu fault, Taiwan, *Bulletin of the Seismological Society of America, 93*, 1034–1050, doi:10.1785/0120010230.

Heynekamp, M. R., Goodwin, L. B., Mozley, P. S. and Haneberg, W. C. (1999) Controls on Fault-Zone Architecture in Poorly Lithified Sediments, Rio Grande Rift, New Mexico: Implications for Fault-Zone Permeability and Fluid Flow, in: Haneberg, W. C., P. S. Mozley, J. C. Moore and L. B. Goodwin (eds.), *Faults and Subsurface Fluid Flow in the Shallow Crust*, American Geophysical Union, Washington, D. C., doi:10.1029/GM113p0027.

Huang, Y., L. Meng, and J. P. Ampuero (2012), A dynamic model of the frequency-dependent rupture process of the 2011 Tohoku-Oki earthquake, *Earth Planets Space*, *64*(12), 1061-1066, doi:10.5047/eps.2012.05.011.

Hull, J. (1988), Thickness-displacement relationships for deformation zones, *Journal of Structural Geology*, *10*(4), 431-435.

Ide, S., A. Baltay, and G. C. Beroza (2011), Shallow dynamic overshoot and energetic deep rupture in the 2011 Mw 9.0 Tohoku-Oki earthquake, *Science*, *332*(6036), 1426-1429, doi:10.1126/science.1207020.

Ikari, M. J., J. Kameda, D. M. Saffer, and A. J. Kopf (2015), Strength characteristics of Japan Trench borehole samples in the high-slip region of the 2011 Tohoku-Oki earthquake, *Earth and Planetary Science Letters*, *412*, 35-41, doi:10.1016/j.epsl.2014.12.014.

Ito, Y., T. Tsuji, Y. Osada, M. Kido, D. Inazu, Y. Hayashi, H. Tsushima, R. Hino, and H. Fujimoto (2011), Frontal wedge deformation near the source region of the 2011 Tohoku-oki earthquake, *Geophysical Research Letters*, *38*, L00G05, doi:10.1029/2011GL048355.

Jaeger, J. C., N. G. Cook, and R. Zimmerman, R. (2007), *Fundamentals of Rock Mechanics* (4th ed.), Wiley-Blackwell, Hoboken, NJ, 488 pp.

Johnson, A. M., and R. C. Fletcher (1994), *Folding of Viscous Layers*, Columbia University Press, New York, NY, 461 pp.

Johri, M., E. M. Dunham, M. D. Zoback, and Z. Fang (2014a), Predicting fault damage zones by modeling dynamic rupture propagation and comparison with field observations, *Journal of Geophysical Research, 119*(2), 1251-1272, doi:10.1002/2013JB010335.

Johri, M., M. D. Zoback, and P. Hennings (2014b), A scaling law to characterize fault-damage zones at reservoir depths, *AAPG Bulletin*, *98*(10), 2057-2079, doi:10.1306/05061413173.

Kameda, J., M. Shimizu, K. Ujiie, T. Hirose, M. Ikari, J. Mori, K. Oohashi, and G. Kimura (2015), Pelagic smectite as an important factor in tsunamigenic slip along the Japan Trench, *Geology*, *43*(2), 155-158, doi:10.1130/g35948.1.

Kanamori, H., M. Miyazawa, and J. Mori (2006), Investigation of the earthquake sequence off Miyagi prefecture with historical seismograms, *Earth Planets Space, 58*, 1533-1541, doi:10.1186/bf03352657.

Kato, N., and S. Yoshida (2011), A shallow strong patch model for the 2011 great Tohoku-oki earthquake: A numerical simulation, *Geophysical Research Letters, 38*, L00G04, doi:10.1029/2011GL048565.

Kennedy, L. A., and J. C. White (2001), Low-temperature recrystallization in calcite: Mechanisms and consequences, *Geology*, *29*(11), 1027-1030.

Kennett, B. L. N., A. Gorbatov, and E. Kiser (2011), Structural controls on the Mw 9.0 2011 Offshore-Tohoku earthquake, *Earth and Planetary Science Letters*, *310*(3), 462-467, doi:10.1016/j.epsl.2011.08.039.

Keren, T. T., and J. D. Kirkpatrick (2015), Tectonic and induced structures in the JFAST core, *Proceedings of the IODP 343/343T*, Integrated Ocean Drilling Program Management International, Inc., College Station, TX, in review.

Kilsdonk, B., and R. C. Fletcher (1989), An analytical model of hanging-wall and footwall deformation at ramps on normal and thrust faults, *Tectonophysics*, *163*(1), 153-168, doi:10.1016/0040-1951(89)90123-6.

Kirkpatrick, J. D., C. D. Rowe, K. Ujiie, J. C. Moore, C. A. Regalla, F. Remitti, V. Toy, M. Wolfson-Schwehr, J. Kameda, S. Bose, and F. M. Chester (2015), Structure and lithology of the Japan Trench subduction plate boundary fault, *Tectonics, 34*, 53–69, doi:10.1002/2014TC003695.

Knott, S. D., A. Beach, P. J. Brockbank, J. L. Brown, J. E. McCallum, and A. I. Welbon (1996), Spatial and mechanical controls on normal fault populations, *Journal of Structural Geology, 18*(2–3), 359–372, doi:10.1016/S01918141(96)80056-3.

Kodaira, S., T. No, Y. Nakamura, T. Fujiwara, Y. Kaiho, S. Miura, N. Takahashi, Y. Kaneda, and A. Taira (2012), Coseismic fault rupture at the trench axis during the 2011 Tohoku-oki earthquake, *Nature Geoscience, 5*, 646–650, doi:10.1038/ngeo1547.

Koge, H., T. Fujiwara, S. Kodaira, T. Sasaki, J. Kameda, Y. Kitamura, ... and G. Kimura (2014), Friction properties of the plate boundary megathrust beneath the frontal wedge near the Japan Trench: an inference from topographic variation, *Earth, Planets and Space*, *66*(1), 153, doi:10.1186/s40623-014-0153-3.

Kozdon, J. E., and E. M. Dunham (2013), Rupture to the trench: Dynamic rupture simulations of the 11 March 2011 Tohoku earthquake, *Bulletin of the Seismological Society of America, 103*(2B), 1275-1289, doi:10.1785/0120120136.

Lay, T., C. J. Ammon, H. Kanamori, M. J. Kim, and L. Xue (2011), Outer trench-slope faulting and the 2011 Mw 9.0 off the Pacific coast of Tohoku Earthquake, *Earth Planets Space*, *63*(7), 713-718, doi:10.5047/eps.2011.05.006.

Lewis, J. C., T. Byrne, and D. J. Prior (1997), Small faults and kink bands in the Nankai accretionary complex: Textural observations from Site 808 of ODP Leg 131, *The Island Arc*, *6*(2), 183-196, doi:10.1111/j.1440-1738.1997.tb00169.x.

Lin, W., S. Saito, Y. Sanada, Y. Yamamoto, Y. Hashimoto, and T. Kanamatsu (2011), Principal horizontal stress orientations prior to the 2011 M w 9.0 Tohoku-Oki, Japan, earthquake in its source area, *Geophysical Research Letters*, *38*(7), L00G10, doi:10.1029/2011gl049097.

Lin, W., M. Conin, J. C. Moore, F. M. Chester, Y. Nakamura, J. J. Mori, ... N. Eguchi (2013). Stress state in the largest displacement area of the 2011 Tohoku-oki earthquake. *Science*, *339*(6120), 687-690, doi:10.1126/science.1229379.

Lindsley-Griffin, N., A. Kemp, and J. F. Swartz (1990), Vein structures of the Peru margin, Leg 112, in: Suess, E., R. von Huene, *et al.* (eds.*), Proceedings of the Ocean Drilling Program, Scientific Results 112,* 3–16.

Love, A. E. H. (1927), *A Treatise on the Mathematical Theory of Elasticity*, Dover, New York.

Loveless, J. P., and B. J. Meade (2011), Spatial correlation of interseismic coupling and coseismic rupture extent of the 2011 M_W = 9.0 Tohoku-oki earthquake, *Geophysical Research Letters, 38*, L17306, doi:10.1029/2011GL048561.

Lundberg, N., and D. E. Karig (1986), Structural features in cores from the Nankai Trough, Deep Sea Drilling Project Leg 87A, in: Kagami, H., D. E. Karig, W. T. Coulbourn, W. T., *et al.* (eds.), *Initial Reports of the Deep Sea Drilling Project 87*, College Station, TX, 797-808, doi:10.2973/dsdp.proc.87.126.1986.

Lundberg, N., and J. C. Moore (1986), Macroscopic structural features in Deep Sea Drilling Project cores from forearc regions, *Geological Society of America Memoirs*, *166*, 13-44.

Lyakhovsky, V. (2001), Scaling of fracture length and distributed damage, *Geophysical Journal International*, *144*(1), 114-122, doi:10.1046/j.0956-540x.2000.01303.x.

Lyakhovsky, V., Y. Ben-Zion, and A. Agnon (1997), Distributed damage, faulting, and friction, *Journal of Geophysical Research*, *102*(B12), 27635–27649, doi:10.1029/97JB01896.

Matsubara, M., and K. Obara (2011), The 2011 off the Pacific coast of Tohoku Earthquake related to a strong velocity gradient with the Pacific plate, *Earth Planets Space*, *63*(7), 663-667, doi:10.5047/eps.2011.05.018.

Maltman, A. J. (1998), Deformation structures from the toes of active accretionary prisms, *Journal of the Geological Society, London*, *155*(4), 639-650.

Maltman, A. J., T. Byrne, D. E. Karig, and S. Lallemant (1993), Deformation at the toe of an active accretionary prism: synopsis of results from ODP Leg 131, Nankai, SW Japan, *Journal of Structural Geology, 15*(8), 949-964, doi:10.1016/0191-8141(93)90169-b.

Mauldon, M., and J. G. Mauldon (1997), Fracture sampling on a cylinder: from scanlines to boreholes and tunnels, *Rock Mechanics and Rock Engineering, 30*(3), 129-144, doi:10.1007/bf01047389.

McGrath, A. G., and I. Davison (1995), Damage zone geometry around fault tips, *Journal of Structural Geology, 17*(7), 1011-1024, doi:10.1016/0191-8141(94)00116-h.

Minoura, K., F. Imamura, D. Sugawara, Y. Kono, and T. Iwashita (2001), The 869 Jōgan tsunami deposit and recurrence interval of large-scale tsunami on the Pacific coast of northeast Japan, *Journal of Natural Disaster Science, 23*(2), 83-88.

Mishima, T., T. Yang, J. J. Mori, F. M. Chester, N Eguchi, and S. Toczko (2012), Preliminary rock-magnetic studies of core samples from the IODP Japan Trench Fast Drilling Project (JFAST), paper presented at 2012 American Geophysical Union Fall Meeting, San Francisco, CA, Abstract T13B-2608.

Mitchell, T. M., and D. R. Faulkner (2009), The nature and origin of off-fault damage surrounding strike-slip fault zones with a wide range of displacements: A field study from the Atacama fault system, northern Chile, *Journal of Structural Geology, 31*(8), 802–816, doi:10.1016/j. jsg.2009.05.002.

Mitsui, Y., N. Kato, Y. Fukahata, and K. Hirahara (2012), Megaquake cycle at the Tohoku subduction zone with thermal fluid pressurization near the surface, *Earth and Planetary Science Letters, 325*, 21-26, doi:10.1016/j.epsl.2012.01.026.

Miura, S., N. Takahashi, A. Nakanishi, T. Tsuru, S. Kodaira, and Y. Kaneda (2005), Structural characteristics off Miyagi forearc region, the Japan Trench seismogenic zone, deduced from a wide-angle reflection and refraction study, *Tectonophysics, 407*(3-4), 165–188, doi:10.1016/j.tecto.2005.08.001.

Nakamura, Y., S. Kodaira, B. J. Cook, T. Jeppson, T. Kasaya, Y. Yamamoto, Y. Hashimoto, M. Yamaguchi, K. Obana, and G. Fujie (2014), Seismic imaging and velocity structure around the JFAST drill site in the Japan Trench: low *V*p, high *V*p/*V*s in the transparent frontal prism, *Earth, Planets and Space, 66*(1), 121, doi:10.1186/1880-5981-66-121.

Nakamura, Y., S. Kodaira, S. Miura, C. Regalla, and N. Takahashi (2013), High resolution seismic imaging in the Japan Trench axis area off Miyagi, northeastern Japan, *Geophysical Research Letters, 40*, 1713-1718, doi:10.1002/grl.50364.

Noda, H., and N. Lapusta (2013), Stable creeping fault segments can become destructive as a result of dynamic weakening, *Nature, 493*(7433), 518-521, doi:10.1038/nature11703.

Oohashi, K., T. Hirose, M. Takahashi, and W. Tanikawa (2015), Dynamic weakening of smectite-bearing faults at intermediate velocities: Implications for subduction zone earthquakes, *Journal of Geophysical Research*, in press, doi:10.1002/2015JB011881.

Peacock, D. C. P. (2006), Predicting variability in joint frequencies from boreholes, *Journal of Structural Geology*, *28*(2), 353-361, doi:10.1016/j.jsg.2005.10.007.

Peacock, D. C. P., S. D. Harris, M. Mauldon (2003), Use of curved scanlines and boreholes to predict fracture frequencies, *Journal of Structural Geology*, *25*(1), 109-119, doi:10.1016/s0191-8141(02)00016-0.

Perfettini, H., and J. P. Avouac (2014), The seismic cycle in the area of the 2011 *Mw*9.0 Tohoku-Oki earthquake, *Journal of Geophysical Research, 119*, 4469–4515, doi:10.1002/2013JB010697.

Pollitz, F. F., R. Bürgmann, and P. Banerjee (2011), Geodetic slip model of the 2011 M9.0 Tohoku earthquake, *Geophysical Research Letters, 38*, L00G08, doi:10.1029/2011GL048632.

Power, W. L., and T. E. Tullis (1991), Euclidean and fractal models for the description of rock surface roughness, *Journal of Geophysical Research*, *96*(B1), 415-424, doi:10.1029/90JB02107.

Power, W. L., T. E. Tullis, S. R. Brown, G. N. Boitnott, and C. H. Scholz (1987), Roughness of natural fault surfaces, *Geophysical Research Letters*, *14*(1), 29-32, doi:10.1029/gl014i001p00029.

Rabinowitz, H. S., H. M. Savage, T. Plank, P. J. Polissar, J. D. Kirkpatrick, and C. D. Rowe (2015), Multiple major faults at the Japan Trench: Chemostratigraphy of the plate boundary at IODP Exp. 343: JFAST, *Earth and Planetary Science Letters*, in review.

Rice, J. R., C. G. Sammis, and R. Parsons (2005), Off-fault secondary failure induced by a dynamic slip pulse, *Bulletin of the Seismological Society of America*, *95*(1), 109-134, doi:10.1785/0120030166.

Ritz, E., and D. D. Pollard (2012), Stick, slip, and opening of wavy frictional faults: A numerical approach in two dimensions, *Journal of Geophysical Research, 117*, B03405, doi:10.1029/2011JB008624.

Ritz, E., D. D. Pollard, and M. Ferris (2015), The influence of fault geometry on small strike-slip fault mechanics, *Journal of Structural Geology*, *73*, 49-63, doi:10.1016/j.jsg.2014.12.007.

Rochford, E. L., D. J. Prior, S. M. Agar, and A. Maltman (1995), Microstructural analysis of deformation bands from site 860, Chile margin, in: Lewis, S. D., J. H. Behrmann, R. J. Musgrave, and S. C. Cande (eds.), *Proceedings of the Ocean Drilling Program, Scientific Results, 141*, College Station, TX, 13-26.

Saffer, D. M., and C. Marone (2003), Comparison of smectite-and illite-rich gouge frictional properties: application to the updip limit of the seismogenic zone along subduction megathrusts, *Earth and Planetary Science Letters, 215*(1), 219-235, doi:10.1016/s0012-821x(03)00424-2.

Sanford, A. R. (1959), Analytical and experimental study of simple geologic structures, *Geological Society of America Bulletin, 70*(1), 19-52.

Sagy, A., and E. E. Brodsky (2009), Geometric and rheological asperities in an exposed fault zone, *Journal of Geophysical Research, 114*, B02301, doi:10.1029/2008JB005701.

Sato, M., M. Fujita, Y. Matsumoto, T. Ishikawa, H. Saito, M. Mochizuki, and A. Asada (2013), Interplate coupling off northeastern Japan before the 2011 Tohoku-oki earthquake, inferred from seafloor geodetic data, *Journal of Geophysical Research, 118*, 3860–3869, doi:10.1002/jgrb.50275.

Saucier, F., E. Humphreys, and R. Weldon (1992), Stress near geometrically complex strike-slip faults: application to the San Andreas fault at Cajon Pass, Southern California, *Journal of Geophysical Research, 97*(B4), 5081-5094, doi:10.1029/91jb02644.

Savage, H. M., and E. E. Brodsky (2011), Collateral damage: Evolution with displacement of fracture distribution and secondary fault strands in fault damage zones, *Journal of Geophysical Research, 116*, B03405, doi:10.1029/2010JB007665.

Savage, H. M., and M. L. Cooke (2010), Unlocking the effects of friction on fault damage zones, *Journal of Structural Geology, 32*(11), 1732-1741, doi:10.1016/j.jsg.2009.08.014.

Sawai, M., T. Hirose, and J. Kameda (2014), Frictional properties of incoming pelagic sediments at the Japan Trench: implications for large slip at a shallow plate boundary during the 2011 Tohoku earthquake, *Earth, Planets and Space, 66*(1), 65, doi:10.1186/1880-5981-66-65.

Sawai, Y., Y. Namegaya, Y. Okamura, K. Satake, and M. Shishikura (2012), Challenges of anticipating the 2011 Tohoku earthquake and tsunami using coastal geology, *Geophysical Research Letters, 39*, L21309, doi:10.1029/2012GL053692.

Scholz, C. H. (1987), Wear and gouge formation in brittle faulting, *Geology, 15*(6), 493-495.

Scholz, C. H., N. H. Dawers, J. Z. Yu, M. H. Anders, and P. A. Cowie (1993), Fault growth and fault scaling laws: Preliminary results, *Journal of Geophysical Research, 98*(B12), 21951–21961, doi:10.1029/93JB01008.

Schulz, S. E., and J. P. Evans (1998), Spatial variability in microscopic deformation and composition of the Punchbowl fault, southern California: Implications for mechanisms, fluid–rock interaction, and fault morphology, *Tectonophysics, 295*(1), 223–244, doi:10.1016/s0040-1951(98)00122-x.

Scientific Party (1980), *Initial Reports of the Deep Sea Drilling Project*, vol. 56, 57, U.S. Gov't. Printing Office, doi:10.2973/dsdp.proc.5657.1980.

Shibazaki, B., T. Matsuzawa, A. Tsutsumi, K. Ujiie, A. Hasegawa, and Y. Ito (2011), 3D modeling of the cycle of a great Tohoku-oki earthquake, considering frictional behavior at low to high slip velocities, *Geophysical Research Letters, 38*, L21305, doi:10.1029/2011GL049308.

Shipton, Z. K., A. M. Soden, J. D. Kirkpatrick, A. M. Bright, and R. J. Lunn (2006), How thick is a fault? Fault-displacement-thickness scaling revisited, in: R. E. Abercrombie, *et al.* (eds.), *Earthquakes: Radiated Energy and the Physics of Faulting*, Geophys. Monogr. Ser., vol. 170, AGU, Washington, D. C., 193–198.

Shipton, Z. K., J. P. Evans, and L. B. Thompson (2005), The geometry and thickness of deformation-band fault core and its influence on sealing characteristics of deformation-band fault zones, in: Sorkabi, R. and Y. Tsuji (eds.) *Faults, Fluid Flow, and Petroleum Traps*, AAPG Memoirs, 85, 181–195.

Suyehiro, K., and A. Nishizawa (1994), Crustal structure and seismicity beneath the forearc off northeastern Japan, *Journal of Geophysical Research, 99*(B11), 22331-22347, doi:10.1029/94jb01337.

Terzaghi, R. D. (1965), Sources of error in joint surveys, *Geotechnique, 15*(3), 287-304.

Tsuji, T., Y. Ito, M. Kido, Y. Osada, and H. Fujimoto (2011), Potential tsunamigenic faults of the 2011 off the Pacific coast of Tohoku Earthquake, *Earth Planets Space, 63*(7), 831–834, doi:10.5047/eps.2011.05.028.

Tsuru, T., J. Park, N. Takahashi, S. Kodaira, Y. Kido, Y. Kaneda, and Y. Kono (2000), Tectonic features of the Japan Trench convergent margin off Sanriku, northeastern Japan revealed by multi-channel seismic reflection data, *Journal of Geophysical Research, 105*, 16403–16413, doi:10.1029/2000jb900132.

Tsuru, T., J. Park, S. Miura, S. Kodaira, Y. Kido, and T. Hayashi (2002), Along-arc structural variation of the plate boundary at the Japan Trench margin; implication of interplate coupling, *Journal Of Geophysical Research, 107*(B12), 2357, doi:10.1029/2001jb001664.

Tsutsumi, A., O. Fabbri, A. M. Karpoff, K. Ujiie, and A. Tsujimoto (2011), Friction velocity dependence of clay‐rich fault material along a megasplay fault in the Nankai subduction zone at intermediate to high velocities, *Geophysical Research Letters*, 38(L19301), doi:10.1029/2011GL049314.

Ujiie, K., A. J. Maltman, and M. Sánchez-Gómez (2004), Origin of deformation bands in argillaceous sediments at the toe of the Nankai accretionary prism, southwest Japan, *Journal of Structural Geology, 26*(2), 221–231, doi:10.1016/j.jsg.2003.06.001.

Ujiie, K., H. Tanaka, T. Saito, A. Tsutsumi, J. J. Mori, J. Kameda, … S. Toczko (2013), Low coseismic shear stress on the Tohoku-Oki megathrust determined from laboratory experiments, *Science, 342,* 1211-1214, doi:10.1126/science.1243485.

Vannucchi, P., and H. Tobin (2000), Deformation structures and implications for fluid flow at the Costa Rica convergent margin, ODP Sites 1040 and 1043, Leg 170, *Journal of Structural Geology, 22*(8), 1087-1103, doi:10.1016/s0191-8141(00)00027-4.

Vermilye, J. M., and C. H. Scholz (1998), The process zone: A microstructural view of fault growth, *Journal of Geophysical Research, 103*(B6), 12223–12237, doi:10.1029/98JB00957.

von Huene, R., and R. C. Culotta (1989), Tectonic erosion at the front of the Japan Trench convergent margin, *Tectonophysics, 160*(1–4), 75–90, doi:10.1016/0040-1951(89)90385-5.

von Huene, R., and S. Lallemand (1990), Tectonic erosion along the Japan and Peru convergent margins, *Geological Society of America Bulletin, 102*(6), 704–720, doi:10.1130/00167606(1990)102<0704:TEATJA>2.3.CO;2.

von Huene, R., C. R. Ranero, and P. Vannucchi (2004), Generic model of subduction erosion, *Geology, 32*, 913–916, doi:10.1130/G20563.1.

von Huene, R., D. Klaeschen, B. Cropp, and J. Miller (1994), Tectonic structure across the accretionary and erosional parts of the Japan Trench margin, *Journal of Geophysical Research, 99*(B11), 22349–22361, doi:10.1029/94jb01198.

von Huene, R., M. Langseth, N. Nasu, and H. Okada (1982), A summary of Cenozoic tectonic history along the IPOD Japan Trench transect, *Geological Society of America Bulletin, 93*(9), 829-846, doi:10.1130/00167606(1982)93<829:ASOCTH>2.0.CO;2.

Vrolijk, P. (1990), On the mechanical role of smectite in subduction zones, *Geology*, *18*(8), 703-707.

Wang, K., and K. Suyehiro (1999), How does plate coupling affect crustal stresses in Northeast and Southwest Japan?, *Geophysical Research Letters, 26*(15), 2307-2310, doi:10.1029/1999GL900528.

Wilson, J., J. Chester, and F. Chester (2003), Microfracture analysis of fault growth and wear processes, Punchbowl Fault, San Andreas system, California, *Journal of Structural Geology, 25*(11), 1855–1873, doi:10.1016/S0191-8141(03)00036-1.

Xu, S., Y. Ben-Zion, J. P. Ampuero, and V. Lyakhovsky (2014), Dynamic Ruptures on a Frictional Interface with Off-Fault Brittle Damage: Feedback Mechanisms and Effects on Slip and Near-Fault Motion, *Pure and Applied Geophysics, 172*(5), 1243-1267.

Yang, T., T. Mishima, K. Ujiie, F. M. Chester, J. J. Mori, N. Eguchi, S. Toczko, and Exp. 343 Scientists (2013), Strain decoupling across the décollement in the region of large slip during the 2011 Tohoku-Oki earthquake from anisotropy of magnetic susceptibility, *Earth and Planetary Science Letters, 381*, 31-38, doi:10.1016/j.epsl.2013.08.045.

Yue, H., and T. Lay (2011), Inversion of high-rate (1 sps) GPS data for rupture processes of the 11 March 2011 Tohoku earthquake (M_w 9.1), *Geophysical Research Letters, 38*, L00G09, doi:10.1029/2011GL048700.

Zeeb, C., E. Gomez-Rivas, P. D. Bons, and P. Blum (2013), Evaluation of sampling methods for fracture network characterization using outcrops, *AAPG Bulletin*, *97*(9), 1545-1566, doi:10.1306/02131312042.

CHAPTER 4

Future work and remaining questions

4.1 Future work

This thesis provides the basis for future investigations regarding the role of fault friction on damage zones and frictional strength of the shallow Japan Trench décollement. While I have addressed preliminary questions regarding the effect of friction on damage zone characteristics via the JFAST core, I can recommend a few future studies based on the following questions:

Can damage zone measurements in future drill cores better constrain variability of fault friction on shallow Japan Trench décollement and inheritance of structures?

Future IODP drilling expeditions in the shallow Japan Trench (JTRACK) are in the planning stages [*Sample et al.*, 2014]. By drilling at multiple sites that slipped different amounts during the 2011 Tohoku-oki earthquake, the expedition may be able to better assess the control of fault zone material properties on shallow slip. Coring the incoming Pacific plate section will provide an opportunity to assess the background level and nature of structures prior to subduction. Additional coring in the frontal prism will allow for comparison of damage zone characteristics across several locations on the décollement. This could provide an opportunity to investigate any variability in induced damage, damage zone characteristics, and perhaps fault friction or roughness along the shallow décollement. *In situ* stress determinations may help elucidate the long-term fault strength by evaluating the recovery process of the décollement following a great earthquake. In summary, similar damage zone characterization in future Japan

Trench drill cores will expand the spatial constraints of this study and perhaps provide insight regarding variability of frictional strength along the shallow décollement.

What is the effect of damage zone characteristics at the shallow Japan Trench on the fluid transport properties?

Damage zones can act as a conduit for fluid flow, and thus are inherently related to the permeability structure of fault zones [*Caine et al.*, 1996]. By using information gathered in this study regarding structural patterns in the fault damage zone, future work may focus on the characterization of hydraulic properties. Aperture distribution, connectivity, and present day stress field would all be important considerations. In high porosity rocks, the damage zone permeability is controlled by the frequency and connectivity of both low permeability deformation bands and of high permeability open fractures [*Lunn et al.*, 2008], both of which are present in the décollement damage zone. Interestingly, permeability reduction across deformation bands is highly influenced by the amount of phyllosilicates present, and increases rapidly with increasing phyllosilicate content [*Fossen and Hesthammer*, 2000]. Such phyllosilicate bands make up 29% of the core-scale tectonic structures transected by linear scanline sampling in the examined cores of this thesis, and therefore could have an interesting impact on fluid transport characterization. Structural complexity, such as large changes in structure intensity, has been shown to change damage zone permeability over several orders of magnitude [*Wibberley and Shimamoto*, 2003]. Frequency and orientation of microstructures will also influence permeability. A future study could model the fluid flow throughout the footwall and hanging wall fracture networks, including the effect of permeability along the décollement [*Tanikawa et al.*, 2013; *Valdez et al.*, 2015]. Several comprehensive approaches to integrating

damage zone characteristics into fluid flow modeling exist in the literature [e.g. *Brown and Bruhn,* 1998; *Caine and Forster*, 1999; *Caine and Tomusiak,* 2003; *Johri*, 2012]. Method typically assign appropriate effective permeability tensor values to various reservoir grid blocks, depending on fracture intensity and flow properties, to model the fracture network, which can be based on extensive field data. *Johri* [2012] simulate fluid flow by upscaling the fracture population to obtain effective continuum grid flow properties using Oda's method [*Oda,* 1985]. Fluid flow modeling integrating the damage zone characteristics at the shallow Japan Trench would help improve our understanding of fluid flow in accretionary prisms [*Moore and Vrolijk*, 1992], especially adjacent to the shallow décollement where the role of fluids and pore pressure may be important in assessing seismic hazards.

Can the schematic representation of distinct JFAST damage zone data be applied in the field to test for relative fault friction based solely on damage zone observations in similar lithologies?

In section 3.6.2, I have proposed a schematic representation of my data and interpretation of its distinct characteristics (Fig. 13), implying the assessment of relative fault friction from damage zone thickness and decay is applicable elsewhere. An interesting future study would be to test this idea in the field at a fault where many of the variables (e.g. host lithology, stress regime, depth) are fixed. For example, by examining a fault with variations in damage zone thickness and decay exponents along strike, one could hypothesize a non-uniform distribution of friction along the fault or changes in fault geometry. Similarly, measurements of damage zone thickness and decay exponents on two separate faults of the same lithology could be used to assess relative fault friction, with contributions from laboratory results. It would be important to constrain roughness of the fault to make sure changes in damage zone properties are not the

result of changes in fault geometry. Or perhaps the changes in damage zone properties with changes in fault geometry are systematic? An important contribution of a study of this sort could be to densify the number of data points on the damage decay exponent – displacement scaling plot (Fig. 10b,c) for a single fault with varying displacements. This could be similar to the way *Faulkner et al.* [2011a] have isolated damage zone thickness and displacement measurements around one fault system to avoid making comparisons across different settings.

4.2 Remaining questions

Finally, a few questions without suggested methods or similar studies remain:

1. What is the effect of varying static fault friction on off-fault deformation decay in dynamic rupture models?
2. How long does it take for faults to reach critical structure intensity in the adjacent damage zone?
3. How rough is a plate-boundary fault? How does it scale with other faults?
4. What do the damage zone of other shallow subduction zone faults (e.g. Nankai, Barbados, Costa Rica) look like? Is there a connection between damage zone characteristics, long-term fault strength, and seismicity patterns across subduction zones worldwide?
5. What is the role of damage zones on induced seismicity? Are certain damage zone characteristics related to the magnitude of induced seismic events?
6. Can we use to character of damage zones to better predict faults close to failure?
7. Is there a relationship between damage zone characteristics and fractured reservoir productivity

REFERENCES

Brown, S. R., and R. L. Bruhn (1998), Fluid permeability of deformable fracture networks, *Journal of Geophysical Research, 103*(B2), 2489–2500, doi:10.1029/97JB03113.

Caine, J. S., and C. B. Forster (1999), Fault zone architecture and fluid flow: Insights from field data and numerical modeling, in: Haneberg, W. C., P. S. Mozley, J. C. Moore and L. B. Goodwin (eds.), *Faults and Subsurface Fluid Flow in the Shallow Crust*, American Geophysical Union, Washington, D. C.

Caine, J. S., and S. R. Tomusiak (2003), Brittle structures and their role in controlling porosity and permeability in a complex Precambrian crystalline-rock aquifer system in the Colorado Rocky Mountain Front Range, *Geological Society of America Bulletin*, *115*(11), 1410-1424.

Caine, J. S., J. P. Evans, and C. B. Forster (1996), Fault zone architecture and permeability structure, *Geology*, *24*(11), 1025-1028.

Faulkner, D. R., T. M. Mitchell, E. Jensen, and J. Cembrano (2011a), Scaling of fault damage zones with displacement and the implications for fault growth processes, *Journal of Geophysical Research, 116*, B05403, doi:10.1029/2010JB007788.

Fossen, H., and J. Hesthammer (2000), Possible absence of small faults in the Gullfaks Field, northern North Sea: implications for downscaling of faults in some porous sandstones, *Journal of Structural Geology*, *22*(7), 851-863, doi:10.1016/s0191-8141(00)00013-4.

Johri, M. (2012), Fault damage zones-observations, dynamic modeling, and implications on fluid flow, Ph.D. dissertation, Department of Geophysics, Stanford University, Palo Alto, CA, 105–140.

Lunn, R. J., J. P. Willson, Z. K. Shipton, and H. Moir (2008), Simulating brittle fault growth from linkage of preexisting structures, *Journal of Geophysical Research, 113*, B07403, doi:10.1029/2007JB005388.

Moore, J. C., and P. Vrolijk (1992), Fluids in accretionary prisms, *Reviews of Geophysics*, *30*(2), 113-135, doi:10.1029/92rg00201.

Oda, M. (1985), Permeability tensor for discontinuous rock masses, *Geotechnique*, *35*(4), 483-495, doi:10.1680/geot.1985.35.4.483.

Sample, J., J. Kirkpatrick, S. Kodaira, J. Mori, S. Saito, and M. Strasser (2014), Workshop report: Tracking the Tsunamigenic slips Across and Along the Japan Trench (JTRACK): Investigating a new paradigm in tsunamigenic megathrust slip with very deep water drilling using the D/V Chikyu, *International Ocean Discovery Program*, http://usssp-iodp.org/wp-content/uploads/JTRACK_workshop_report.pdf

Tanikawa, W., T. Hirose, H. Mukoyoshi, O. Tadai, and W. Lin (2013), Fluid transport properties in sediments and their role in large slip near the surface of the plate boundary fault in the Japan Trench, *Earth and Planetary Science Letters, 382,* 150-160, doi:10.1016/j.epsl.2013.08.052.

Valdez, R. D., II, R. M. Lauer, M. J. Ikari, H. Kitajima, D. M. Saffer, and Expedition 343/343T Scientists (2015), Permeability and consolidation behavior of sediments from the northern Japan Trench subduction zone, IODP Site C0019, in: Chester, F. M., J. J. Mori, *et al.* (eds.) *Proceedings of the Integrated Ocean Drilling Program; Japan Trench Fast Drilling Project (JFAST)*, College Station, TX, doi:10.2204/iodp.proc.343343T.201.2015.

Wibberley, C. A. J., and T. Shimamoto (2003), Internal structure and permeability of major strike-slip fault zones: the Median Tectonic Line in Mie Prefecture, Southwest Japan, *Journal of Structural Geology, 25* (1), 59-78, doi:10.1016/s0191-8141(02)00014-7.

APPENDIX

A1: Breccia zone image analysis

Where the spacing between structures was ~0.5 cm or less (i.e. breccia zones), we approximated the depths of structures within the zone by determining the average clast size. By assuming the boundaries of clasts within a breccia zone are fracture surfaces, the size of a clast is also a measure of fracture spacing. To measure clast properties, we implemented an image analysis technique in Matlab© following the methods of *Bjørk et al.* [2009]. After converting MSCL-I photos to gray scale and removing zones of induced damage in the photos, the Matlab© program uses gray scale-thresholding to separate individual grains and report average grain diameter, among other clast properties.

Table 3 outlines the breccia zones identified in the JFAST core, the threshold values used, and the resulting structure intensity calculation within the zone. Figure 14 shows an example of the image analysis process through the gray scale thresholding method.

Table 3: Breccia zone image analysis parameters									
Core Section	**Top Depth (mbsf)**	**Bottom Depth (mbsf)**	**Zone Thickness (mm)**	**Zone Width (pixels)**	**Lower Thresholding Value (pixels)**	**Upper Thresholding Value (pixels)**	**Min. Detectable Particle Size (pixels)**	**Number of fractures along linear transect**	**Structure intensity (st/m)**
16R-1	818.56	818.7	140	1014	120	230	200	40	0.29
16R-1	818.7	818.9	200	1022	120	240	200	83	0.42
16R-1	818.94	819.1	160	1024	120	220	100	48	0.30
16R-1	819.12	819.27	150	1024	120	205	100	36	0.24
16R-1	819.37	819.5	130	996	120	210	100	30	0.23
16R-1	824	824.12	120	1025	120	240	140	46	0.38
18R-1	824.24	824.28	40	1050	120	240	200	18	0.45
18R-1	824.55	824.69	140	1021	120	250	200	37	0.26
18R-1	824.73	824.8	70	1024	120	240	200	12	0.17
18R-1	824.92	824.96	40	1024	120	230	200	9	0.23
18R-1	825.05	825.15	100	1024	120	230	200	40	0.40
18R-1	825.31	825.38	70	1024	120	240	200	21	0.30
20R-1	832.04	832.08	40	1026	120	240	200	9	0.23

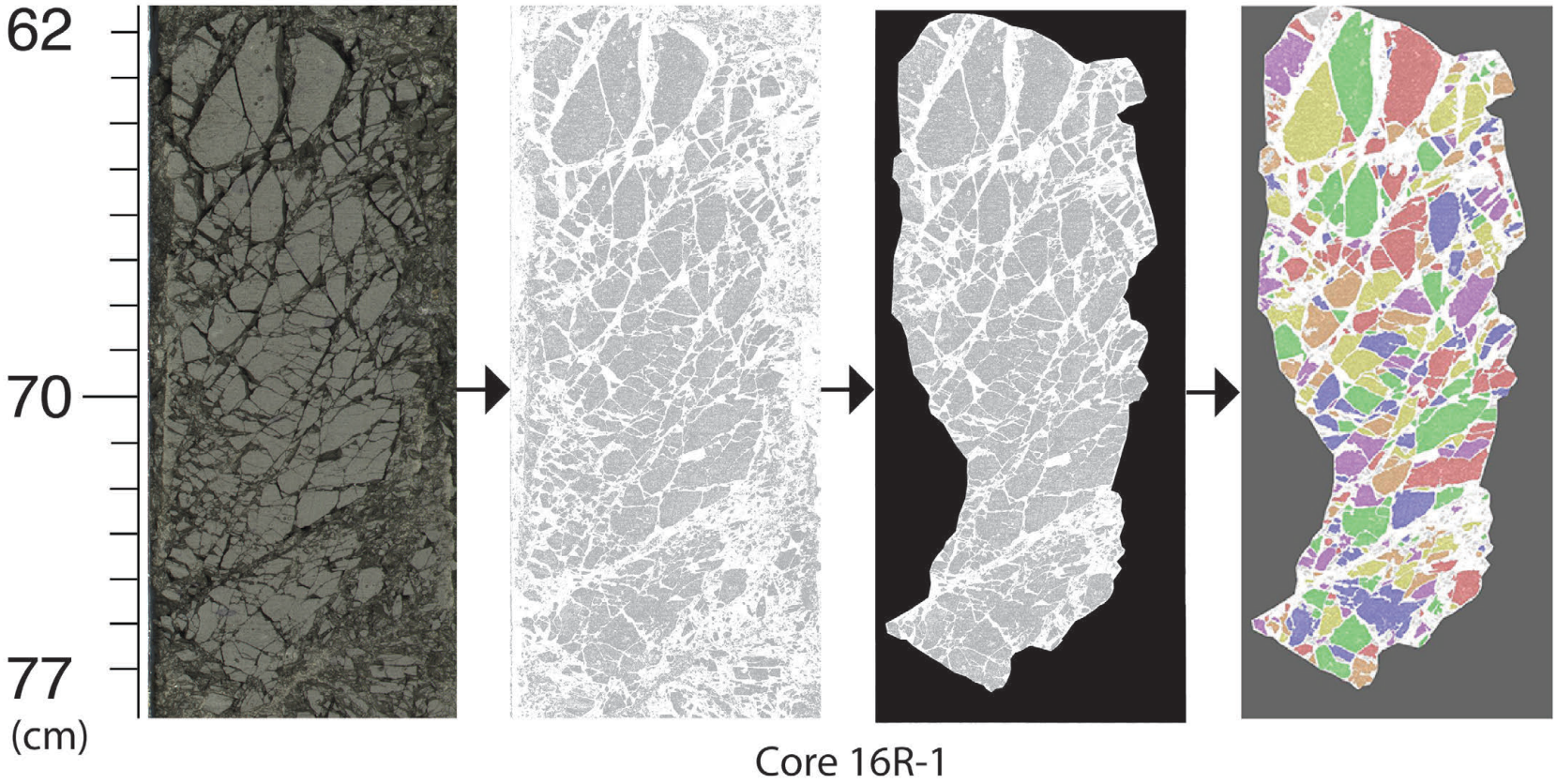

Figure 14: Example of gray-scale thresholding method to determine average grain size in breccia zones. MSCL-I core photos are converted to gray scale, cropped to remove zones of induced damage/drilling mud, and implemented into Matlab© code to identify individual grains.

A2: Calculating true dip angles in core

The following is obtained from *Chester et al.* [2013a; Structural methods]. For planar structures (e.g., bedding or faults), two apparent dips on two different surfaces (e.g., one being the split core surface, which is 90°–270° and vertical, and the other being the 0°–180° vertical surface) were measured in the core reference frame as azimuths (measured clockwise from 0°, looking down), and plunges. An XYZ coordinate system was defined in such a way that the positive *x*-, *y*-, and *z*-directions coincided with 0°, 90°, and vertical downward, respectively. If the azimuths and plunges of the two apparent dips were given as (α_1, β_1) and (α_2, β_2) respectively, then the unit vectors representing these two lines, v_1 and v_2, were

$$\mathbf{v}_1 = \begin{pmatrix} l_1 \\ m_1 \\ n_1 \end{pmatrix} = \begin{pmatrix} \cos\alpha_1 \cos\beta_1 \\ \sin\alpha_1 \cos\beta_1 \\ \sin\beta_1 \end{pmatrix} \text{ and } \mathbf{v}_2 = \begin{pmatrix} l_2 \\ m_2 \\ n_2 \end{pmatrix} = \begin{pmatrix} \cos\alpha_2 \cos\beta_2 \\ \sin\alpha_2 \cos\beta_2 \\ \sin\beta_2 \end{pmatrix},$$

where *l*, *m*, and *n* represent the *x*-, *y*-, and *z*-components of the vectors.

The unit vector normal to this plane (v_n) was then defined as follows:

$$\mathbf{v}_n = \begin{pmatrix} l_n \\ m_n \\ n_n \end{pmatrix} = \frac{\mathbf{v}_1 \times \mathbf{v}_2}{\left|\left(\mathbf{v}_1 \times \mathbf{v}_2\right)\right|},$$

$$\mathbf{v}_1 \times \mathbf{v}_2 = \begin{pmatrix} \begin{vmatrix} m_1 & m_2 \\ n_1 & n_2 \end{vmatrix} \\ \begin{vmatrix} n_1 & n_2 \\ l_1 & l_2 \end{vmatrix} \\ \begin{vmatrix} l_1 & l_2 \\ m_1 & m_2 \end{vmatrix} \end{pmatrix} = \begin{pmatrix} m_1 n_2 - m_2 n_1 \\ n_1 l_2 - n_2 l_1 \\ l_1 m_2 - l_2 m_1 \end{pmatrix}$$

where .

The azimuth (α_n) and plunge (β_n) of v_n were given by:

$$\alpha_n = \tan^{-1}\left(\frac{m_n}{l_n}\right), \quad \beta_n = \sin^{-1} n_n .$$

The dip direction (α_d) and dip angle (β) of this plane were α_n and 90° + β_n, respectively, when $\beta_n < 0°$. They were $\alpha_n \pm 180°$ and 90° – β_n, respectively when $\beta_n \geq 0°$. The right-hand rule strike of this plane (α_s) was then given by $\alpha_d - 90°$.

A3: Microstructure sampling method

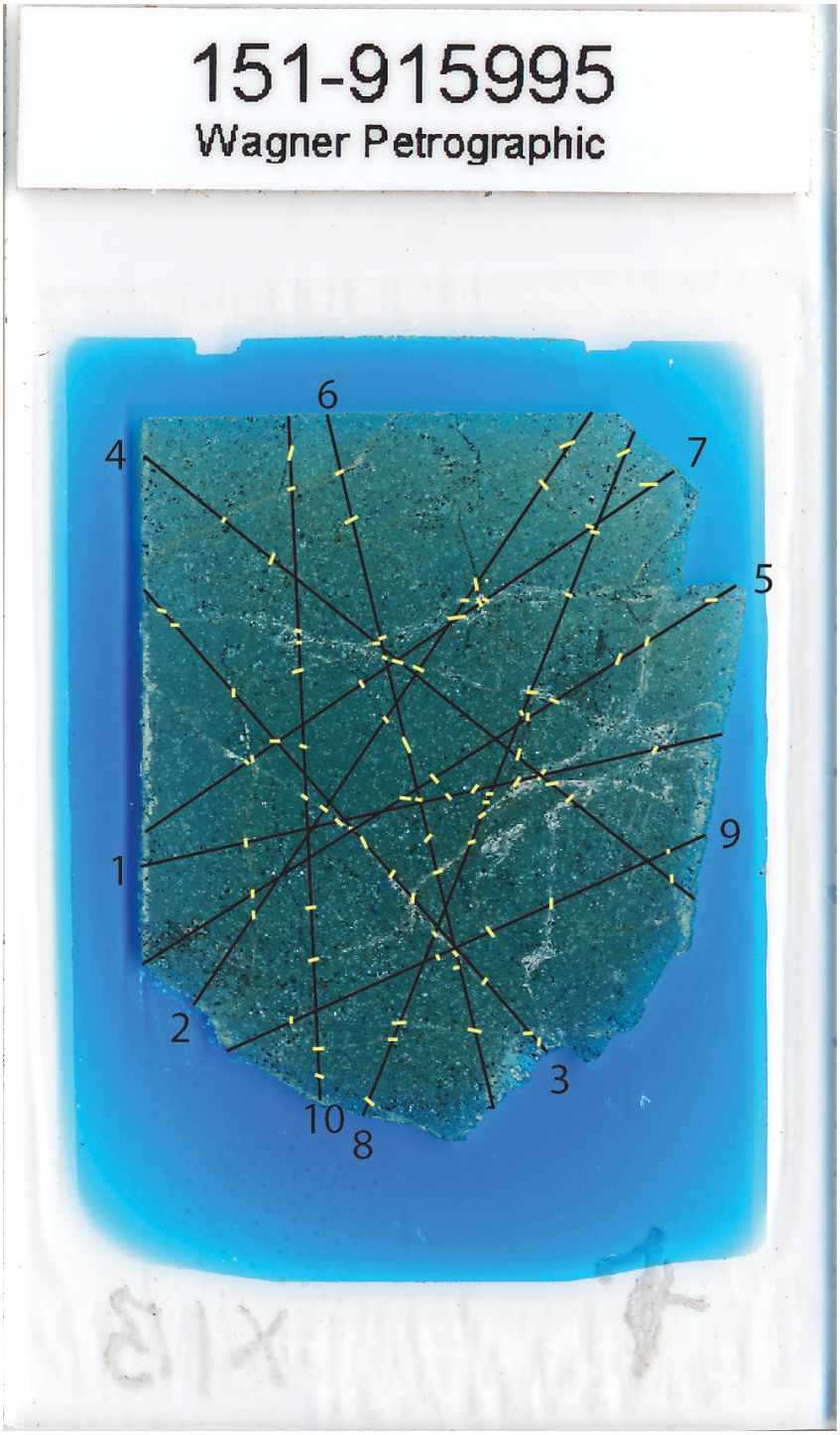

Figure 15: Example of microstructure (ms) sampling technique. Ten randomly oriented linear scanlines were drawn on each of three orthogonally cut thin sections. Number of microstructures intersecting each line (yellow ticks) were counted. Line length was measured, resulting in an intensity calculation in the form of (ms/mm).

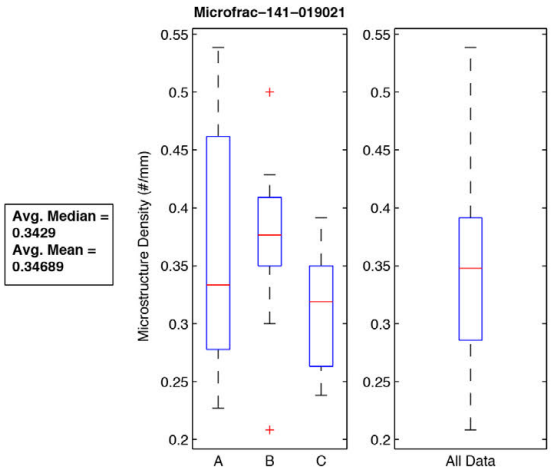
Microfrac–141–019021
Avg. Median = 0.3429
Avg. Mean = 0.34689
Microstructure Density (#/mm)
A
B
C
All Data

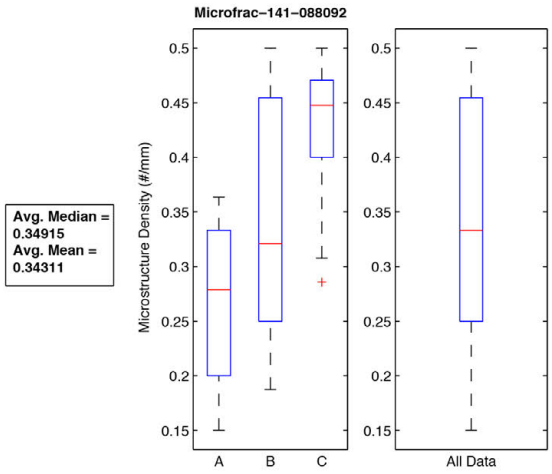
Microfrac–141–088092
Avg. Median = 0.34915
Avg. Mean = 0.34311
Microstructure Density (#/mm)
A
B
C
All Data

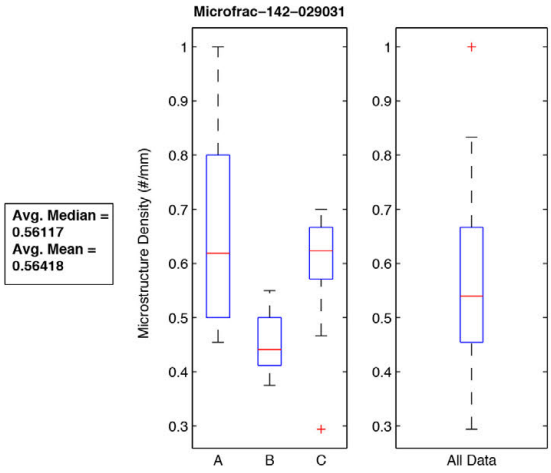
Microfrac–142–029031
Avg. Median = 0.56117
Avg. Mean = 0.56418
Microstructure Density (#/mm)
A
B
C
All Data

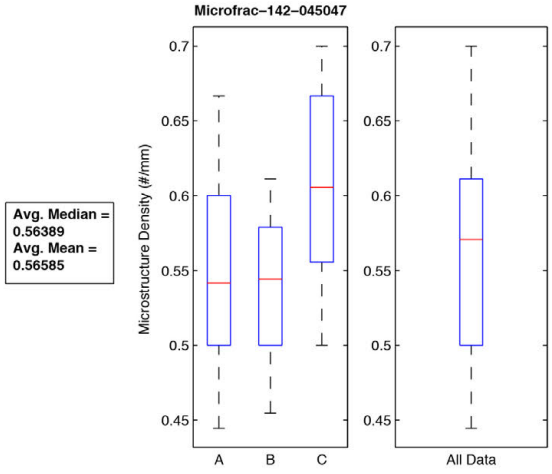
Microfrac–142–045047
Avg. Median = 0.56389
Avg. Mean = 0.56585
Microstructure Density (#/mm)
A
B
C
All Data

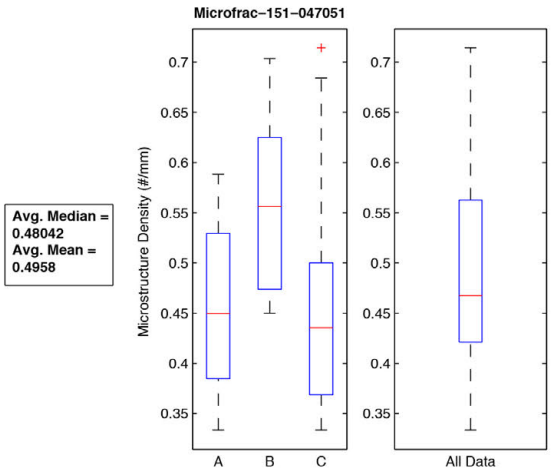
Microfrac–151–047051
Avg. Median = 0.48042
Avg. Mean = 0.4958
Microstructure Density (#/mm)
A
B
C
All Data

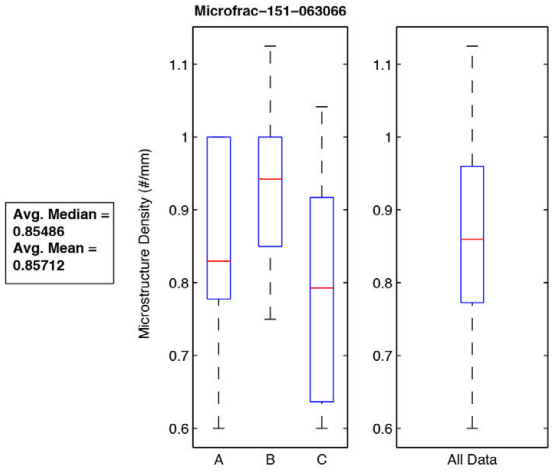
Microfrac–151–063066
Avg. Median = 0.85486
Avg. Mean = 0.85712
Microstructure Density (#/mm)
A
B
C
All Data

Avg. Median = 0.98863
Avg. Mean = 1.0205

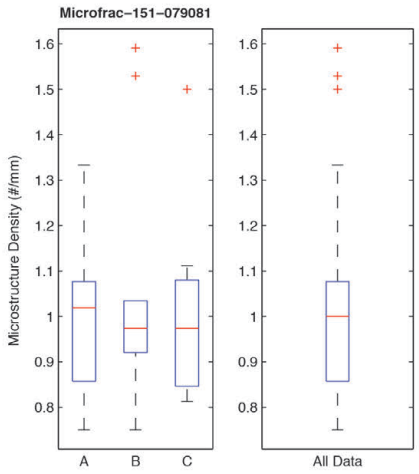

Avg. Median = 0.95959
Avg. Mean = 0.97624

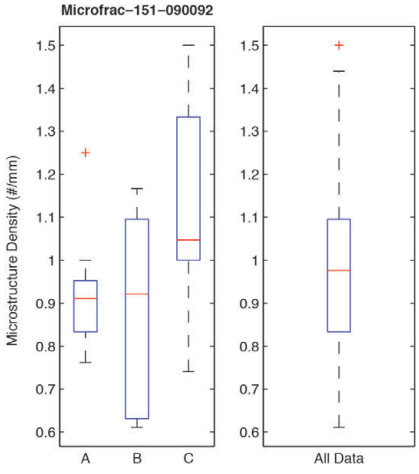

Avg. Median = 0.75988
Avg. Mean = 0.76656

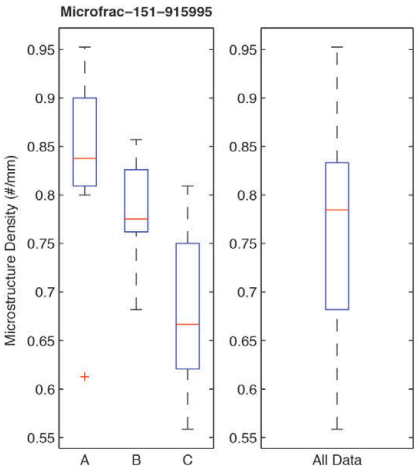

Avg. Median = 1.0161
Avg. Mean = 1.0162

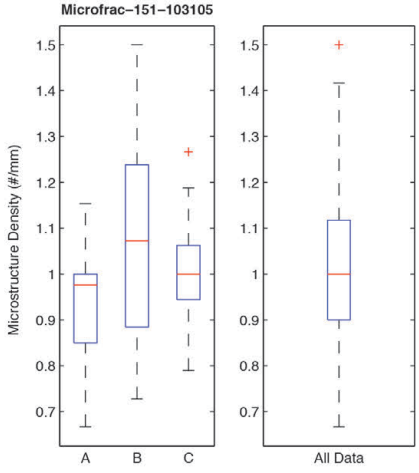

Avg. Median = 1.0518
Avg. Mean = 1.093

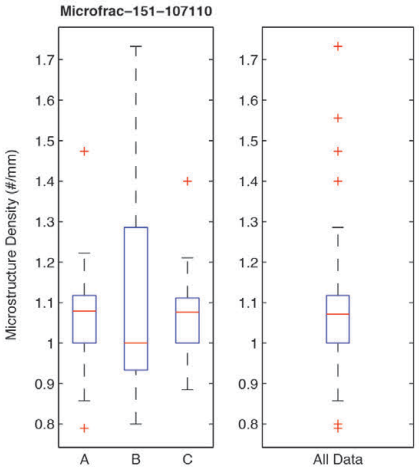

Avg. Median = 0.48205
Avg. Mean = 0.5018

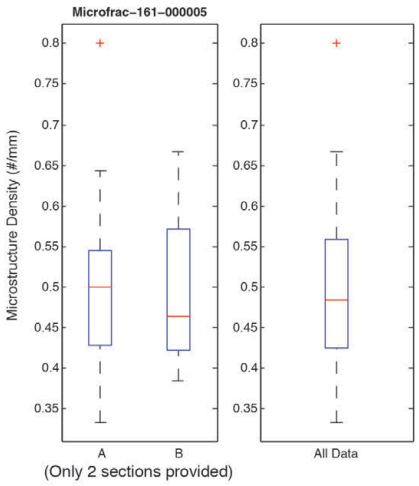

Avg. Median = 1.1326
Avg. Mean = 1.1509

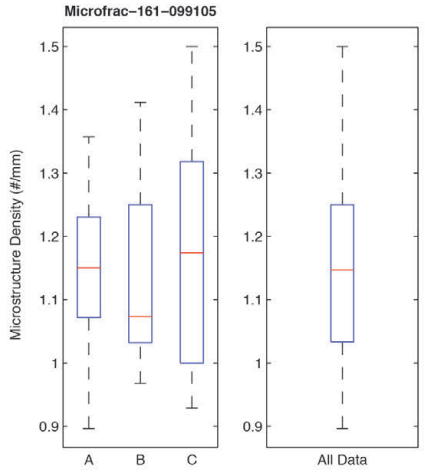

Avg. Median = 0.94484
Avg. Mean = 0.92109

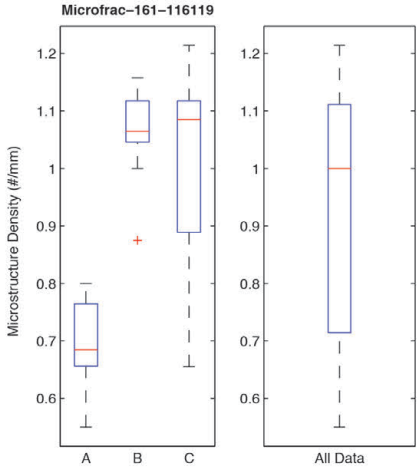

Avg. Median = 2.0578
Avg. Mean = 2.0433

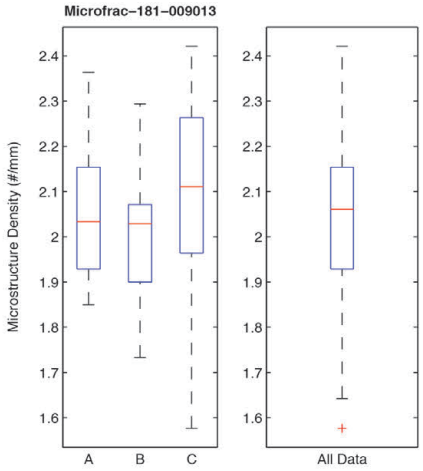

Avg. Median = 1.9824
Avg. Mean = 1.9572

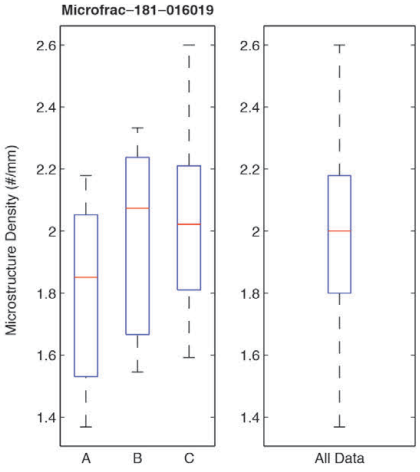

Avg. Median = 2.0194
Avg. Mean = 1.9998

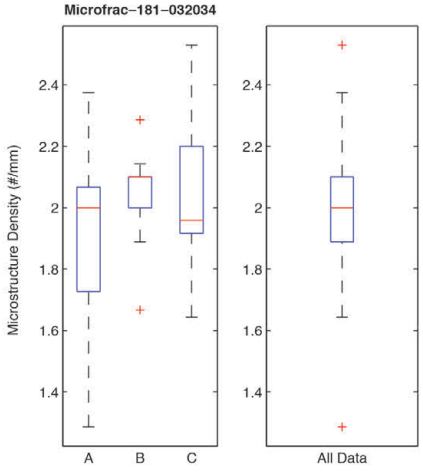

Avg. Median = 1.3132
Avg. Mean = 1.3438

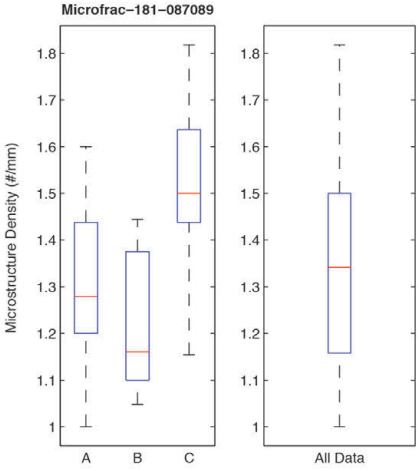

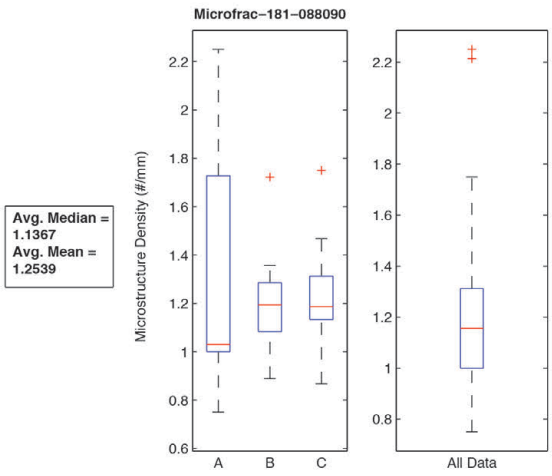
Microfrac–181–088090
Avg. Median = 1.1367
Avg. Mean = 1.2539
Microstructure Density (#/mm)
A
B
C
All Data

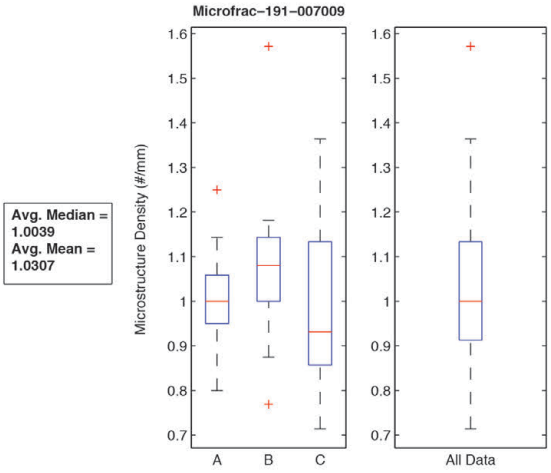
Microfrac–191–007009
Avg. Median = 1.0039
Avg. Mean = 1.0307
Microstructure Density (#/mm)
A
B
C
All Data

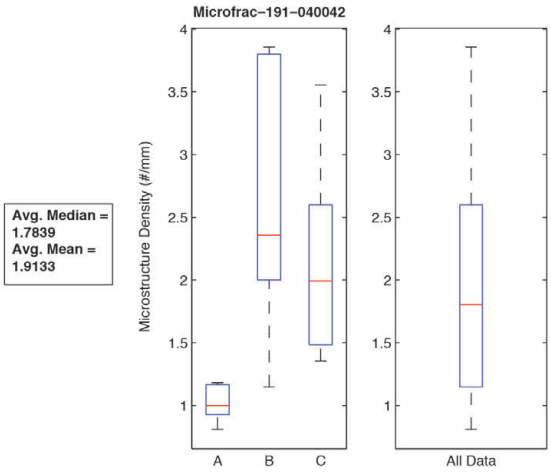
Microfrac–191–040042
Avg. Median = 1.7839
Avg. Mean = 1.9133
Microstructure Density (#/mm)
A
B
C
All Data

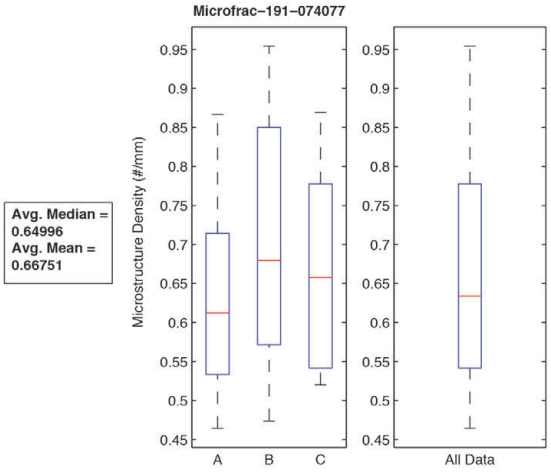
Microfrac–191–074077
Avg. Median = 0.64996
Avg. Mean = 0.66751
Microstructure Density (#/mm)
A
B
C
All Data

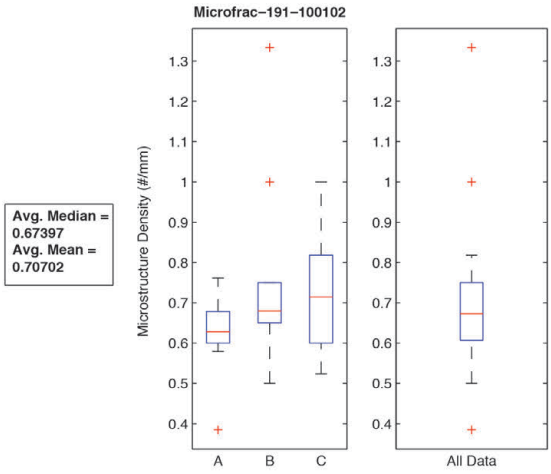
Microfrac–191–100102
Avg. Median = 0.67397
Avg. Mean = 0.70702
Microstructure Density (#/mm)
A
B
C
All Data

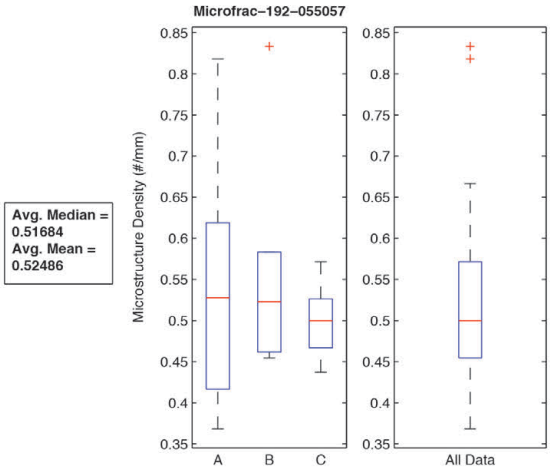
Microfrac–192–055057
Avg. Median = 0.51684
Avg. Mean = 0.52486
Microstructure Density (#/mm)
A
B
C
All Data

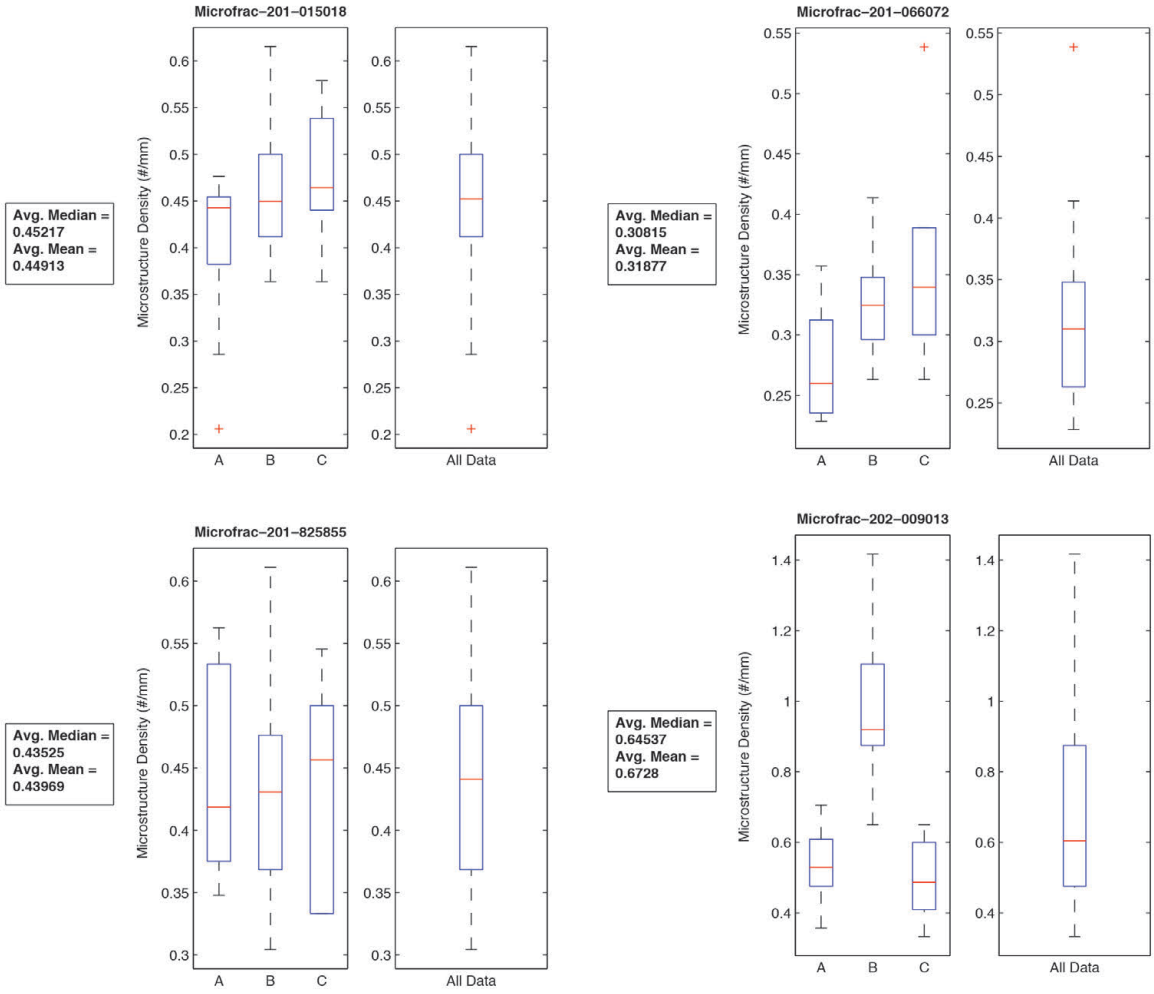

Figure 16: Box-and-whisker plots for microstructure intensity calculations (ms/mm) in three orthogonal thin sections (A, B, C) examined for each sample (Microfrac-[core section number]-[depth range of sample in core]). For example, Microfrac-201-825855 is core section 20R-1, sampled between 82.5 and 85.5 cm. “All data” indicates box-and-whisker distribution for the three orthogonal sections combined. Average median and average mean values are calculated for each sample, demonstrating a small variance in the two values and importance of using the median when a normal distribution of data cannot be assumed.

A4: Apparent dip (rake) angles

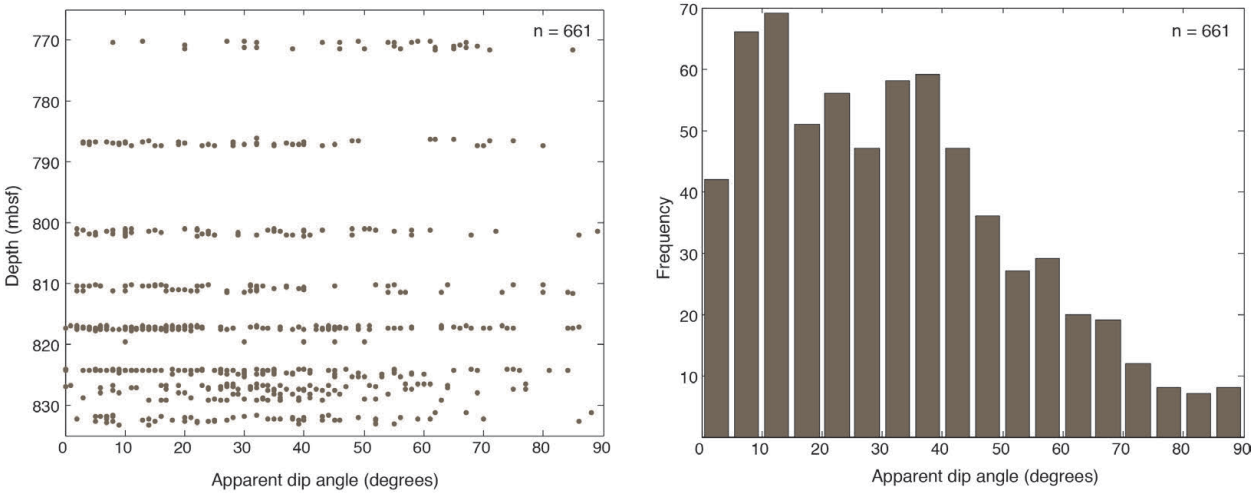

Figure 17: All apparent dip angles in core archive half of tectonic structures intersected by linear scanline. Not all structures in breccia zones included, hence smaller n-value compared to total number of sampled structures. A) Variability with depth; B) frequency distribution.

A5: Model failure criteria

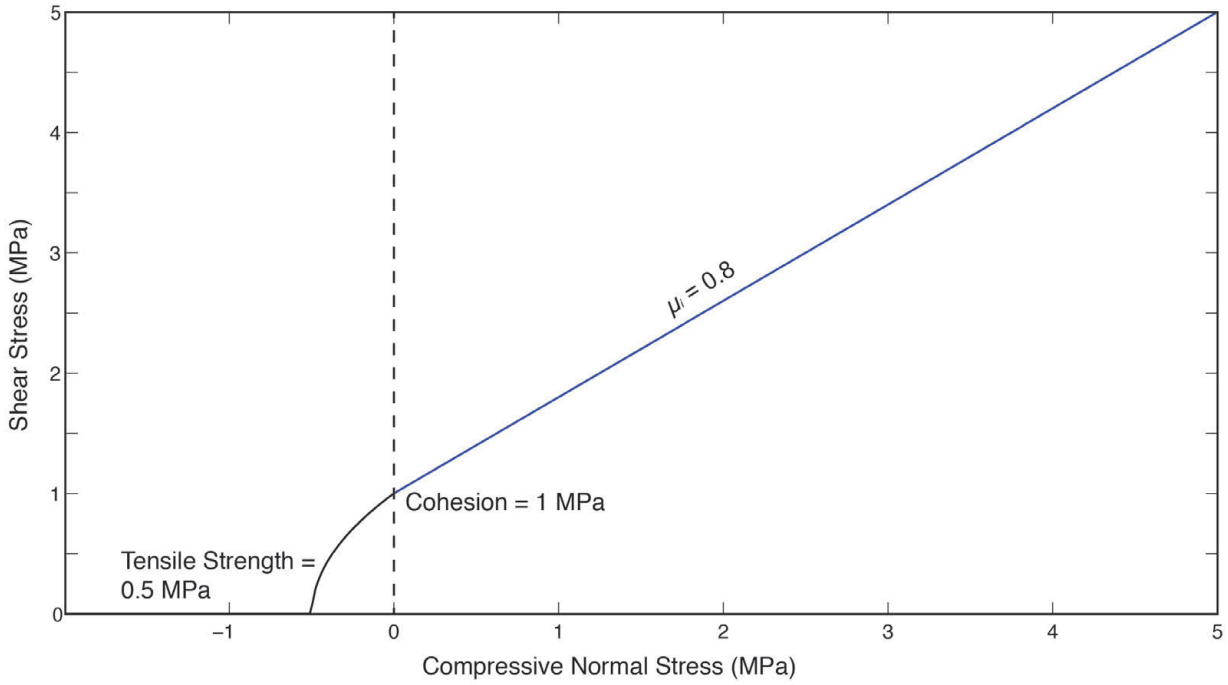

Figure 18: Failure criteria for JFAST host rock applied in the analytical model of stress distribution around a wavy fault, with parameters derived from *Chester et al.* [2013a] and *Ikari et al.* [2015].